Louisiana Tech University

Louisiana Tech Digital Commons

Summer 8-16-2018

Development of a Longitudinal Imaging System for Murine Brain Injury Models

Chelsea D. Pernici
Louisiana Tech University

Follow this and additional works at: https://digitalcommons.latech.edu/dissertations

Doctoral Dissertations   Graduate School

Summer 8-16-2018

Development of a Longitudinal Imaging System for Murine Brain Injury Models

Chelsea D. Pernici

DEVELOPMENT OF A LONGITUDINAL

IMAGING SYSTEM FOR MURINE

BRAIN INJURY MODELS

by

Chelsea D. Pernici, B.S.

A Dissertation Presented in Partial Fulfillment
of the Requirements of the Degree
Doctor of Philosophy

COLLEGE OF ENGINEERING AND SCIENCE
LOUISIANA TECH UNIVERSITY

August 2018

LOUISIANA TECH UNIVERSITY

THE GRADUATE SCHOOL

APRIL 19, 2018
_____
Date

We hereby recommend that the dissertation prepared under our supervision by
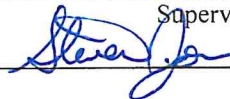
Chelsea Dressel Pernici, B.S.
_____

entitled **DEVELOPMENT OF A LONGITUDINAL IMAGING SYSTEM**
_____

FOR MURINE BRAIN INJURY MODELS
_____

_____

be accepted in partial fulfillment of the requirements for the Degree of

Doctor of Philosophy in Biomedical Engineering
_____

_____
Supervisor of Dissertation Research
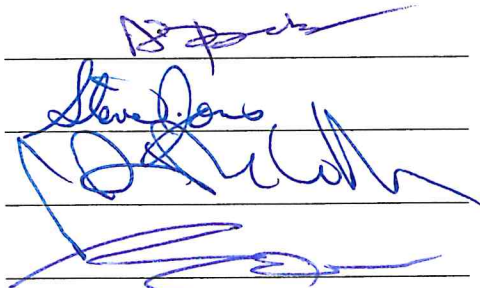
_____
Head of Department
Biomedical Engineering
_____
Department
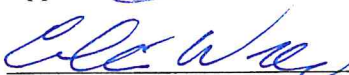
Recommendation concurred in:

_____

_____

_____   Advisory Committee

_____

Approved:

_____
Director of Graduate Studies

_____
Dean of the College

Approved:

_____
Dean of the Graduate School

ABSTRACT

Following traumatic brain injury (TBI) and stroke, secondary injury cascades can lead to axonal damage and persistent microglia activation, respectively, in subcortical regions of mice. Current techniques, such as diffusion tensor imaging (DTI) and histology are used to observe features related to damage, but DTI lacks cellular resolution and histology is conducted on fixed tissue, preventing longitudinal studies in the same mouse. The combination of cranial windows and multiphoton microscopy (MPM) is used to image cells in the upper layers of the mouse cortex, but resolution rapidly degrades with imaging depth, making it difficult to observe white matter and subcortical regions following TBI and stroke. To circumvent this challenge, a novel imaging system was developed capable of obtaining longitudinal data related to this secondary damage in subcortical regions of mice.

An existing technology, gradient refractive index (GRIN) lenses, was used in conjunction with MPM to image mice before and after injury models. GRIN lenses were attached to low profile head plates and surgically implanted into the brain of mice to acquire time-lapse images of white matter for 60 days following midline fluid percussion injury and microglia 24 hours after a MCAo stroke model. Thy1-YFP and Cx3cr1-tdTomato mice were used to compare changes in white matter fiber tracks and microglia dynamics, respectively. In a model of stroke, injured mice exhibited larger soma areas as compared to control treated animals, demonstrating their activated morphology. When

the potential therapeutic, Annexin A1, was administered, treated animals had smaller soma areas as compared to the saline treated animals, signifying Annexin A1's potential to mitigate inflammation. The system was also used in a model of TBI and the results indicated injured animals developed significantly more varicosities and terminal bulbs than uninjured animals. When minocycline, an FDA approved antibiotic, was administered, treated animals had fewer varicosities and terminal bulb development, demonstrating the potential of the therapeutic to protect against axonal degeneration following TBI. Overall, the imaging system was successfully used in preclinical trials to demonstrate the effectiveness of two potential therapeutics in two brain injury models.

APPROVAL FOR SCHOLARLY DISSEMINATION

The author grants to the Prescott Memorial Library of Louisiana Tech University the right to reproduce, by appropriate methods, upon request, any or all portions of this Dissertation. It is understood that "proper request" consists of the agreement, on the part of the requesting party, that said reproduction is for his personal use and that subsequent reproduction will not occur without written approval of the author of this Dissertation. Further, any portions of the Dissertation used in books, papers, and other works must be appropriately referenced to this Dissertation.

Finally, the author of this Dissertation reserves the right to publish freely, in the literature, at any time, any or all portions of this Dissertation.

Author _____

Date _____

DEDICATION

This dissertation is dedicated to my mother, for teaching me to always persevere and be true to myself, to my father, for teaching me a strong work ethic goes a long way, and to my husband, who kept me sane and caffeinated on this nonlinear path to success.

TABLE OF CONTENTS

LIST OF TABLES

LIST OF FIGURES

Figure 39. *In vivo* image set of astrocytes in lower levels of cortex viewed through an implanted GRIN lens. A z-stack of 51 images spaced 1 μm apart in depth was acquired through a GRIN lens implanted in an adult GFAP-GFP mouse. Astrocyte cell bodies and processes were observed throughout the volume. Z-projections were made of several consecutive image planes (steps). All images were projections of 5 consecutive image planes with the exception of Image E in which 10 planes were used for the projection. The most dorsal image plane was defined as plane 1 and the most ventral image was plane 51. Z-projection planes for A-H were, as follows: A. 1-5, B. 5-10, C. 10-15, D. 15-20, E. 25-35, F. 35-40, G. 40-45, H. 45-50. A Gaussian filter with σ=1.33 was applied to all channels to reduce background noise. **Scale bar = 5 μm** [15].   49

Figure 310. Two-channel *in vivo* image obtained through an implanted GRIN lens. The image is from prefrontal cortex of an adult GFAP-GFP mouse implanted with a 350 μm diameter GRIN lens. Texas red-dextran dye was injected into the tail vein to visualize the vasculature. A few glial cells expressing GFP under the GFAP promoter can be seen near one of the blood vessels near the center of the image. A Gaussian filter with σ=1.33 was applied to all channels to reduce background noise. **Scale bar = 5 μm** [15].   50

Figure 41. Nissl stained sagittal section (image, exclusive of locations for analyzing microglia activation levels, courtesy of Dr. Xiao Hong Lu, Louisiana State University Health Sciences Center, Shreveport, LA). Locations for analysis of microglia activation state in brain slice images were, as follows (**A**) CA3 in the hippocampus, (**B**) the cerebral cortex directly above CA3, (**C**) the necrotic core of the ischemic region, (**D**) the transition zone, directly above position C on the ventral side of the corpus callosum, (**E**) penumbra of the stroke, and (**F**) the rostral cortex.   60

Figure 42. Representative images at baseline and 24 hours after sham or transient (60 min) MCAo procedure. Insets are single cells showing activation states. Microglia become activated (retracted processes) **(B)** as compared to both baseline **(A, C)** and sham treated animal **(D)**. Insets are representative images of microglia morphology. Images are z-projections of 10 x 1 μm slices. **Scale bar = 10 μm.**   62

Figure 43. AnxA1 may be protective against microglial activation, but not through FPR2/ALX mechanism. Mice underwent sham (n=1) or transient (60 min) MCAo (n = 8) and administered saline (n=2), AnxA1 (n=3) or AnxA1 + Boc 2 (n=2). Cell soma area was calculated at baseline and at 24 hours post reperfusion. Data is represented as mean normalized soma area ± SEM.   63

Figure 44. Representative brain slice images of positions B, E, and F comparing microglia activation when treated with AnxA1 **(A-C)** versus treated with saline **(D-F).** AnxA1 treated animals had microglia with smaller soma areas in the cortex after

ACKNOWLEDGMENTS

First and foremost, I would like to thank my parents for their continued support throughout my journey at Louisiana Tech University and for encouraging me to dream big. Second, I'd like to acknowledge my husband who stuck with me through all the ups and downs of graduate school and kept me fed and caffeinated the last year and a half. I'd like to acknowledge my committee members for their help throughout the years. Thank you to Dr. Mark DeCoster for all the knowledge and classes concerning fluorescent imaging. Thank you to Dr. Bryant Hollins for always checking in and seeing how my research is progressing. Thank you to Dr. Steven Jones for making me think philosophically, to never, ever forget to title my x and y axis on a graph, and the endless conversations about the joys of running. Thank you to Dr. Prahbu Arumugam for stepping in and serving on my advisory committee last minute when it was crucial. I'd like to acknowledge Dr. James Spaulding for his constant aid and animal support throughout the years. Thank you to Emily Born for being a good listener, friend, and for ensuring all the animals were taken care of during my experiments. Thank you to Dr. Alan Chiu for inspiring me as an undergraduate to pursue research in biomedical engineering. A big thank you to all my lab members for always being there so we could brainstorm ideas and on occasion, discuss our sanity for deciding on this career path. Finally, an enormous thank you to Dr. Teresa Murray for being my mentor during my graduate years at Louisiana Tech. Thank you for always having your door open to discuss

successes and failures. Without you forcing me get out of my comfort zone, make mistakes and push boundaries, I would not be the scientist I am today. Thank you for allowing me to work on three collaborative projects, one with Dr. Felicity Gavins at Louisiana State University Health and Sciences Center in Shreveport, one with Dr. Johnathan Lifshitz and Dr. Rachel Rowe at The University of Arizona, and one with Dr. Jeoungsoo Lee at Clemson University. These projects have allowed me to participate in interdisciplinary research, gain a wide range of skills, and network with professionals for my future career. Finally, I'd like to acknowledge the National Institutes of Health grants R21NS090131 and R21HD075376 to Dr. Teresa Murray for funding these projects.

CHAPTER 1

INTRODUCTION

1.1   Background

1.1.1   *In Vivo* Microscopy

In vivo studies are studies done in whole living organisms and *in vivo* imaging

uses a variety of modalities to conduct research at the organ, tissue, cell and molecular

level in animals, with murine models being especially popular. Imaging is crucial to

better understand the diseases, injury, and inflammation of the brain as well as being vital

in drug development. Furthermore, it is increasingly important to be able to image

animals longitudinally to better understand the progression of disease and injury and

understand the long-term effects of potential therapeutics.

The brain is a highly dynamic, complex structure, capable of gathering,

organizing, and responding to multiple inputs. One of the main challenges in

neuroscience is understanding the underlying mechanisms involved in brain function, as

well as its response to stimulus and injury. Brain function involves both temporal and

spatial properties, making it difficult to fully understand its capabilities. Current

modalities such as diffusion tensor imaging and magnetic resonance imaging allow the

collection of longitudinal data, but they lack the resolution required to understand the

brain at a cellular level. Histology and clearing methods provide cellular resolution, but

since these methods cannot be employed in living animals, temporal data cannot be

collected. *In vivo* microscopy, specifically multiphoton microscopy, combined with novel technologies offers an opportunity to collect both spatial and temporal data in both the progression of brain injury and development of potential therapeutics.

1.1.2   Traumatic Brain Injury

Traumatic brain injury (TBI) is of great interest to biomedical researchers. Each year, 1.1 million Americans are treated for a traumatic brain injury in an emergency room setting, with approximately 50,000 injuries resulting in deaths [1]. An estimated 124,000 individuals discharged from the hospital with moderate to severe TBI develop long term disabilities each year [2], with an estimated 3.32 million individuals currently living with disabilities [3]. While individuals may survive a TBI, they often have limitations to their daily living such as social integration and financial independence. Sixty-six percent of individuals with a history of TBI will receive welfare or disability checks [4]. With TBI affecting such a large population and many being of a young age, the occurrence carries vast direct and indirect costs, $9.2 billion and $51.2 billion, respectively [5].

Traumatic brain injury is defined as damage to the brain as result of external forces. These forces can include acceleration or deceleration, impact, crushing forces, or penetration by an object. When this damage occurs, cognition and physical functions become impaired. Additionally, social functions are affected, often resulting in depression and anxiety [6]. Any type of laceration or penetration results in focal brain damage, while acceleration forces cause diffuse brain damage. Focal contusions will affect the gray matter of the brain, which constitutes the cell bodies while diffuse injuries play a part in white matter or axonal damage [7]. Traumatic brain injury is a complex

neurodegenerative condition, and its deleterious and progressive effects must be understood if an effective therapeutic treatment is to be found.

1.1.3   Stroke

Ischemic stroke is a neurological deficit occurring from decreased blood flow to the brain. Strokes cost the United States $34 billion annually and they kill approximately 130,000 people each year [8]. The American Heart Association (AHA) recognizes three types of stroke, ischemia, hemorrhagic, and transient ischemic attack, with ischemia accounting for an estimated 87 percent of all cases [9]. While ischemic stroke has a high rate of prevalence, few therapies or strategies exist to treat stroke or to prevent secondary damage. Despite the ongoing research in animal models of stroke, little has been done to translate experimental studies to a clinical level. Currently, the only treatment available for stroke is tissue plasminogen activator (tPA), which is a protein aiding in the breakdown of clots. While this protein has been beneficial, it must be administered within 6 hours following the ischemic event, and has only been effective in approximately 5% of all cases[10], [11]. Therefore, it is crucial we develop tools which can collect longitudinal data to better understand the progression of the disease and how therapeutics could intervene.

1.2   Project Overview

Discovering and optimizing therapies to aid in the recovery of traumatic brain injury (TBI) and ischemic stroke is of great interest to the translational, biomedical research community. Mice are often used in preclinical trials to test the effects of candidate therapies. The research projects described in Chapters 4 and 5 were run as preclinical trials implementing a novel, longitudinal imaging approach using mice.

Following ischemia, microglia become activated, contributing to the expansion of the infarct and mediating further damage [12]. An *in vivo* imaging system was tested to demonstrate its ability to elucidate neuroinflammation and determine the efficacy of a potential therapy, Annexin A1.

Current imaging modalities have shown that traumatic brain injury can cause diffuse axonal damage, which is not caused by merely one event, but by a progression of mechanical and cellular damage [13]. In addition, affected individuals have deficits in functionality such as memory and learning. This research characterizes these cellular changes over several weeks post-TBI. It uses multiphoton microscopy and implanted gradient refractive index (GRIN) lens technology to image axonal damage in the external capsule of mice. The external capsule is a region of the brain containing myelinated axons, or white matter. An imaging system that was previously developed in the Murray lab was modified in order to facilitate the induction of a TBI and collect high quality images [14], [15]. Behavioral performance was compared for the same mice before and after TBI to correlate performance with the stage of injury.

Minocycline is effective when administered between 45 min -4 hours following a traumatic brain injury [16]. The research expands on this knowledge by correlating acute drug administration to axonal damage and resolution. Furthermore, since it is not always plausible to treat individuals immediately following an injury, this research expanded the therapeutic window out to 72 hours and determined if its effect is comparable to acute administration at both a cellular and behavioral level.

Finally, non-viral vectors, specifically a polyplex micellar carrier with therapeutic compounds, has shown promise in reducing astrogliosis and facilitating axonal

regeneration when used in a rat model of spinal cord injury. The research described in Chapter 6 expands these studies; it uses an *in vivo*, murine model to demonstrate the ability of these micelles to diffuse in the brain. Micelles were locally injected into the brain and drug diffusion was imaged over the course of 3 days through a cranial window.

Overall, the project demonstrates the effectiveness of a novel longitudinal imaging system for use in preclinical trials. The device can collect high cellular resolution images in deep regions of the brain, an area inaccessible by current imaging modalities. The device was successfully used in two different murine brain injury models, collected images for longitudinal brain dynamic measurements, and demonstrated the benefits of two therapeutics.

1.2.1 <u>Hypothesis</u>

By using GRIN lens technology, the efficacy of candidate therapies for brain injuries can be measured. Annexin A1, an endogenous protein, can modulate neuroinflammation by inhibiting microglia activation when administered 6 and 18 hour post ischemia/reperfusion. Minocycline can prevent axonal degeneration following a model of TBI when administered beginning at 72 hours post TBI. Furthermore, a polyplex micelle has shown potential in facilitating axonal regeneration after spinal cord injury in rats. This same micelle carrier can be used in a murine model and diffuses in the brain after a local injection.

1.2.2 <u>Specific Aims</u>

In order to test these hypotheses, the following aims were accomplished:

1. Modify a previously developed imaging device such that it is applicable to brain injury models and potential therapy development.

2. Measure microglia dynamics 24 hours after ischemia/reperfusion (stroke) and AnxA1 treatment.

3. Measure progressive axonal degeneration following induced TBI and minocycline treatment over the course of 30 days.

4. Demonstrate diffusion of PgP-pβgal, a polyplex micelle carrier, after a local injection in a murine model.

1.3

CHAPTER 2

BACKGROUND

2.1 Traumatic Brain Injury

Traumatic brain injury has affected and continues to affect a large part of the population. Traumatic brain injury can lead to disabilities, including cognition, sensory, and behavioral problems [17], [18]. Most patients, if they recover consciousness, still suffer from cognitive problems, including many of their higher order thinking skills. Most commonly, they suffer from short and long term memory loss and become distracted easily, leading to deficits in planning and organization functionality [19]. Evidence suggests that individuals will suffer from anxiety and depressive behavior for months and even years after the initial injury [20], [21]. Suffering from a TBI has long term consequences not just for the individual, but for those around them. Past and on-going research has examined and defined many of the cognitive and behavioral deficits following injury. However, the underlying mechanisms of TBI are not yet sufficiently understood, and additional research at the cellular level is needed to better identify effective therapeutic targets.

2.1.1 Axons

Information in the brain is transmitted as electrical and chemical signals via the neurons, which are comprised of a cell soma, dendrites, and an axon. Signals originate at synapses in dendrites and travel to the soma and down an axon to other neurons. Axonal

structure is supported by microtubules, which form a unipolar array and facilitate transport of organelles, proteins, and RNA. Axonal transport is essential for neuronal function and damage to organization of the microtubules can be detrimental [22].

Myelin, which is produced by oligodendrocytes and considered the white matter of the brain, is comprised primarily of phospholipids. It functions as the insulator for axons, where signal propagation occurs. The fluid in the brain contains ions, which aid in the creation of electrical charge concentrations across the cell membrane and signal propagation. Along the axon, exist the nodes of Ranvier, which are gaps in the myelin sheath, exposing the axon to extracellular fluid. Under normal, healthy circumstances, the conduction of the signal leaps from one node to the next on an axon. When injury occurs, progressive damage causes a reduction in both myelin and axon quality. As a result the signal is reduced, and brain function associated with those neurons is impaired [23].

2.1.2   Microglia

Microglia are the resident immune cells of the brain and were identified by Nissl and Robertson at the end of the 19th century and coined by Pio del Rio Hortega in 1932 [24]. Microglia exhibit a highly ramified morphology with numerous long, tortuous processes extending in all directions originating at the cell soma. While microglia are termed resting, their processes are highly mobile, continuously surveying their environment for disturbances [25].

After injury, microglia respond to extracellular signals and in an effort to maintain homeostasis will clear cellular debris and toxic substances. When cells die, they release damage-associated molecular patterns (DAMPs). Microglia are equipped with pattern recognition receptors and when the DAMPs are detected, microglia produce cytokines

and chemokines, allowing them to communicate with other cells, further initiating the inflammatory response. In addition to these receptors, microglia express receptors for other factors released by injured neurons, including ATP and glutamate. In response to the released factors, microglia will retract their processes and transform from a ramified to an amoeboid morphology, resembling macrophages. This change in morphology allows microglia to proliferate and migrate towards the site of injury [26].

2.1.3   Diffuse Axonal Injury

Traumatic brain injury can be either focal or diffuse, with diffuse axonal injury (DAI) being the most common. During DAI, acceleration and rotational forces occur and spatiotemporal pressure variations cause compressive, tensile, and shear strains. The shape of the skull-brain interface can be described as approximately spherical. Skull-brain movements caused by the accelerative and rotational forces cause a secondary, spherical pressure wave. The isotropic property of brain tissue causes the spherical wave front to be conserved as it propagates to the deep regions of the brain. As it travels deeper, the area of the brain progressively decreases, and as a result the pressure gradient increases [27]. Consequently, DAI localizes in the white matters of brain, such as the corpus callosum and the brain stem, areas rich in axons.

As a result of the wave propagation, rapid compressive and tensile forces cause elongation of axons, damaging the microtubules. A loss of elasticity causes the microtubules to misalign, and when they reform, areas of swelling, known as varicosities, develop from interrupted axonal transport. The disorganization of axons and swellings can lead to disconnection of the axon, resulting in a terminal bulb. Varicosities and terminal bulbs are both considered hallmarks of brain injury [7].

In order to visualize white matter damage, diffusion tensor imaging (DTI) has been widely used. DTI has revealed a decrease in white matter anisotropy with increasing time following injury, correlating with behavioral problems [28]–[31]. Changes to the cellular microstructure following damage, cause the diffusion of water to be altered. In a healthy brain, diffusion is typically not obstructed parallel to the axonal fibers, but restricted perpendicular to the fibers. If damage occurs, the perpendicular diffusivity increases while parallel diffusivity decreases, signifying demyelination and axonal damage [32].

2.1.4   Secondary Injuries

The initial injury causes immediate damage to neurons, axons and blood vasculature, but it is the secondary injuries that cause many of the deleterious outcomes of TBI [33]. Secondary axotomy can occur as a result of abnormal calcium homeostasis. When the axonal membrane is disturbed by the strains of injury, they become leaky, allowing the influx of calcium. The increased levels of calcium cause enzymes to degrade key structural proteins and destroy the microtubules. This causes further accumulation of proteins, leading to additional axonal swellings, and if the axon becomes weak it can disconnect and form a terminal bulb can occur [34].

When neurons become damaged, they release cytokines and other pro-inflammatory molecules into the surrounding area. As a result, both resident and infiltrating immune cells are recruited to the site of damage, leading to chronic inflammation [35]. As part of the secondary injury cascade, microglia will react to the injury by becoming activated and remain activated for years after injury has occurred [36], [37]. Microglia activity was shown to relate to axonal irregularities in both humans

and rodents; microglia DNA was found in white matter regions months after the injury had occurred [38].

In rodents and humans, progressive axonal degradation occurs in parallel with behavioral and cognitive deficits [36], [39]. Additionally, this progressive loss is associated with microglia activation and infiltration [40], [41]. Few treatments are available to mitigate the deleterious secondary injuries that progressively cause axonal damage and microglia activation. In order to better address the lack of current options for TBI, drug candidates and the time frame in which administration would be most effective must be further explored.

2.2   Stroke

Stroke is the fifth leading cause of death in the United States, with few treatment options available [42]. Ischemia occurs when the blood vessel becomes obstructed, preventing blood from traveling to the brain. Typically, the middle cerebral artery, a major branch supplying blood to the brain, is occluded. As a result, insufficient oxygen and nutrients are delivered and cellular homeostasis is disrupted leading to cell death. At the core of the stroke, the area with the highest blood flow restriction, cell death occurs within the first few minutes and is nearly wide spread at 24 hours [43]. In the penumbra, the area less affected by the occlusion, cell death occurs more slowly through apoptosis. As a result, targeting this area, offers an opportunity for therapeutic intervention [44].

When the brain is deprived of oxygen and blood glucose during the ischemic phase, cells die, releasing damage signals into the environment, including ATP. Microglia become activated, phagocytosing debris and secreting proinflammatory molecules, leading to further tissue damage. However, microglia have also been shown to

secrete IL-10 and TGF-β, anti-inflammatory cytokines, and mice completely devoid of microglia have larger infarcts. As a result, microglia may be destructive during the repair phase, but their presence is needed to aid in alleviating the injury [45].

Only one drug therapy is available for stroke, tissue plasminogen factor (tPA). This factor is administered intravenously and works by dissolving the clot. It is only effective within the first few hours of stroke and the longer the treatment is delayed, the less effective it is. Additionally, tPA only addresses the occlusion in ischemia and not the secondary injuries [11]. As a result, a therapy that can intervene and modulate inflammation is needed.

2.3   Longitudinal *In Vivo* Imaging Methods

2.3.1   Multiphoton Microscopy

Biological tissue naturally scatters light, making it difficult to image deep brain animal tissue with linear imaging techniques such as bright field and fluorescence imaging. Multiphoton microscopy (MPM), recognized as the gold standard for *in vivo* imaging, is a non-linear optical method that uses near infrared light to excite photons *in vivo* from fluorescent structures. The fluorescence may come from labeling techniques such as transgenic mice or injectable fluorescent dyes. With the development of turnkey mode-locked laser systems, multiphoton microscopy can be used without extreme complexity.

Two photon absorption is a rare event. Two photons must arrive within approximately 0.5 fs of each other at a fluorescent molecule and combine their energies to cause the molecule to transition to an excited state. However, advances in the technology have made it possible to increase the probability on this excitation event. The

setup of MPM requires an ultrafast pulsed laser source and an excitation pathway. Mode locked lasers generate ultrashort light pulses at a rate of 100 MHz. As a result, the laser is essentially off more than it is on. Typically, high numerical aperture objectives are used, compressing photons in space. The combination of compressed laser power in time and photons in space leads to a higher probability of an excitation event. MPM relies on multiple photons being absorbed simultaneously, and as a result, it depends on photon concentration [46], [47].

Two-photon excitation is used to generate fluorescence. Two photons, each with one-half the energy needed to excite the molecule, must simultaneously be absorbed. Because wavelength and photon energy are inversely related, and the incident photons will have a wavelength that is two times the wavelength required in single photon excitation. This longer incident wavelength leads to an inverse Stokes shift, where the emitted signal has a shorter wavelength than the excitation source. Appropriate filters are used to collect the fluorescence of interest and an image can be reconstructed [48].

Multiphoton microscopy offers advantages over the use of one photon, continuous laser light used in confocal microscopy. MPM uses a longer wavelength, which leads to less light scattering and allows for deeper penetration of tissue. Confocal microscopy is limited to visualizing tissue about 100 μm below the surface of the brain, while MPM can penetrate depths between 500-600 μm[47]. The high density of laser light that can produce two-photon excitation of fluorophores, which is necessary for visualization, only occurs at the focal point of the laser beam and not throughout the entire area of tissue, minimizing background fluorescence. In contrast, confocal illumination bathes the entire thickness of the sample with higher energy light that can bleach fluorophores and damage

tissue regardless of the focal plane for imaging. MPM uses a raster scanning beam and therefore, the high energy focal point is constantly moving. As a result, photo bleaching of fluorophores and tissue damage are reduced [49], [50]. For these reasons, multiphoton microscopy remains the preferred choice for *in vivo* imaging over confocal or wide field fluorescence imaging.

Chronic *in vivo* imaging of the brain is necessary to fully understand the progression of disease and injury. Over the years, several methods have been employed with multiphoton microscopy to accomplish this goal. Cranial windows and thin skulled windows are most often used to image the upper cortex of the brain, while gradient refractive index lenses allow researchers to peer deeper into the brain.

2.3.2   Cranial Windows

Cranial windows were developed by Dr. Karel Svoboda and when properly executed, allow the observation of the same cortical area over time spans from minutes to months [51]. A craniectomy, in which a circular portion of the skull is removed, creates a window for observation. Depending on the application, the dura matter can be removed or left intact. Typically, low-melt agarose gel is placed between the brain and window to prevent damage and protect the brain from outside particles[52]. In some applications, the overlying cortical tissue can be removed to prevent light scattering from thick brain tissue[53]. While this approach allows us to obtain high resolution images of deep brain tissue, this method is considered highly invasive as a large area of tissue is removed.

Cranial windows have been effective in a range of applications including the study of synaptic plasticity, calcium dynamics, and neuroinflammation in disease models. This imaging technique has been successfully applied to a variety of transgenic mouse

models and injectable dyes. Dendritic spines, involved in synaptic plasticity, have been longitudinally imaged to demonstrate their stability and loss in both naïve and disease models of mice [53]–[56].

Calcium dyes can be injected into the desired imaging area and a cranial window can be placed to reveal the activity of dense neuronal networks, offering method that is less invasive than electrophysiological recordings [57]–[59]. To look at calcium dynamics long-term, cells can be chronically labeled with viral vectors, again offering an advantageous approach over chronically implanted electrodes, such that it eliminates degradation caused by cell death and gliosis at the electrode tips [60]. Cranial windows have been further developed to be stable over time allowing the imaging of neuronal activity in awake mice in order to map behavior-related neuronal dynamics [61], [62].

In models of stroke, cranial windows have been used to examine brain dynamics following injury. Longitudinal *in vivo* imaging of apical dendritic arbors demonstrated before the induction of stroke, dendritic arbors are relatively stable and following injury, significant remodeling occurred as shown by dendritic tip growth and retraction [63]. Microglia dynamics have been longitudinally studied *in vivo* with the use of cranial windows, demonstrating their role and tendency to become activated, proliferate, and interact with the blood vasculature after models of stroke [64]–[66] .

2.3.3   Thinned Skull Windows

The use of thinned skull windows with multiphoton microscopy is a popular technique, which limits the amount of biological tissue the laser travels through while simultaneously protecting the brain from external factors, such as temperature and pressure [67]. When the skull is removed, as in the case of cranial windows, glia cells

become activated and can lead to changes the brain dynamics, inherently effecting the scientific study. Thinned skull windows have the advantage of decreased inflammation [68]. In the neocortex, thinned skull windows have allowed researchers to visualize dendritic spines as well as perform longitudinal imaging in which the changes in dendritic segments are imaged in layers 5 of the brain [54], [69].

A disadvantage with thinned skull windows is the need to re-perform skull thinning as the bone regrows over time. To circumvent this disadvantage, researchers have developed methods, such as reinforcing the thin skull with transparent cement and glass windows, allowing visibility up to 250 μm below the pial surface over a 3 month time period [70]. An additional disadvantage to this technique is the skull is considered a highly chaotic tissue and light will be severely distorted before reaching the point of focus. Wave fronts can be controlled with adaptive optics and fluorescence signal can be increased and subsequently increase the field of view area [71]. The depth of the field of view is limited and inherently based on the thickness of the skull after thinning. In order to obtain high resolution images, the skull thickness should be between 15-25 μm, as this can potentially lead to damaged brain tissue [72].

Thinned skull windows have been used to study a variety disease models, including ALS, Alzheimer's, and stroke. In ALS, the thinned skull technique was used to visualize excitotoxicity by identifying dendritic blebbing [73]. In Alzheimer's, this method is used to successfully image senile plaques in living animals in the same brain region over a period of days to months [74], [75]. Brain dynamics have been studied following various models of stroke. Calcium transients are associated with sensory processing and rewiring months after an ischemic stroke [76]. A longitudinally used

thinned skull window revealed increased microglia reactivity and the entrance of circulating cells into the parenchyma because the blood brain barrier became compromised [77].

While both cranial and thin skulled windows have provided insights in various disease models, the majority of data collected has been limited to the upper regions of the brain. While some *in vivo* information has been collected in lower levels of the cortex [53], it typically involves the removal of brain tissue, which can interfere with data collection and analysis. As a result, optical devices are needed that can extend the imaging depth and provide longitudinal data while causing minimal brain impairment.

2.3.4   Gradient Refractive Index Lenses

Light scattering from brain tissue is a challenge presented when attempting to image neural activity in the brain. Deep regions of brain have remained inaccessible, as they are beyond the working distance of current modalities. To circumvent this challenge, gradient refractive index (GRIN) lenses can be used *in vivo* to explore deeper regions of brain. GRIN lenses can provide the high cellular resolution needed to better understand brain activity and to study the progression of brain trauma.

GRIN lenses, a class of micro lenses, are glass cylinder, biocompatible lenses used to examine deep brain structures [14], [15], [78]. The lenses use a negative gradient in the refractive index of glass from the center of the lens to the outside edge to bend and focus light. The lenses have flat surfaces which allows for ease in manufacturing a system to implant [79]. The glass is inhomogenously doped with cation species, with the highest density of cations at the central axis of the lens and declining radially towards the outer edge. Total internal reflection occurs gradually as light passes from the central

regions to the periphery. As a result, the light will travel through the lens in a sinusoidal path [80].

GRIN lenses are characterized by their pitch, length, or numerical aperture. The pitch represents the number of internal images made inside the lens, determined by the refractive index profile. GRIN lenses can be up to tens of centimeters long, which is more than capable of imaging in animals and even humans. When GRIN lenses are combined with multiphoton microscopy, they can resolve optical planes far from the surface of the lens which is beneficial because implantation of the lens may cause mechanical damage or may initiate an immune response next to the lens [14].

GRIN lenses alone generally have a numerical aperture, which is related to the resolving power, of 0.5. While these lenses have enabled microendoscopes to be used in small animal research applications, the optical resolution is not comparable to conventional microscopy. Single GRIN lenses have several optical drawbacks, such as a highly elongated point spread function, which hinders the ability to collect high resolution three dimensional image stacks [78], [79]. GRIN lenses can be optimized by combing additional refractive index matched elements leading to high numerical apertures and allowing for the collection of high resolution data that are needed in studies such as neuronal plasticity and resident immune cell response[78], [81].

GRIN lenses have been used in a variety of applications to demonstrate their functionality *in vivo* and to collect data concerning neural networks. GRIN lenses have been used to visualize the activity of deeply buried neurons in the substantia nigra, lateral hypothalamus, and hippocampus [48], [51], [52]. Lower levels of the prefrontal cortex can be imaged with minimal glia scarring and without interrupting the animal's behavior

[14]. Longitudinal images of deep brain structures with GRIN lenses have revealed the extreme stability of dendrites and rare instances of their alterations[83]. In order to image calcium transients in awake and behaving mice, GRIN lenses have been used in endoscopes and ultrafast camera systems [84], [85], establishing their potential to be used to study not only resting brain dynamics.

GRIN lens technology has been useful in collecting longitudinal data with high cellular resolution. This technology can be further used to study the progression of high incidence brain injuries, such as stroke and traumatic brain injury. A GRIN lens can be implanted long-term into transgenic mice without interrupting animal behavior [14], offering an opportunity to study both brain structural changes and behavior following injury in the same mouse. Additionally, GRIN lens technology would be useful as a preclinical tool. It is important to understand when and how candidate therapies are affecting the outcome, and if this outcome is long term. Since GRIN lenses can collect both spatial and temporal data from the same mouse, they offer a unique opportunity to accomplish this goal.

2.4 Candidate Therapies for Brain Injury

2.4.1 Minocycline

Finding an effective treatment for traumatic brain injury remains a challenge in the scientific community. Despite the ongoing research and the substantial investments in this field, traumatic brain injury still remains a major source of disability in the world. Both the mechanical and cellular damage disrupt cognition and everyday life for individuals suffering from a traumatic brain injury, and as a result it is imperative to find a treatment which can limit and reverse the deleterious effects of the injury. An FDA

approved drug, minocycline, has shown preclinical potential as a therapeutic when administered acutely (< 24 hr) following a traumatic brain injury.

Minocycline belongs to the tetracycline family of antimicrobials, is considered a broad spectrum antibiotic, and has been in use for over 30 years. Minocycline can be administered both intravenously and orally, and it has a long half-life [86]. Because it is also a highly lipophilic molecule, it can easily pass through the blood brain barrier leading to an accumulation in the cells of the central nervous system [87]. It can be used chronically in high doses and is well tolerated in humans [88].

The antibiotic effects of tetracyclines has been known since the early 1940s, and recently, their non-antibiotic properties have been studied, including their anti-inflammatory, antiapoptotic, and antioxidant benefits. Minocycline has been shown to be beneficial for many inflammatory diseases and has emerged as effective in neuroprotection and confirmed in experimental models of ischemia and traumatic brain injury [86].

At high dosages, minocycline inhibits inflammatory cells, including microglia, T cells, and neutrophils. It has also been shown to block both caspase-dependent and independent apoptosis, inhibit metaloproteases, and scavenge for reactive oxygen species. As a result of these properties, the drug has been studied at administration between 45 minutes and 4 hours in several pre-clinical models of TBI [89].

Early administration of minocycline has shown to suppress markers of neuroinflammation, namely activated microglia and macrophage densities, which can account for neuronal loss. Early inflammatory outcomes were examined following TBI and it was found that at both one and four days after a closed head injury model, the

number of activated microglia in minocycline-treated animals was significantly less than in the saline treated group, demonstrating the early protective effects of minocycline [90].

In a closed head injury model using the weight drop method, minocycline was administered at 5 minutes post injury and long term histopathological outcomes were studied. Three months after injury, minocycline was shown to protect the volume (ipsilateral/contralateral) of the corpus callosum, striatum, and lateral ventricle when compared to naïve mice. Additionally, the treatment reduced the number of both GFAP+ and CD11b+ cells, which are markers for astrocytes and microglia, respectively. The results demonstrate than when minocycline is administered acutely following closed head injury, it exhibits a long term, protective effect [91].

Another study used the same model and minocycline treatment set up to examine both the drug's acute and chronic effect on preclinical neurological outcomes. One of the best markers for diffuse axonal injury is the accumulation of β-amyloid precursor protein (β-APP). This protein accumulates within hours following traumatic brain injury because disrupted axonal protein transport causes it to pool at the site of impaired tissue. Following TBI, the number of β-APP labeled axons increased markedly, independent of treatment, signifying that the mechanical damage occurring during diffuse axonal injury cannot be protected by the drug. However, minocycline did decrease the number of CD11b+ cells, demonstrating its effect on neuroinflammation [92].

Memory impairment, anxiety, and depression manifest following traumatic brain injury, a result of the mechanical and cellular damage. Minocycline, when administered acutely improves recognition memory when evaluated long term [93]. Additionally,

minocycline improves both acute and long term functional behavior after a closed head injury in mice, as compared to vehicle treated mice [92], [94].

Minocycline is neuroprotective when administered between one and four hours, but it is not always possible to treat individuals in such a short time window. Therefore, it is necessary to determine if the drug is still effective when administered in a longer therapeutic window. Additionally, the studies conducted have looked at fixed brain slices, which are a snapshot it time. It is not only necessary to identify the efficacy of minocycline treatment, but also how it affects the progression of axonal damage.

2.4.2   Annexin A1

Annexin A1 (AnxA1) was first discovered in the 1970s and is a 37-kDA member of the annexin superfamily. This molecule is expressed in subcellular granules of monocytes and neutrophils [95]. AnxA1 modulates various biological events, including both acute and chronic inflammation [96]. AnxA1 causes L-selectin on neutrophils to shed and leukocytes to detach from the endothelium, contributing to the protein's ability to restrict transmigration from the vasculature to tissue that is seen in inflammation. Anx1 must be internalized to exhibit its anti-inflammatory effects. When cells become activated, AnxA1 is released. Following release, AnxA1 becomes cleaved causing it to either act as a pro-drug or produce homeostasis by limiting the action of AnxA1 [97].

As a result of reperfusion injury, chemokines and cellular adhesion molecules (CAM) are expressed, which causes leukocytes to migrate into the damaged tissue. Additionally, resident microglia become activated, leading to excessive inflammation. When this occurs, endogenous strategies involving the glucocorticoid regulated protein, AnxA1, are initiated by the immune cells. AnxA1 modulates the inflammatory response

by targeting the formyl peptide receptor 2 (FPR2) as demonstrated by the administration
of a known antagonist, Boc2. When Boc2 is administered simultaneously with AnxA1,
the anti-inflammatory properties of AnxA1 are negated [98]. To further establish the anti-
inflammatory effect of AnxA1, an AnxA1-/- mouse was developed and has demonstrated
that when AnxA1 is absent, inflammation is exacerbated [99]. When exogenous AnxA1
was administered to animals undergoing ischemia/reperfusion injury, leukocyte adhesion
and rolling was significantly decreased, reducing the inflammatory response normally
seen in this disease model [96], [100].

AnxA1 is endogenously expressed in microglia and it has been demonstrated, *in
vitro,* that exogenous AnxA1 promotes the phagocytosis of apoptotic neurons and
promotes the resolution of inflammatory microglial activation. This demonstrates AnxA1
has a fundamental role in brain homeostasis and the administration of exogenous AnxA1
may be potentially effective as a therapeutic for neuroinflammation [101]. Further
research is needed to determine if AnxA1 exhibits this same protection *in vivo* following
ischemia/reperfusion.

2.4.3   PgP-pβ-Gal

Therapeutic nucleic acids capable of changing gene expression levels may be
advantageous in the treatment of axonal regeneration. In gene therapy, vectors containing
genetic material capable of expressing a therapeutic gene are delivered intracellularly.
Viral vectors are commonly used to deliver and achieve transfection, but they lack
specificity, can cause an immune response, and lead to inflammation. In injuries such as
stroke and TBI, inflammation has a key role in further mitigating damage. Introducing
therapeutic compounds that further cause inflammation would be inefficient, and

therefore, it is necessary to use a transfection system that eliminates these concerns and can achieve delivery in the central nervous system. Non-viral vectors are being developed, such as plasmid DNA and siRNA. These vectors are formulated with cationic lipids or polymer carriers, which are not only easy to manufacture at a large scale, but reduce off target effects and diminish an inflammatory response [102].

A synthetic polymer that has shown promise by its ability to transfect DNA vectors in the CNS is polyethylenimine (PEI). However, in the presence of serum, the transfection efficiency of PEI is low and cytotoxic. To overcome these limitations, polymeric micelles for combinatorial drug/gene delivery are being developed. The cationic amphiphilic copolymer, poly(lactide-co-glycolide)-graft-polyethylenimine (PgP) has been synthetized as an efficient vector for stable intracellular delivery of nucleic acids. PgP micelles loaded with reporter genes and siRNA (PgP polyplexes) can transfect cells in the rat spinal cord *in vivo* as well as reduce cytotoxicity as compared to conventional PEI. As a result, PgP may be an effective choice for gene delivery [103].

Since PgP has shown to deliver DNA to the normal rat spinal cord, the ability of PgP to deliver siRhoA in a rat compression spinal cord injury model was investigated. The results demonstrated that after local injection of the micelles loaded with siRhoA, apoptosis and astrogliosis were reduced. Furthermore, axonal regeneration was increased as compared to the untreated SCI animal groups [104]. These results are encouraging, and PgP complexed with siRhoA and other therapeutic biomolecules may be a candidate for treating diffuse axonal injury (DAI). DAI is a progressive injury and can result in widespread axon degeneration and microglia activation. Based on the PgP's ability to carry drugs that reduce inflammation and increasing axonal regeneration, it may be an

effective therapeutic in not only delivery of anti-inflammatory drugs but also reversing the progressive damage.

CHAPTER 3

CHAPTER 4

TRIO PLATFORM: A NOVEL LOW PROFILE

IN VIVO IMAGING SUPPORT AND

RESTRAINT SYSTEM FOR MICE

4.1   Introduction

Laser scanning confocal microscopy through cortical windows has opened upper layers of the mouse brain for high resolution, time-course, *in vivo* imaging [105], [106], and multiphoton microscopy (MPM) has facilitated *in vivo* imaging of the olfactory bulb [107] and lower layers of the cortex, up to several hundred microns deep [79]. Additionally, implanted GRIN lenses have extended the reach of MPM to lower cortical and subcortical regions of the murine brain [78], [79], [83] and small prisms have provided vertical views of entire cortical columns [108]. These technological achievements have met at a crossroad with the rapid growth in the number of transgenic mouse strains to achieve unprecedented spatiotemporal resolution of dynamic processes in the brain. Transgenic mice with fluorescent proteins expressed under specific genetic promoters have permitted cell-type specific identification of targeted cell populations. Investigators have used *in vivo* imaging on these mice to observed processes such as changes in dendritic spine density [109], migration and activation of microglia [110], growth of brain tumors [83], [106], and the dynamics of a brain tumor microenvironment

[111]. Additionally, genetically encoded calcium sensitive fluorescent proteins [112], [113] and dyes [51], [112] have revealed the activity of local and large scale neuronal networks [114]. Furthermore, by counterstaining the vasculature, blood flow rates have been determined [79], [115], and vessel permeability and leukocyte trafficking have been observed [116]. The ability to monitor these activities over time in a mouse model has tremendous importance to both basic research and preclinical studies [111], [117]. Yet, the means by which mice are positioned and maintained for imaging has relied primarily on old technology and non-standardized custom made components.

Positioning and maintaining anesthetized mice for imaging over time requires a means to secure the head, maintain the animal's body temperature and facilitate delivery of anesthesia. Securely restraining the animal's head during imaging is essential for reducing motion artifacts from respiration and heart beats [116]. A good restraint system will also optimize the alignment of the imaging region with microscope objective [78], [116]. Repeatable alignment is important for longitudinal experiments and is critically important for imaging through implanted GRIN lenses [118].

Numerous methods of restraining mice via head fixation for *in vivo* imaging have been reported. These mainly include stereotaxic devices [111] many of which are custom fabricated for a particular research lab [106], [107], [116], and involve custom designed stages [113], and custom-made bars or plates (head posts) permanently affixed to the head with customized stage-mounted devices that secure the head post [61], [109], [113], [119]. Several commercially available head immobilization devices are available that can restrain the head for imaging through cranial windows. Examples include the MAG-1 Simple Head Holder Plate for Mice from Narishige International USA, Inc. and mouse

and neonatal rat adaptors from Stoelting Co. and Harvard Apparatus, Harvard Biosciences, Inc. However, these devices are 4 – 7.5 centimeters tall, which is greater than the distance between the stage and the objective lens on some microscope systems. Three-point immobilization devices with ear bars and a bite bar are smaller than stereotaxic frames and will securely immobilize the head, but these have rudimentary adjustments for pitch, yaw, and roll. This limited adjustability makes it difficult to consistently align the head over multiple imaging sessions for longitudinal studies. Some custom head plate and holder systems have a much smaller size and consistent alignment for imaging through cranial windows. Unfortunately, recreating custom components can pose a challenge when attempting to use another lab's protocol. Notably, no low profile, commercially available systems were identified that can achieve the repeatable, sensitive alignment needed for repeated imaging through an implanted GRIN lens.

Gas anesthesia may be used for long *in vivo* imaging sessions to avoid unwanted movement caused by injection of anesthetic agents and to avoid light contamination when opening a shroud to make an injection. However, the nose cones for gas anesthesia are usually configured to mount onto stereotaxic frames and few studies use stereotaxic frames for *in vivo* imaging [106], [111], presumably, because of their large size. Alternatively, a simple plastic cone can be attached to the hose from the vaporizer. The open end of the cone is covered with the top half of a rubber balloon with a slit in it. The nose of the mouse is placed in the slit of the cone, but if the slit is not properly sized, anesthetic gas can leak into the room (personal observation) unless a scavenger system is installed. This system increases the amount of space occupied by components on and around the microscope stage and can substantially increase setup time.

Prolonged anesthesia will cause a drop in body temperature to hypothermic levels if left unchecked [120]. Two commonly used types of systems are electrical, thermostatically controlled resistive heating plates or pads and warm water pads. Electrical plates are thin and fit well under microscope objectives. Both the electrical plates and pads pose a risk of overheating the animal if the temperature probe is improperly placed or it becomes dislodged. Warm water pads use circulating water that is warmed in a reservoir to a set temperature, such as 37˚ C. Its thermostat is located inside the water tank, which greatly reduces the possibility of overheating the animal. Unfortunately, these pads are bulky and raise the height of the mouse by several millimeters or more. They can also be uneven and thus, require the operator to expend additional time to move the pad to achieve proper head alignment. To our knowledge, none of these heating systems provide head fixation. A heating pad with a standard immobilization frame raises the height of the mouse's head to over 7 cm.

4.2   Materials and Methods

4.2.1   TRIO Design and Construction

The system was designed to restrain the head of an anesthetized mouse with a head plate (or head post) attached to the skull and to orient the cranial window so that the flat face of the window is perpendicular to a microscope objective (**Figure 31**). The system was also designed to provide gas anesthesia and to maintain body temperature. The components of the system were designed in SolidWorks (Dassault Systèmes). A MakerBot® Replicator® 2 three-dimensional (3D) printer and poly(lactic acid) (PLA) filament were used to fabricate the system. This manufacturing method minimized development time and costs, allowing for multiple design iterations. The widespread

availability of 3D printers enables other researchers to replicate or modify the design as their experiments require.
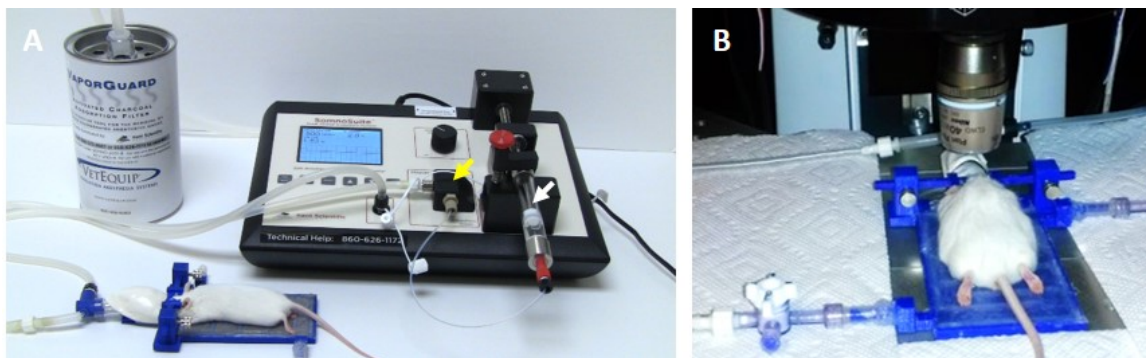
Figure 31. TRIO Platform: an *in vivo* integrated imaging support system. (**A)** TRIO Platform with gas anesthesia supplied by a compact, portable gas anesthesia system (SomnoSuite®, Kent Scientific Corp.). Isoflurane is supplied from a syringe (**white arrow**). The integrated digital vaporizer (**yellow arrow**) is much smaller than traditional vaporizers which markedly reduces the amount of anesthesia used for surgeries and for imaging sessions. (**B)** Anesthetized mouse positioned and warmed for imaging using the TRIO Platform on the stage of a multiphoton microscope. The overall height of the base plate with circulating warm water and the mouse head is only 20 mm. This relatively small height will enable its use on a wider range of microscopes. (The white paper towels around the platform were used to block reflections from the lights used for this photo. They are not required for imaging.) The compact anesthesia system can be placed to the side of the stage within the microscope enclosure or outside of the enclosure [15].

4.2.2   Warm Water Plate

A 3D printed plate with an interior, serpentine channel for warm water circulation serves as the central hub of the system (**Figure 32**). The plate was designed with a low-profile rectangular geometry that is 5 mm high, 115 mm long and 61 mm wide. Water inlet and outlet ports were placed at opposing corners and fitted with standard tube fittings to allow attachment of polymer tubing to deliver warm water and recycle it back to the warm water reservoir. Water in the reservoir was maintained at 40° C. A flat cover was attached to the top of the water chamber with cyanoacrylate adhesive (Loctite). The entire chamber was sealed with a silicone adhesive (Kwik Sil, World Precision

Instruments, Sarasota, FL, USA) to prevent leaks. This system has been used for 9

months without any water leaks.
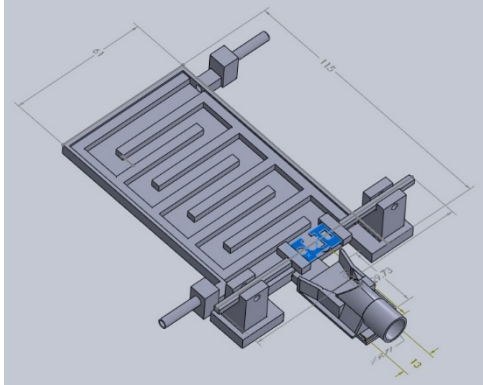
Figure 32. Integrated system with the top cover of the base plate removed to show the
serpentine water channel. Parts were 3D printed and designed in SolidWorks®.
Dimensions are in mm [15].

4.2.3   Anesthesia Nose Cone

        To deliver a gaseous anesthetic, a slotted tongue (**Figure 3-3A, arrow**) was glued

to the front of the printed plate and a 3D printed nose cone (**Figure 3-3B-C**). The channel

under the nose cone (**Figure 3-3B, arrow**) slides into the tongue's slot and is held in

place by a triangular catch, preventing it from being dislodged accidently. The cone can

be removed for cleaning or when a non-gaseous anesthetic is being used.
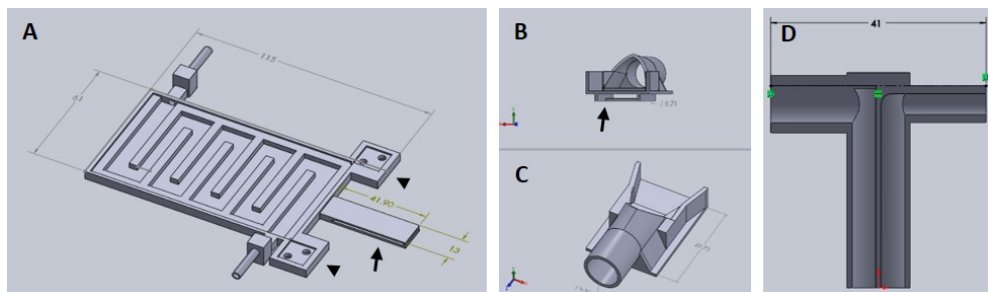
Figure 33. Components of TRIO Platform. A. This view shows features of the base plate
that cannot be seen in **Figure 32**, such as the extensions of the base plate for attaching the
head plate holder posts (**arrowheads**) and the slotted tongue (**arrow**) for attaching the
nose cone. (**B-C**) Two views of nose cone design. Channel under nose cone in (**B, arrow**)

sides into a slot in the tongue (**A, arrow**). D. Gas inlet (right side) and outlet (left side) are integrated into one piece that attaches to the tubular component of the nose cone (**C, arrow**). Dimensions are in mm [15].

A t-shaped gas delivery fitting also printed with PLA (**Figure 3-3D**) is connected

to an opening in the cone (**Figure 3-3C, arrow**). One side has a tube fitting that connects

to the inlet hose from a compact gas anesthesia system. The other side connects to the

hose that returns gas to the anesthesia system where the scavenged gas is trapped in an

activated charcoal filter. Both hoses are made of silicone tubing (FDA-grade, Platinum-

cured silicone tubing, 1/8" ID x 3/16" OD, VWR International). We used a SomnoSuite™

anesthesia system (Kent Scientific Corp.) because it fits easily within or near the housing

that surrounds our multiphoton microscope, which was a Vivo™ 2-Photon Microscopy

Workstation (Intelligent Imaging Innovations, Inc., also written as 3i, Inc.). To make

isoflurane delivery more efficient and minimize leaks of anesthetic into the workspace,

an elastomer shroud (AC-COAX-Balloon, Kent Scientific Corp.) is secured over the

opening of the nose cone with a piece of ½-wide plastic tape (**Figure 3-4, arrow**). The

elastomer covering can be lifted temporarily to confirm that the animal's nose is place

fully in the cone. A medium-sized rubber balloon with the neck piece removed will work

equally as well. We have also used a piece of 18-gauge wire, instead of tape, to secure the

shroud to the gas delivery tube. The shroud was easily replaced when the edges of the

rubber dried and cracked after several months of use.
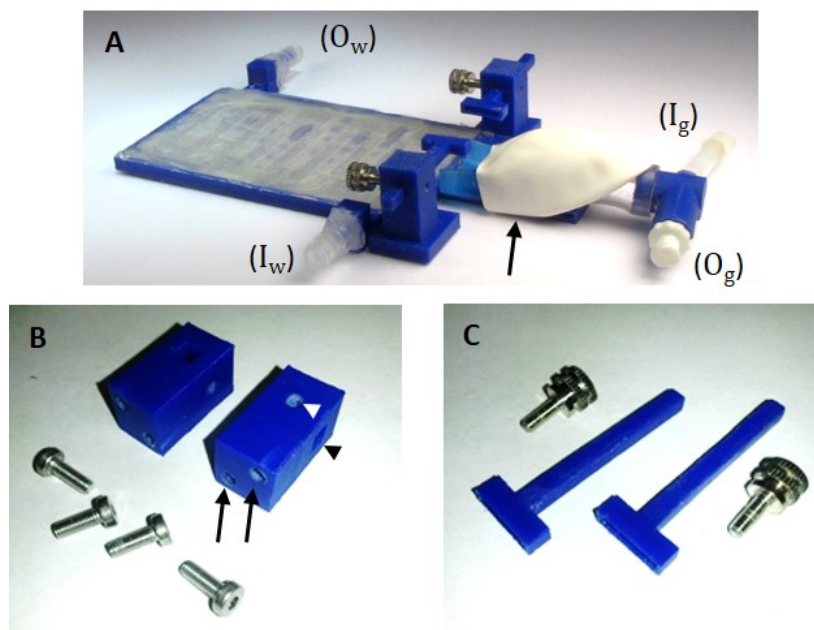
Figure 34. TRIO Platform 3D-printed system. **(A)** Assembled system with tube fittings for attachment to inlet (I_w) and outlet (O_w) water lines and Luer lock fittings for attachment of inlet (I_g) and outlet (O_g) tubes from a gas anesthesia system. The elastomeric shroud is held onto the nose cone with plastic tape from the underside of the device (**black arrow**). **(B)** Head plate holder posts and machine screws. Two screws are placed in holes in the base plate and screwed into tapped holes in the posts (**black arrows**) to attach the posts to the base plate. A square hole in the post holds an arm of the head plate holder (black arrowhead) and a round taped hole in the post (**white arrowhead**) holds a set screw (**C**) to secure the position of the arm in the square hole. **(C)** Head plate holders with the accompanying screws that secure the head plate holders to the holder posts [15].

In order to add a head plate holder securely to the base plate, the two front corners of the base plate have two 21 mm square extensions that are printed as part of the bottom plate (**Figure 3-3A, arrowheads**). The posts are attached to these extensions with 3-mm hex head machine screws 8 mm in length. The posts are rectangular columns, 22 mm in height. Each post has two 8-mm long holes in the bottom (**Figure 3-4B, black arrows**) that are tapped to match the thread pitch of the 3-mm hex head machine screws that hold the post to the base plate. Each post also has a square hole (4 mm x 4 mm, **black arrowhead**) that holds the long arm of a head plate holder (**Figure 3-4C**), and one 3-mm

circular hole (**white arrowhead**) that is tapped to match the thread pitch of a 3-mm set screw with a knurled head for hand tightening. The long arm of each of the two head plate holders has a square profile that fits snugly into the square holes in the holder posts. The arm can be securely positioned in the post by tightening the set screw by hand until the arm does not move with gentle pressure. The screw must not be overtightened as overtightening will cut into the plastic and shorten the life of the holder. The t-shaped end of each bar has a 1-mm high by 1-mm deep by 12 mm long rectangular cavity (**Figure 3-3, inset**), which holds the outer end of a head plate. Together, both bars securely hold the head plate and orient it such that the cranial window is perpendicular to the laser beam.

4.2.4 Head Plate Assembly

SolidWorks and 3D printing with a PLA filament (G-Star Technologies) were used to design and fabricate head plates, respectively. We used a polymer head plate instead of a metal plate or bar to minimize the mass of the plate and permit easy modification of the number of ports and their placement. Minimizing the mass of the head plate, which was about 0.2 g, was important for our work because many of our mice are used for behavioral experiments in between imaging sessions [117].

The head plates are 9 mm long, which is long enough to have free ends to attach to the head plate holders (**Figures 3-2 and 3-5**) and short enough to provide free movement when the mouse is awake (**Figure 3-6**). A section at the caudal edge is cut out, providing an opening for installation of an injury hub which was used for midline fluid percussion experiments to induce traumatic brain injury [121]. If the hub is not needed, the cutout provides additional surface area for applying adhesive. A second

cutout (**Figure 3-5**), provides a place to attach a 5 mm diameter glass cover slip cranial window.
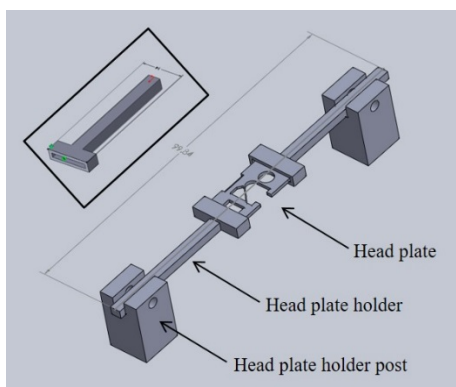
Figure 35. Two head plate holders grip each side of a head plate. The head plate is permanently attached to the skull of a mouse. Head plate holder posts position the holders and head plate above the base plate with sufficient space for positioning the head of an adult mouse (see **Figure 3-1B**). The entire assembly is 22 mm tall, 14 mm wide, and just under 100 mm long. **Inset.** Detailed view of a head plate holder. The long arm has a square cross section (3.7 mm x 3.7 mm) that fits into a square hole in a holder post. One end of the head plate fits into the slot in the t-shaped end. The slot is 12 mm long, 1 mm wide and 1 mm deep. The overall width is 14 mm and the overall length is 41 mm. These dimensions can be adjusted for different sized head plates [15].

Figure 36. Mouse with an implanted GRIN lens and permanently attached head plate. Prior to surgery, a GRIN lens was affixed to a 5 mm diameter cover slip which was then glued to the head plate. The lens was implanted into the brain by lowering it through a craniotomy and advancing it into the brain as the head plate was slowly lowered to the skull (see **Figure 3-7**) [15].

Optical adhesive (Number 71 Adhesive, Norland Products, Cranbury, NJ, USA) is used to secure the cover slip to the head plate. A thin bead of adhesive (~1-mm wide) is applied around the edge of the cover slip and then gently pressed against the bottom of the head plate using blunt, curved forceps so that the adhesive forms a continuous seal. The head is placed upside down for this step. The optical adhesive is cured using a UV lamp according to the manufacturer's instructions. Because UV light is harmful, the operator must shield eyes and skin from UV light at all times. It is important to confirm that the coverslip is parallel to the bottom of the head plate which will ensure optimal alignment of the cranial window for imaging. If the resolution of the printer is not precise enough, the cover slip may not seat parallel to the head plate. In this case, a 5-mm end mill and standard machining techniques can be used to mill the area for attachment.

For deep brain imaging in lower cortical layers 4-6 and subcortical regions, a GRIN lens should be attached to the cranial window, a 5-mm diameter glass cover slip. The attachment of the GRIN lens to a cover slip has been described in our previous work [78]. Because the cover slip is mounted on the underside of the head plate, the head plate should be placed upside down and the coverslip-GRIN lens assembly should be positioned over an appropriate opening in the head plate with the free end of the GRIN lens pointed up. The operator should use a stereomicroscope or large magnifying glass with ample lighting to clearly visualize the forceps and lens and to ensure that the forceps do not touch the GRIN lens. The forceps can transfer glue and debris onto the lens which could degrade image quality. It is also possible to chip the edge of the lens or to break it off the cover slip with sufficient pressure. In our experience, workers become proficient at making these assemblies in about 2-3 procedures.

A clean, dust-free or low-dust work area is necessary when the cover slip is attached to the head plate. This work area reduces potential sources of infection and maintains optical clarity of the window and/or GRIN lens. Components can be cleaned with 70% ethanol prior to assembly and any dust particles can be removed before applying adhesives. Additionally, the UV light used to cure the adhesive disinfects the exposed surfaces. Assemblies should be transferred after curing using clean forceps and stored in clean, covered containers. Prior to implantation, assembled head plates should be exposed to UV light for 15 minutes on each side or soaked in 70% ethanol for 15 minutes to disinfect the surfaces. They should be transferred to the surgical site in sterile containers. Autoclaving is not recommended as it might warp the polymer head plate. Ethylene oxide gas was not tested as a means of sterilization.

Because the head plate design is easily modified in SolidWorks® and plates are quickly printed with an inexpensive polymer, making changes for different types of imaging experiments is quick and economical.

4.2.5   Printing the Platform

All polymer parts were designed in SolidWorks® and produced on a Replicator 2® (MakerBot®) 3D printer. All pieces were printed at 100% fill with a 0.1 mm layer height. (Note: Some 3D printers cannot print as small as 0.1 mm/layer.) Optimal 3D printing of the components of this system requires correct printing orientation. Printing in another orientation could result in the printer program adding a meshwork of polymer "supports" to overhanging areas. Without supports, overhanging areas would deform under the force of gravity. These supports could occlude channels and slots that should be

left open. Parts with open areas can be oriented such that supports are not needed. We optimized the orientations for printing each part, as follows:

1. The base of the platform was printed right side up, with the bottom of the device flat against the platform, with no supports.

2. The top of the device was printed on its widest side (i.e., flat) with no supports.

3. The slotted tongue was printed on its thinnest side so that the slot was perpendicular to the printer platform. No supports were used.

4. The nose cone was printed with the cylindrical part against the platform, with supports

5. The gas delivery fitting was printed in two halves, with the inside edges flat against the platform, with no supports.

6. The head plate holder post was printed laying on its longest side, so that the slot was perpendicular to the platform, and with no supports.

7. The head plate holder was positioned so that the long arm was pointed straight into the air and printed with no supports.

4.2.6   Animals for *In Vivo* Imaging

White, GFAP-GFP+ lab mice (FVB/N-Tg(GFAPGFP)14Mes/J) were obtained from Jackson Labs. Louisiana Tech University IACUC guidelines were followed for animal housing with lighting in a 12 h on – 12 h off cycle. Food and water were provided *ad libitum*.

4.2.7   Surgery

All surgical and imaging procedures were approved by the Louisiana Tech University Institutional Animal Care and Use Committee. Every effort was made to

minimize pain and suffering. A noxious stimulus consisting of two toe pinches every 15 min was used to confirm that animals were in a surgical plane of anesthesia during surgical procedures. Mice were monitored for recovery until sternal recumbency was overserved. To minimize post-surgical pain, Ibuprophen, children's suspension (30 mg/kg/day) was dissolved in the animal's drinking water for 60 - 72 hours following surgery. Mice were also monitored daily for signs of distress or poor health. The end point for mice was perfusion (see histology section).

Prior to performing any procedures, mice were allowed to acclimate to the room in their home cage for at least 30 minutes. For surgery, a mouse was initially anesthetized with 3% isoflurane (VEDCO) in the induction chamber of a SomnoSuite® small animal anesthesia system (Kent Scientific Corp.). A mixture of ketamine (10 mg/kg) and xylazine (1 mg/kg) in sterile saline was injected intraperitoneally after induction of anesthesia using the isoflurane chamber. This mixture was used to give surgical staff time to prep the animal and position it in the stereotaxic frame. Once secured in the frame, the mice were maintained on 1.5% isoflurane. Ophthalmic ointment was placed on the eyes and the fur over the scalp was cut with iris scissors. The mouse was then placed in a Benchmark stereotaxic frame with a nose cone for gas anesthesia (Leica Biosystems) and a mouse and neonatal rat adaptor (Stoelting Co.). Anesthesia was maintained using 1.5% isoflurane supplied by the SomnoSuite® system. Body temperature was regulated and heart rate and SpO2 were monitored using a PhysioSuite® System (Kent Scientific Corp.).

Aseptic surgery was performed to install either a cranial window or a GRIN lens mounted on a cranial window, as previously described [78], [117]. Briefly, after

confirming the mouse was in a surgical plane of anesthesia using noxious toe pinches, an incision was made in the scalp and connective tissue was cleared.

Under a surgical microscope, a micro drill was used to make a 1 mm diameter craniectomy at selected rostral and lateral distances with respect to bregma and the midline, respectively. The exposed dura was removed and a GRIN lens (mounted on a head plate, as described in the head plate assembly section) was implanted through the craniectomy.

Before the head plate was attached, a thin layer of cyanoacrylate adhesive (Krazy Glue®) was applied to the skull [72], [122]. To position the head plate for implanting it was held by a set of two 3D-printed head plate grips (**Figure 37C**) mounted to the end of a steel probe holder (**Figure 37B**; Stoelting Co.) that was attached to a stereotaxic frame (**Figure 37A**). The rostral-caudal and medial-lateral direction controls of the stereotaxic frame were used to guide the lens to the desired stereotaxic coordinates. The probe holder control was then lowered until the GRIN lens was touching the pial surface of the brain. After this, the assembly was lowered at a rate of 0.1 mm/min to the desired depth into the brain. Once the final depth was reached, cyanoacrylate glue was applied around the head plate and in any holes in the head plate that were not used for the window, GRIN lens, or other devices. For some animals, we left the large central hole open for later installation of an injury hub for inducing a traumatic brain injury using midline fluid percussion [121]. Stereotaxic coordinates will vary depending on the location of the brain region for imaging. Insertion depth is limited by the length of the GRIN lens and the angle of insertion.
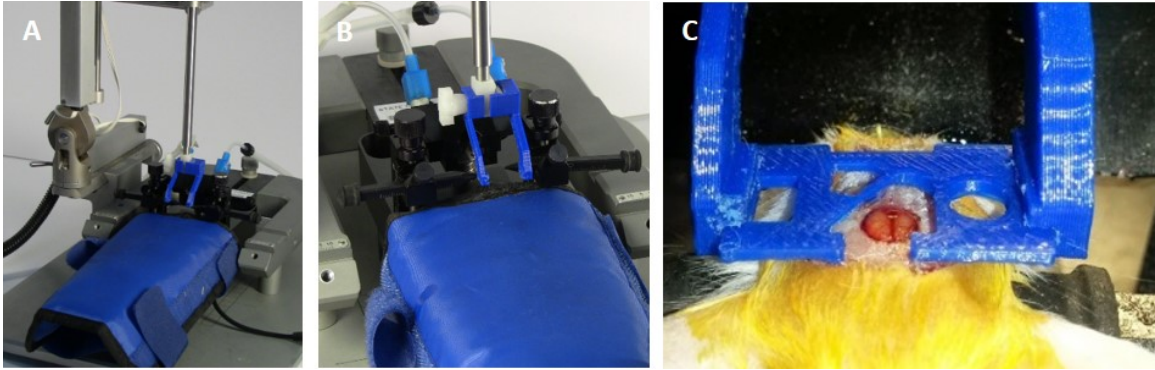
Figure 37. Probe holder with custom grips for surgically attaching head plate. The head plate is held by a 3D printed head plate grips that are attached to the end of a standard probe holder for a stereotaxic device. (**A**) Probe holder with custom grips attached. (**B**) View showing details of grips. (**C**) Grips in use during surgery to attach a head plate. The cut-out in the head plate around the craniotomy provides room to attach an injury hub for a fluid percussion injury, however, a glass cover slip can be attached to this area for use as a cranial window, or it can be used for applying additional adhesive, if desired. For our experiments, a GRIN lens is attached to a round glass cover slip that is glued under the opening that is just rostral and to the left of the craniotomy. The lens is lowered into a separate craniotomy (not visible in this photo) as the head plate is lowered. [15]

It is important that the nose of the mouse is tilted upward for GRIN lens implants in rostral regions of the brain; otherwise the lens will not fully insert into the brain before the back of the head plate stops against the upper curve of the skull. To raise the nose so that the skull is more parallel with the head plate, the height of the bite bar on the stereotaxic frame can be increased. Likewise, for lateral implants the head should be tilted to the side to avoid having the head plate hit the upper curve of the skull and stop before the lens is fully inserted. For slightly lateral implants, this can often be accomplished by slowly adjusting one ear bar higher than another. However, adjusting an ear bar to access more lateral positions requires a larger angle and will result in the ear bar coming out of the ear canal. For these insertions, it will be necessary to adjust the angle of the stereotaxic arm that holds the probe holder. (Note: Pressure should never be applied to one side of the head plate to force it to seal completely against the skull as this

would cause the end of the GRIN lens to move rapidly in an arc through the brain, damaging a much larger area of tissue than a proper, linear insertion path.) When the lens is being implanted in one of these special areas, it is best to check the head angle or the angle of the stereotaxic arm by lowering a head plate without a lens to the skull and adjusting the angles for implantation before attempting to implant a GRIN lens.

4.2.8   Imaging

After acclimating to the room in their home cage for at least 30 minutes, mice should be anesthetized in an induction chamber under 3% isoflurane. The heater for the water reservoir-pump system should be turned on about 20 minutes prior to inducing anesthesia. When vascular counterstaining is desired, a dye such as Texas Red-Dextran [123] can be injected via a lateral tail vein [79]. After anesthesia is induced, the mouse should be placed in the TRIO Platform. Light anesthesia can be maintained using 1% isoflurane.

Immediately prior to moving the mouse to the microscope, the coverslip should be cleaned with 70% isopropyl or ethyl alcohol. This cleaning can be done under a stereomicroscope or large, lighted magnifying glass. Once the window is cleaned, the TRIO platform and compact anesthesia system are brought to the microscope. The head plate is positioned under the objective lens of the multiphoton microscope. A fiber optic light on a flexible metal shaft can be used to illuminate the head plate and glass window for positioning while using the bright field setting on the microscope. For repeated imaging in mice with identical head plates, two to three guide bars can be fastened onto the microscope stage that will automatically position the platform for imaging. We have not noticed any movement of the platform over imaging sessions as long as 2 hours. The

platform could be taped into place if procedures are performed during the imaging session that might move the platform.

To test our system for *in vivo*, multiphoton imaging, we used GFAP-GFP mice (The Jackson Laboratory) with an implanted GRIN lens, as described in the surgical section. Aligning a GRIN lens for imaging was a more rigorous test of our system than aligning a cranial window. I*n vivo* images were acquired with a Vivo™ 2-Photon Microscopy Workstation (3i). To focus on the implanted GRIN lens, we used a 40X/0.6 NA air objective with a correction collar (Nikon), as previously described (Murray and Levene, 2012). GFP was excited using a Chameleon multiphoton laser (80 MHz, Coherent) tuned to 890 nm and emitted light was filtered using a 525/40 nm bandpass filter (Brightline®, Semrock, Inc.). For some imaging sessions, the vasculature was stained with Texas red-dextran dye (Life Technologies, Inc.) via a tail vein injection. This dye was simultaneously excited with the 890 nm laser light used for exciting GFP to capture images in the green and red channels at the same time. A 612/69 nm bandpass filter (Brightline® filters by Semrock, Inc.) was used to filter the emission from the red dye. Scanning was controlled by Slidebook, a proprietary program that controls the (3i, Inc.) and performs image analysis and processing. We used a 2 µs dwell time with pixel averaging (4/scan). Power at the sample was adjusted to ~35 mW using a Pockels cell (Conoptics, Danbury, CT, USA) which was controlled using a Slidebook interface.

4.2.9   Images of TRIO System

Images of the TRIO system were acquired by Kayla Ponder and Teresa Murray, PhD.

4.3   Results

4.3.1   Summary of Performance

The TRIO platform *in vivo* integrated imaging support system (**Figure 31**) has

been used over 40 times. The rigid base plate provided a sturdy, yet thin base for

positioning and holding a mouse under a microscope objective. The elastomer covering

over the nose cone provided increased collection of anesthesia, lowering the percentages

of anesthetic to induce and to maintain anesthesia. It also greatly reduced or eliminated

any odor of anesthesia in the room, which likely reduced exposure of researchers to the

anesthetic. Additionally, the water channels remained clear and the base and water lines

and connections remained water tight. Furthermore, the restraint system successfully

positioned mice ranging from 25 – 55 g with little or no motion artifact from breathing or

heartbeat. Moreover, the alignment was sufficient for the demanding technique of GRIN

lens imaging in which the laser beam must be parallel to the axis of the lens to image

deep brain tissue optimally.

4.3.2   Base Plate Temperature Distribution

Temperature measurements were acquired by Kayla Ponder and Benjamin S.

Kemp. Temperature measurements were taken at the top of the heated base plate at five

equally-spaced positions in the middle of the assembled plate, starting near the nose cone

where the head of the mouse is placed (Position 1), and ending in the section near where

end of the tail rests on the plate (Position 5). A Fluke 62 mini infrared thermometer

(Fluke, Inc.) was used to make these measurements. Three sets of readings were acquired

over 2 days. The first set was taken on Day 1; the second and third sets were acquired on

Day 2. Prior to making measurements, the water in the reservoir-pump system (300

ml/min flow rate) was heated to 40 ˚C, as measured with an immersible glass laboratory

thermometer. The IR thermometer was checked by measuring the temperature of the

water bath, which matched the temperature of the immersed thermometer. After this, the

water inlet and outlet tubes were connected to the base plate via Luer lock fittings and

then the circulating pump was turned on. Temperature readings were taken at 5-minute

intervals for the first 30 minutes and 10 minute intervals from 30 to 60 minutes. On Day

2 the water was drained between Test 2 and Test 3 and the plate was allowed to return to

room temperature (about 22 ˚C). The water reservoir remained heated. For Test 2, the

tubes were connected in reversed positions so that the water flowed in the opposite

direction, as summarized below.

> Test 1: Flow from nose cone to rear

> Test 2: Flow from rear to nose cone

> Test 3: Flow from nose cone to rear

> Temperature increased slightly over the first few time points before it stabilized.

Therefore, only the last 6 measurements (20 – 60 min.) were used to determine the mean

temperature at each position (**Table 31**).

Table 31. Mean temperature at top of base plate. SEM is square error of the mean; n=3
measurements for each position [15].

Position Number	Mean ± SEM (°C)
1	35.1 ± 0.5
2	35.2 ± 0.6
3	35.2 ± 0.6
4	32.6 ± 0.8
5	24.1 ± 0.2

4.3.3   Inducing Anesthesia

Eight meters of 4-mm ID x 6-mm OD clear polymer tubing carried the heated water from the heated water reservoir to the platform and back to the reservoir (4 meter length for each direction). Some heat was lost as the water traveled through the tubing; thus, it was necessary to maintain the water in the reservoir at 40 °C to maintain a desired temperature of 35 °C on the top of the heated base plate. The length, wall thickness, diameter, and material composition of the tubing could affect the amount of heat loss, so future systems with different lengths and types of tubing may require a higher or lower reservoir temperature.

The large decrease in mean temperature recorded for Position 5 was independent of the direction of water flow. Thus, the decrease was most likely not related to the loss of temperature over the distance of the serpentine water channel in the plate. The silicone coating was thicker over the far end of the plate that included Position 5. This rubberlike, waterproof coating could serve as an insulator and is the most likely explanation for the lower temperature in this area. This temperature inhomogeneity did not affect the ability of the plate to warm a mouse because only the mouse's tail rests over Position 5.

Anesthesia was induced using 3% isoflurane in an induction chamber connected to a SomnoSuite IDV gas anesthesia system [124]. A mouse was considered anesthetized after it ceased attempting a righting response when turned on its back in the chamber. At this point the mouse was quickly transferred to the nose cone of the support system and isoflurane anesthesia was maintained at 1.5% for surgery and 1% - 1.5% for imaging (n>40). We were able to keep the mouse fully anesthetized for over 2 hours, the average length of our imaging sessions. Routine toe pinches every 15 minutes were performed to ensure that mice were anesthetized. Furthermore, by using the shroud over the nose cone

and the activated charcoal scavenging system built into the SomnoSuite® system, we noticed that the smell of isoflurane was absent or greatly diminished when the shroud was in place. The reduced odor is consistent with a recent report that predicts a much lower level of isoflurane gas escaping into the room [124].

4.3.4   Fitting the Platform into a Small Space

The TRIO platform fit under the relatively narrow space of 35 mm between our microscope objective lens and stage. Although the overall height of our system is 2.7 cm (Fig 8) from the bottom of the base plate to the top of the head plate holders, the top of the head plate is held at 2 cm. Thus, the platform can be used in an imaging space only ~2.2 cm high, which means that it can be used on more microscope systems without replacing the microscope stage. In contrast, the Mouse and Neonatal Rat Adaptor (Stoelting Co.) was too tall to fit under the microscope objective (**Figure 38**). The distance from the objective to the top of the mouse head was about 75 mm, which would require removal or modification of the microscope stage. Similarly, a mouse placed on an electrically heated pad (RightTemp™ warming pad, Kent Scientific Corp.) or on a thermal pad (39DP Deltaphase Isothermal Pad, Braintree Scientific, Inc.) had a combined height that exceeded 35 mm. An alternative would have been to place the mouse under the objective lens on a thin, electrically heated plate (TCAT-2LV, Physitemp Instruments Inc.). However, the plate was wide and long and there was no good way to mount the head plate holder and a nose cone onto it in a secure manner.
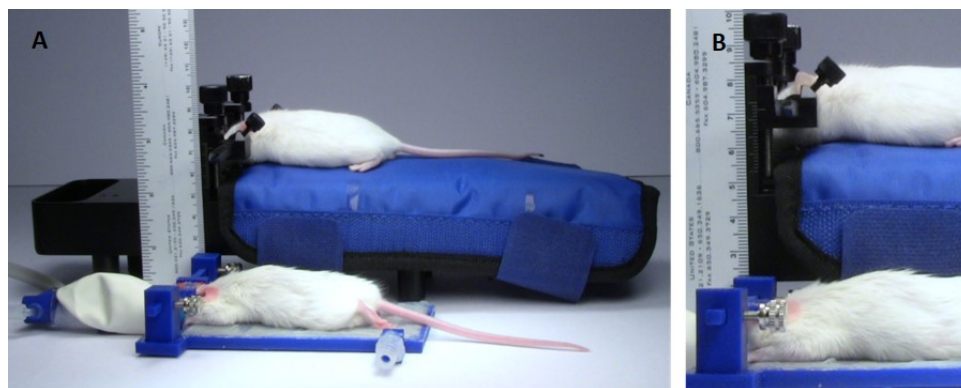
Figure 38. Height comparison. Comparison of the size of the TRIO platform with a Mouse and Neonatal Rat Adaptor with an electrically heated warming pad. (**A**) Anesthetized mice restrained in the two systems. The TRIO system is capable of warming the entire mouse, but is still much smaller than the Mouse and Neonatal Rat Adaptor. (**B**) Close-up image of the two restraint systems. The top of the mouse head in the TRIO system is 2.2 cm above the table compared to 7.0 cm in the other system [15].

4.3.5   Suitability for *In Vivo* Microscopy

The support system has allowed us to image successfully multiple mice implanted with GRIN lenses over several weeks for a total of over forty imaging sessions. The head plate and holder system held the head securely so that we observed little or no evidence of motion artifacts in our images. We also did not experience problems with misalignment of the lens with the laser beam.

Figure 39 is a representative set images of astrocytes in a 50 μm thick region of brain in a live GFAP-GFP mouse. The image set was taken through a 1.1 mm long, 350 μm diameter GRIN lens implanted into the prefrontal cortex. Cell bodies and processes can be seen at all levels through the 50 μm z-stack with some depths having more cell bodies that others. This type of imaging can virtually section the brain at varying depths and it can be repeated over time in the same animal. **Figure 310** is a two-channel image showing blood vessels and GFP+ glial cells wrapped around a blood vessel.

Figure 39. *In vivo* image set of astrocytes in lower levels of cortex viewed through an implanted GRIN lens. A z-stack of 51 images spaced 1 μm apart in depth was acquired through a GRIN lens implanted in an adult GFAP-GFP mouse. Astrocyte cell bodies and processes were observed throughout the volume. Z-projections were made of several consecutive image planes (steps). All images were projections of 5 consecutive image planes with the exception of Image E in which 10 planes were used for the projection. The most dorsal image plane was defined as plane 1 and the most ventral image was plane 51. Z-projection planes for A-H were, as follows: A. 1-5, B. 5-10, C. 10-15, D. 15-20, E. 25-35, F. 35-40, G. 40-45, H. 45-50. A Gaussian filter with σ=1.33 was applied to all channels to reduce background noise. **Scale bar = 5 μm** [15].

Figure 310. Two-channel *in vivo* image obtained through an implanted GRIN lens. The image is from prefrontal cortex of an adult GFAP-GFP mouse implanted with a 350 μm

diameter GRIN lens. Texas red-dextran dye was injected into the tail vein to visualize the vasculature. A few glial cells expressing GFP under the GFAP promoter can be seen near one of the blood vessels near the center of the image. A Gaussian filter with σ=1.33 was applied to all channels to reduce background noise. **Scale bar = 5 μm** [15].

4.3.6   Summary of Results

We have developed a low profile, multifunctional, *in vivo* brain imaging support system capable of positioning a mouse in precise alignment with an upright microscope, while simultaneously providing heat and anesthesia. The system is easily assembled and has a small footprint.

4.4   Discussion

4.4.1   Advantages of 3D Printing

The use of 3D printing is a relatively inexpensive manufacturing process in both time and material costs. The method is also flexible; typically one need only make a dimensional change in a design program, such as SolidWorks®, to modify the prototype for supporting a rat or other laboratory animal. The head plate can be redesigned and repurposed if the region of interest is along the spine.

4.4.2   Future Construction and Designs

In a few instances, a mouse's head plate became entangled in the overhanging bars that form the food hoppers in its cage. This resulted in head plates being dislodged. We now use a cage system without low overhanging bars to avoid this problem. Future head plate modifications will include reducing the size of the head plates so that they do not become caught between cage bars.

We have also determined, through measuring the mean temperatures of the base plate surface across the length of the plate that the silicone adhesive applied to seal the

heated plate also acts as an insulator when applied in a sufficiently thick layer. The area

with a relatively thick layer of silicone had a consistently lower temperature that was not

dependent on the directions of warm water flow through the plate. This was not a

problem for warming our mice because only the tail rested on this area. For future

systems, a method to apply a uniformly thin coating of silicone (< 1mm) should be

developed. Alternatively, the top plate might be effectively fused to the bottom section of

the base plate using heat, as mentioned above.

4.4.3   Potential Impact

Currently, a variety of different components are combined to create a support

system for *in vivo* optical imaging of anesthetized mice. Many of these systems include

custom made components. Furthermore, some systems include custom stages that may be

necessitated by the relatively large size of some components. Taken together, these

conditions can make it difficult for other researchers to replicate these systems and make

use of techniques that others have developed. We have combined the functions of head

restraint, alignment, warming and anesthesia into one low-profile, compact system.

Because the system is small, it should work on a wider range of confocal and multiphoton

microscope systems than other larger systems. We hope that this system or one similar to

it will provide a more standardized means of conducting these types of imaging

experiments and thus, enhance repeatability. Moreover, we hope that this system will

enable more labs to conduct *in vivo* optical imaging experiments.

CHAPTER 5

CHAPTER 6

IN VIVO IMAGING DEVICE FOR MCAO

AND THERAPY DEVELOPMENT

6.1   Ischemia/Reperfusion

Following ischemia, a decrease in oxygen causes a depression in cell signaling. The sodium-potassium channels are damaged, allowing the influx of calcium ions. As a result, an increase of glutamate is released, leading to excitotoxicity. As the neurons depolarize, more calcium enters the cells, releasing more glutamate and thus, magnifying the initial injury. Additionally, approximately 4-6 hours following injury, the blood brain barrier breaks down, directly affecting the brain vasculature. As a result of the neuronal and vasculature damage, genes become activated leading to the release of cytokines, activating microglia, and increasing inflammation [125].

Once the neurons become damaged, they display proteins, labeling them for destruction. The proteins attract de-ramified microglia, which in turn phagocytose the affected neurons [125], leading to a loss in the parenchyma volume that subsequently leads to neuronal deficits. While the microglia are important for neuronal pruning in growth and for clearing dead cells in the necrotic region after a stroke, they can phagocytose damaged, but viable neurons following injury. As a result, it may be beneficial to prevent microglia from phagocytosing cellular material in the early stages of

ischemia [126]. In order to effectively find treatments, the role of microglia following injury needs to be better defined.

Microglia have been shown to become activated beginning at 6 hours post reperfusion and become fully activated with an amoeboid shape peaking at approximately 72 hours post reperfusion [45]. The change to an activated state causes the microglia to retract their processes, increasing their cell soma area. This mechanism allows them to become mobile and phagocytose damaged material, including other brain tissue and vasculature [127]. Research has suggested microglia contribute to the breakdown of the blood brain barrier following ischemia [128], [129]. Cross staining has shown the presence of blood vessel material in the intracellular region of microglia as well as microglia enwrapping the blood vessels [66].

To further demonstrate the role of microglia in ischemia, studies conducted on mice devoid of microglia showed beneficial outcomes following reperfusion [130], [131]. The volume of damage was less significant and blood flow was more prominent in the penumbra. This data suggests a decrease in the activation of microglia may be therapeutically beneficial. While evidence has indicated that down regulation of microglia is beneficial, if the area is completely devoid of these cells, other damage may occur. Microglia are needed for daily housekeeping in the brain. Taken together, a balance of microglia activation may be needed to optimize therapeutic benefits.

When stroke occurs chemokines and cellular adhesion molecules (CAM) are expressed. As a result, leukocytes to migrate into the damaged tissue. Additionally, resident microglia become activated, leading to excessive inflammation. The inflammation causes endogenous strategies involving the glucocorticoid regulated

protein, annexin A1 (AnxA1) to be initiated by the immune cells. AnxA1 modulates the inflammatory response by targeting the formyl peptide receptor 2 (FPR2); this was demonstrated by the administration of a known antagonist, Boc2. When Boc2 is administered simultaneously with AnxA1, the anti-inflammatory properties of AnxA1 were negated [98]. When exogenous AnxA1 was administered to animals undergoing ischemia/reperfusion injury, leukocyte adhesion and rolling was significantly decreased, reducing the inflammatory response normally seen in this disease model [96], [100].

AnxA1 is endogenously expressed in microglia and it has been demonstrated, *in vitro,* that exogenous AnxA1 controls the phagocytosis of apoptotic neurons and promotes the resolution of inflammatory microglial activation. This demonstrations that AnxA1 has a fundamental role in brain homeostasis and the administration of exogenous AnxA1 may be potentially affective as a therapeutic for neuroinflammation [101] .

To date, only one clinically relevant therapeutic exists for stroke, and it is only beneficial in about 5% of stroke cases [10]. Therefore, the pursuit of new therapeutics remains a priority. Previous research has shown that exogenous AnxA1 was beneficial in animal models of post-ischemia/reperfusion [96], [98], [100], and that it had a protective effect against inflammatory microglia *in vitro* [101]. To build upon these preliminary findings and determine the effect of AnxA1 *in* the subcortical regions of the brain*,* mice with fluorescently labeled microglia were given AnxA1 at 6 and 18 hours post reperfusion and microglia dynamics were measured *in vivo* through implantable micro-lenses and multiphoton microscopy.

6.2   **Materials and Methods**

6.2.1   Lens Implantation

Mice were briefly anesthetized with 5% isoflurane and subsequently given an intraperitoneal injection of ketamine/xylazine cocktail (10 mg/kg ketamine and 1 mg/kg xylazine in 0.9% sterile saline) and transferred to a stereotaxic frame (Stoelting Co., Wood Dale, Illinois, USA), equipped with ear bars and a nose cone for isoflurane delivery (Leica Biosystems. Inc., Buffalo Grove, Illinois, USA). A SomnoSuite® system (Kent Scientific, Torrington, Connecticut, USA) was used to control isoflurane delivery. Throughout surgery, anesthesia was maintained with 1.0%-1.5% isoflurane. To ensure the animal was fully anesthetized, toe pinches were performed every 15 minutes. Aseptic surgical techniques were used to create a midline incision and remove the periosteum with a surgical bone scraper. A micro drill with a 0.5 mm dental burr was used to make a 1 mm craniectomy in the right hemisphere of the cortex and the dura was removed with the tip of a 28 G hypodermic needle at a low angle to the dura[14], [15]. Each lens implant consisted of a 500 μm diameter, 1.7 mm long, just under ½ pitch, ILH, uncoated GRIN lens (Go!Foton, Somerset, New Jersey, USA) affixed to a #1.5 glass 3 mm diameter cover slip (Electron Microscopy Sciences, Hatfield, Pennsylvania, USA) using NOA 71 optical adhesive (Norland Products, Inc., Cranbury, New Jersey, USA), as previously described. [14], [78] The cover slip facilitates lens handling and serves to correct for some of the spherical aberration inherent in GRIN lenses [78]. A small stainless steel washer, 1 mm thick, was permanently affixed to the cover slip. The washer was mounted in a cannula holder for stereotaxic insertion of the lens. The cannula holder was angled 15° toward the midline and the lens was implanted 0.9 mm rostral to bregma, 2.25 mm lateral to the midline, and lowered to a depth of 1.3 mm at a rate of 0.1 mm/min into the cortical penumbra region. The implant was secured to the skull with dental

adhesive (RelyX, 3M Corp) which was allowed to set for 15 minutes before the cannula

insertion tool was disconnected. This procedure immobilized the lens and sealed the

craniectomy. After removing the insertion tool, a rigid plastic head plate was aligned to

the washer and attached with cyanoacrylate (Krazy Glue®). The head plate was custom

designed and 3D printed in-house for use with our TRIO platform imaging support

system, which is also 3D printed in-house [15]. Mice were returned to their cages with a

warm heating pad (Braintree Scientific, Inc., Braintree, Massachusetts, USA) and were

monitored until they maintained an upright posture. To minimize post-surgical pain, an

analgesic was dissolved in the animal's water (Children's Ibuprophen, 30 mg/kg/day in 8

oz of water) for 72 hours following the procedure. Mice were allowed to recover at least

three weeks before imaging [14].

6.2.2   *In Vivo* Imaging

Mice were briefly anesthetized with 5% isoflurane and then transferred to a TRIO

platform imaging support system, as previously described [15]. Anesthesia was

maintained throughout the imaging session with 1.5% isoflurane. A Chameleon Vision-2

multiphoton laser (80 MHz, Coherent) tuned to 1020 nm was used to excite tdTomato

fluorescence. Emitted light was filtered through a 612/69 nm bandpass filter (Brightline®

filters, Semrock, Inc). Scanned images were acquired on a custom, upright, multiphoton

microscope system, equipped with a Pockels cell and GaAsP detectors (Intelligent

Imaging Innovations, Inc., Denver, Colorado, USA), a 40x/0.6 NA objective with a

correction collar for up to 2 mm of glass (Nikon Instruments, Inc., Japan) [78] and

Slidebook 6 software (3i, Inc.). A pixel dwell time of 2 μs was used with pixel averaging

(5/scan) to acquire three-dimensional (z-stack) images composed of 61 images with a

1 μm step size. Baseline images were acquired at least three weeks after lens

implantation and one week prior to the MCAo procedure. Post-treatment images were

acquired 20 – 24 hr after the procedure. Image sets were exported and stored as TIFF

files on an external hard drive for offline analysis.

6.2.3   Middle Cerebral Artery Occlusion

Mice underwent sham (n = 1) or transient (60 minute) middle cerebral artery

occlusion (MCAo) (n = 8) induced by the occlusion of the right middle cerebral artery

using an intraluminal filament method, as previously described [96]. MCAo was

conducted by Dr. Felicity Gavin's lab at LSUHSC.

6.2.4   Annexin A1 Treatment Protocols

Animals were randomly assigned to a treatment group and were given either

saline (n=2), AnxA1 (n=4), or AnxA1 + Boc2 (antagonist) (n=2) intravenously.

Treatment was administered by Dr. Felicity Gavin's Lab at LSUHSC-Shreveport, and

mice were transferred to Louisiana Tech University for imaging.

6.2.5   Perfusion and Fixation of Brain Tissue

Within 1 – 3 hr of post-procedure imaging, mice were deeply anesthetized with an

intraperitoneal injection of a ketamine (10 mg/kg)/xylazine (1 mg/kg) solution. After

deep anesthesia was confirmed with noxious toe pinches, mice were transcardially

perfused first with phosphate buffered saline (PBS) until blood was cleared and then with

20 ml of cold (4 °C), 4% paraformaldehyde solution, 7.2 pH (PFA) [14]. Heads were

decapitated and then post-fixed in PFA overnight. Next, lenses were removed from the

brain and then brains were removed from the skull [14]. After removal, brains were

immersed in PBS with 30% sucrose in preparation for cryosectioning.

6.2.6   Sectioning and Mounting

Whole brains were transferred to our collaborator, Dr. Xiao Hong Lu, at LSUHSC-Shreveport for sectioning. Once sectioned, slices were returned to our lab for mounting, imaging and image analysis. The slices were mounted onto slides for imaging by Benjamin S. Kemp and Kayla Ponder in Dr. Teresa Murray's lab at Louisiana Tech University.

6.2.7   Slice Imaging

Mounted tissue slices were imaged by Benjamin S. Kemp and Kayla Ponder. Scanned images were acquired using the same MPM system as described in **Section 4.2.2**. A pixel dwell time of 2 μs was used with pixel averaging (5/scan) to acquire three dimensional (z-stack) images composed of 31 images with a 1 μm step size. Three brain slices for each animal were imaged in order to obtain averaged results. Six regions of the brain slice were imaged in order to determine if the effects of MCAo and AnxA1 treatment differed with location. The positions included: A) CA3 in the hippocampus, B) the cerebral cortex directly above CA3, C) the necrotic core of the ischemic region, D) the transition zone, directly above position C on the ventral side of the corpus callosum, E) penumbra of the stroke, and F) the rostral cortex (**Figure 41**).
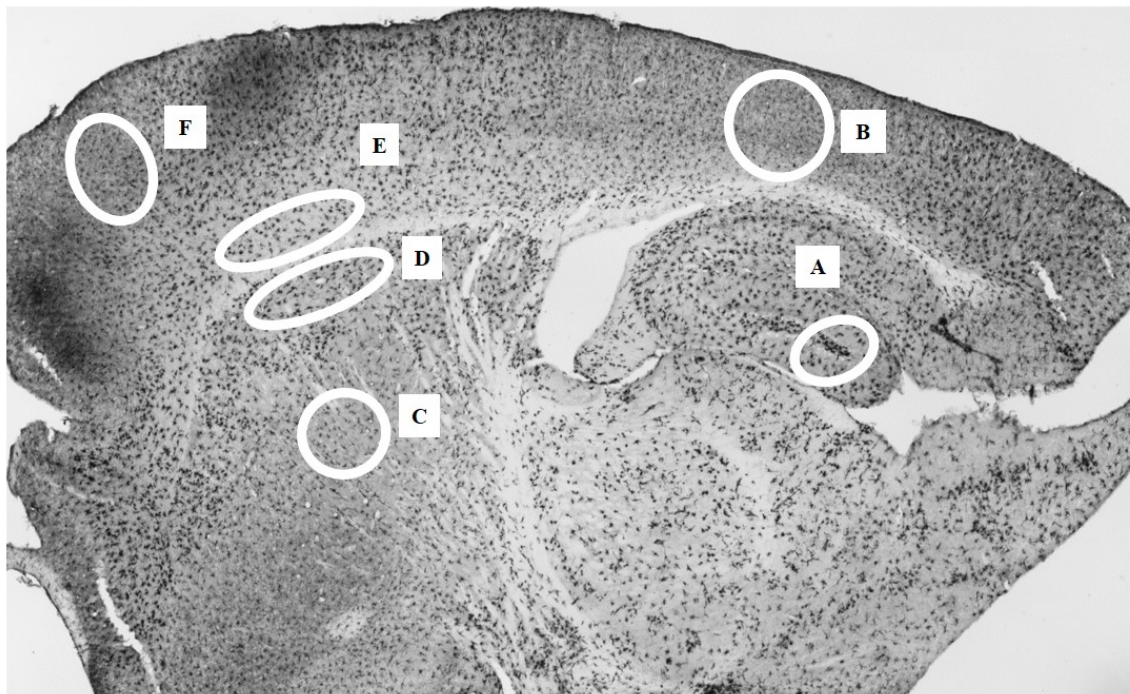
Figure 41. Nissl stained sagittal section (image, exclusive of locations for analyzing microglia activation levels, courtesy of Dr. Xiao Hong Lu, Louisiana State University Health Sciences Center, Shreveport, LA). Locations for analysis of microglia activation state in brain slice images were, as follows (**A**) CA3 in the hippocampus, (**B**) the cerebral cortex directly above CA3, (**C**) the necrotic core of the ischemic region, (**D**) the transition zone, directly above position C on the ventral side of the corpus callosum, (**E**) penumbra of the stroke, and (**F**) the rostral cortex.

6.2.8   *In Vivo* Image Analysis

Image analysis was performed by persons blinded to the treatment condition.

ImageJ (version 1.51i) [132] was used to identify and calculate the soma area of each

fluorescently labeled microglial cell. The region of interest tool was used to draw and

record the outline of each soma. The largest area of each soma was located by evaluating

each image plane in the z-stack. The threshold tool was used to subtract the background

fluorescence in this selected plane and to assist in identification of microglial processes

[133]. The measurement tool was used to create a spreadsheet of the area of each soma.

The mean value and standard error of the mean of the soma area were calculated for each

mouse for pre- and post-treatment conditions. Data were normalized to the baseline

values.

6.2.9   Brain Slice Image Analysis

Image analysis was performed by persons blinded to the treatment condition.

ImageJ (version 1.51i) [132] was used to identify and calculate the area of each

fluorescently labeled microglia cell. Max intensity z- projections of 31 x 1 μm were

created for each animal. Brightness and contrast were adjusted to visualize individual

cells. The region of interest tool was used to draw and record the outline of each soma

and draw a line across the longest part of the cell body to serve as the cell diameter. The

Sholl's analysis plugin [134] was used to determine additional properties indicating

microglia activation state. Shells were defined with a starting radius of 10 μm, and the

ending radius of the cell was determined by the user. The radius step size for the

concentric circles was 5 μm. The number of primary branches was manually entered for

each shell and linear profile with a best fit profile was used. The results were exported as

an Excel file (Microsoft Corp.) and the average results for soma area and the ramification

index for each animal were tabulated and used for comparison.

6.3   Results

6.3.1   Properties of Annexin A1

Animals underwent MCAo or sham surgery and received either saline, AnxA1, or

AnxA1 + Boc2 (antagonist). Images were acquired before and 24 hours after MCAo in

the subcortical regions of the brain and normalized cell soma area was compared (**Figure

42**). Because the number of animals was low, no statistical difference was found as

compared to the control animal, although based on the results, it appears AnxA1

treatment may exhibit protective properties post-I/R (**Figure 43**). I/R-AnxA1 normalized

average cell soma area was consistent with the normalized sham-vehicle treated animal

$(1.07 \pm 0.07$ versus 1.09). I/R-AnxA1 + Boc2 and I/R- AnxA1 had comparable

normalized results, 1.08 ± 0.01 and 1.07 ± 0.07, respectively, suggesting that the

FPR2/ALX mechanism may not be involved in modulating microglia activation post-I/R

in subcortical regions of the brain.

Figure 42. Representative images at baseline and 24 hours after sham or transient (60 min) MCAo procedure. Insets are single cells showing activation states. Microglia become activated (retracted processes) **(B)** as compared to both baseline **(A, C)** and sham treated animal **(D)**. Insets are representative images of microglia morphology. Images are z-projections of 10 x 1 µm slices. **Scale bar = 10 µm.**
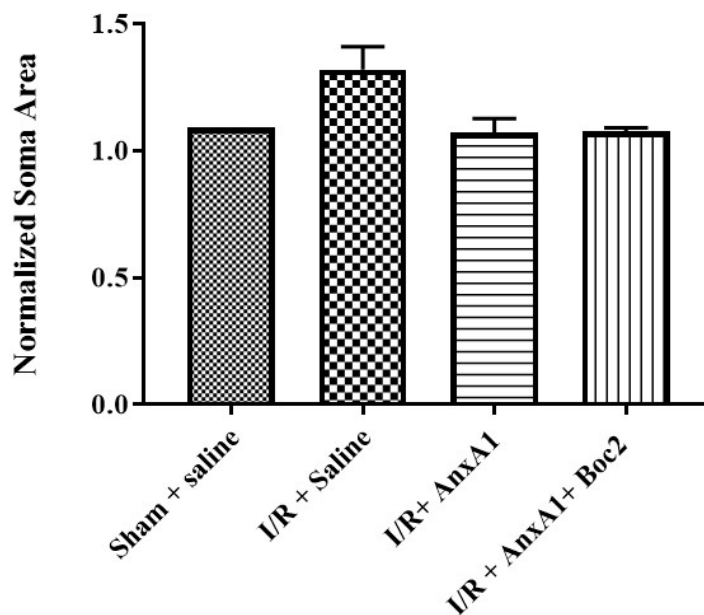
Figure 43. AnxA1 may be protective against microglial activation, but not through FPR2/ALX mechanism. Mice underwent sham (n=1) or transient (60 min) MCAo (n = 8) and administered saline (n=2), AnxA1 (n=3) or AnxA1 + Boc 2 (n=2). Cell soma area was calculated at baseline and at 24 hours post reperfusion. Data is represented as mean normalized soma area ± SEM.

6.3.2   AnxA1 in the Cortex and Necrotic Core

Post-mortem brain slice analysis was conducted to determine if AnxA1 exhibited

protective effects throughout the brain and was not limited to the area under the lens.

Brain slices were imaged and cell soma area was averaged for each animal and compared

to determine the extent AnxA1 modulates inflammation in each position (**Figure 44**).

While the number of animals was not sufficient to determine statistical significance and

to draw conclusions, it appears AnxA1 may be protective in the cortex (**Figure 45**).

Larger soma areas, a property of microglia activation, were measured in the saline treated

group as compared to the AnxA1 treated animals. Furthermore, Boc2, the antagonist, was

not effective as this time point.
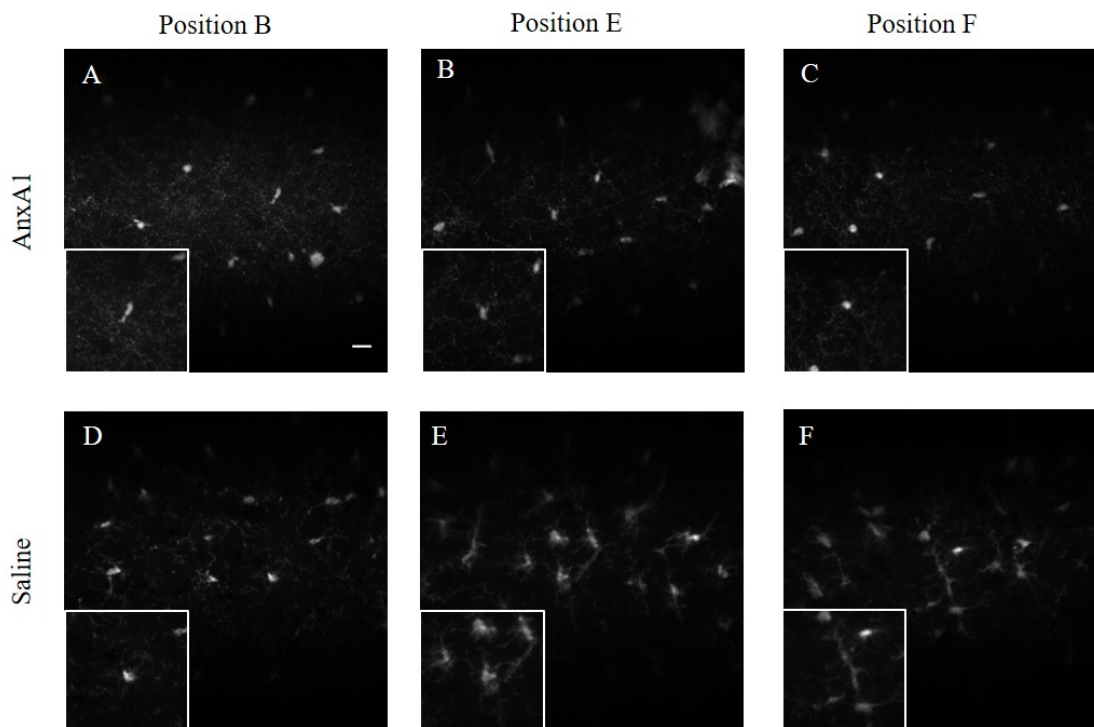
	Position B	Position E	Position F
AnxA1	A	B	C
Saline	D	E	F

Figure 44. Representative brain slice images of positions B, E, and F comparing microglia activation when treated with AnxA1 **(A-C)** versus treated with saline **(D-F).** AnxA1 treated animals had microglia with smaller soma areas in the cortex after MCAo. **Insets** are representative, enlarged images of microglia morphology. **Scale bar = 15 μm.**
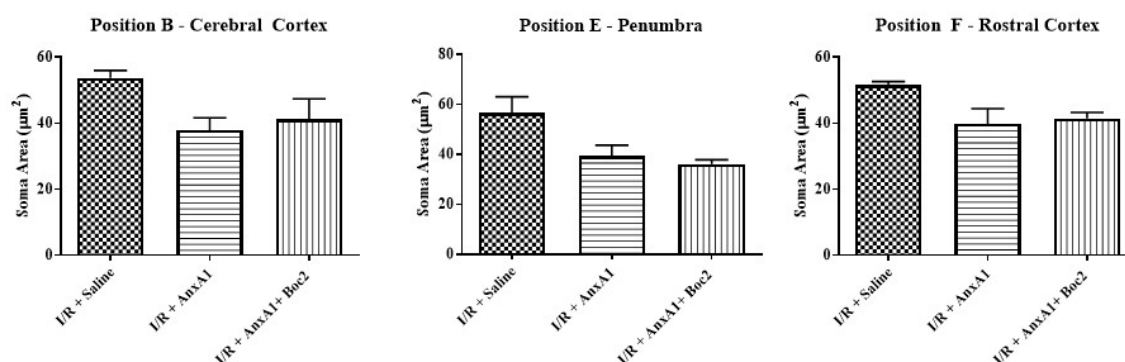
Figure 45. AnxA1 potentially has protective effects in the cortex. At 24 hours post I/R, AnxA1 treated mice tended to demonstrate modulated inflammation, indicative by smaller soma areas as compared to saline treated animals, but not through the FPR2/ALX mechanism as the antagonist, Boc2, did not appear to be effective.

While Annexin A1 exhibited protective effects in the cortex, it did not appear to be as affective in the hippocampus, as cell soma areas in the treated groups were comparable to the saline treated animals. Furthermore, when the antagonist was administered, it was not affective at this time point. (**Figure 46**, **Figure 47**).
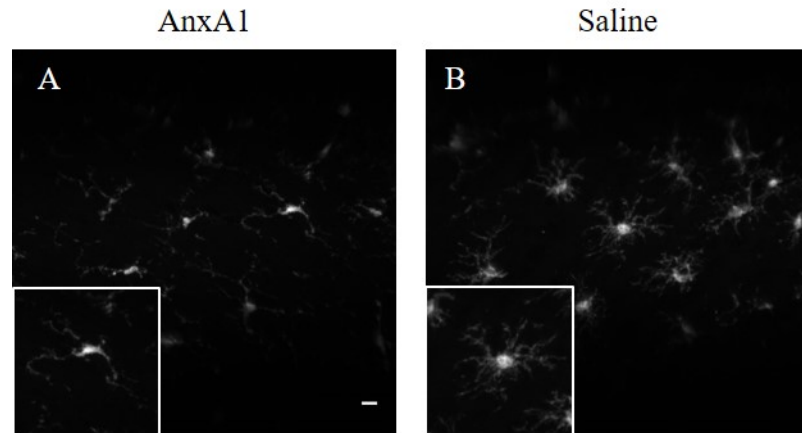
Figure 46. Representative brain slice images from position A (hippocampus) comparing microglia activation when treated with AnxA1 **(A)** versus treated with saline **(B)**.**Insets** are representative up close images of microglia morphology. **Scale bar = 15 μm.**
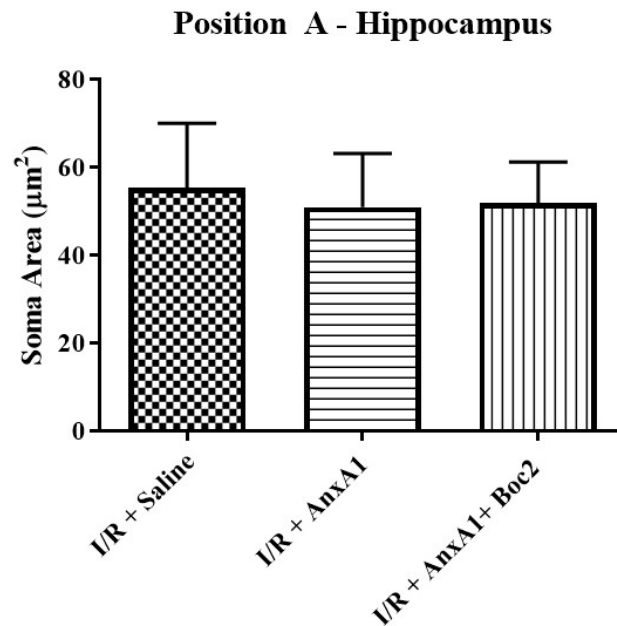
Figure 47. AnxA1 does not exhibit protective properties in the hippocampal region. Saline and AnxA1 treated animals exhibited comparable cell soma areas.

Interestingly, AnxA1 modulated inflammation, as shown by smaller cell soma areas, in the ischemic core (Position C) and the transition zone (Position D), regions containing irreversible damage and widespread cell death (**Figure 48**, **Figure 4-9**). Consistent with other regions, the antagonist was not affective at this time point.
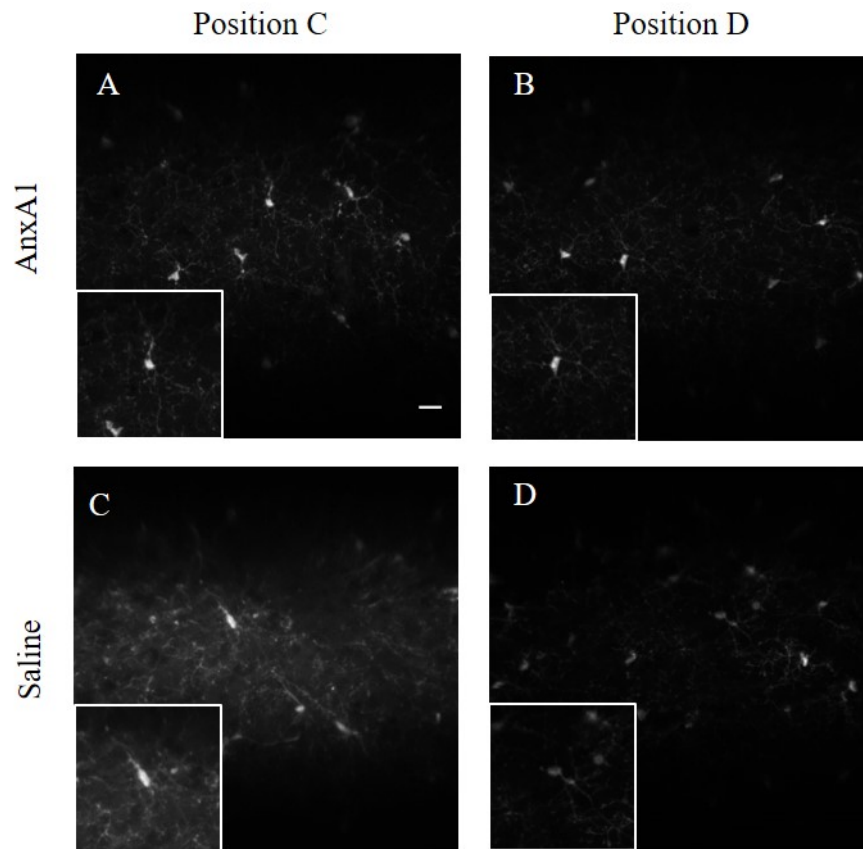
Figure 48. Representative brain slice images of position C (**A, C**) and position D (**B, D**), the necrotic core and transition zone, respectively. Cell soma areas in the AnxA1 treated animals exhibited cells with resting morphology. **Insets** are representative images of microglia morphology. **Scale bar = 15 μm.**
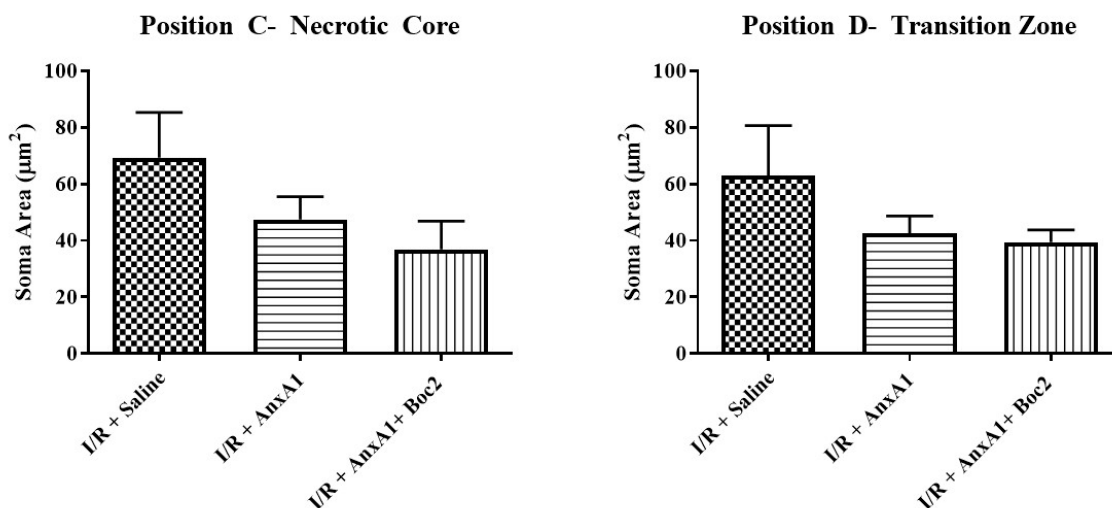
Figure 49. AnxA1 modulates microglial activation in the ischemic core (position C) and transition zone (position D). Treated animals exhibited smaller soma areas in both positions. The antagonist, Boc2, was not effective in these regions and time point.

6.3.3   Imaging System for MCAo

While the study conducted did not lead to statistically significant conclusions concerning the use of AnxA1 as a therapeutic, it did demonstrate the exciting potential to use GRIN lens imaging as a tool to identify microglial activation, a hallmark of neuroinflammation, post-MCAo and to evaluate potential therapeutics in an *in vivo* model. The imaging device was implanted to collect images in subcortical regions of the mouse and the normalized data gave comparable results to position E, the penumbra (Figure 4-1). The nature of the methodology allowed each animal to act as its own control, reducing the number of animals needed for the study. Baseline, three dimensional images were acquired prior to MCAo for each mouse and the data were normalized to post injury results, reducing the inter-animal variability seen in traditional histological analyses.

6.4   Discussion

With stroke being a prevalent problem with minimal existing interventions, it is imperative we find new therapies. Annexin A1 has previously been shown to modulate the inflammatory response in ischemia/reperfusion by reducing the number of rolling and adherent leukocytes through the FPR2/ALX mechanism of action [98]. While the number of animals in this preliminary study was too small for statistical inference, the *in vivo* data suggest that Annexin A1 has the potential to modulate microglia activation post-reperfusion in the penumbra region of the brain. However, it does not appear that the modulation is acting through the FPR2/ALX mechanism. Histological examination of the brains showed Annexin A1 may be effective in protecting the cortex post I/R, but not the hippocampus. Additionally, it appeared to have an effect on the cells located in the necrotic core, an area that typically has irreversible damage. Without more mice, it is difficult to definitively say where Annexin A1 is exhibiting a protective effect and the mechanism involved.

The novel imaging method used in the study was able to collect quality images of microglia and cell soma area could be normalized to the baseline, reducing inter-animal variability. Additionally, it showed results consistent to brain slice analysis, demonstrating it as an effective tool for monitoring microglia activation in the MCAo model and assessing the effectiveness of potential therapeutics.

6.5   Future Work

To obtain more conclusive results about the effectiveness of annexin A1 as microglia modulator, more animals are needed. This study set the ground work and confirmed GRIN lenses are an effective technology for the MCAo model of ischemia/reperfusion by identifying microglial activation 24 hours post injury, and it

showed annexin A1 may be protective in the cortex and ischemic core. Now, a more in-depth study is needed to confirm the effectiveness of the endogenous drug.

A benefit of this novel imaging tool is the ability to collect longitudinal data. Imaging windows can be extended out days and even months after the initial injury and microglial dynamics can be measured over time. This imaging tool makes it possible to collect data immediately following injury and during the recovery phase to better understand not only how microglia dynamics change when therapeutics are administered, but the fate of the microglia when therapeutic administration is stopped in the same mouse. This capability not only reduces inter-animal variability but also minimizes the number of animals used. Overall, GRIN lens technology has shown exciting potential to be used as a preclinical research tool and will lead to a better understanding of brain injuries.

CHAPTER 7

CHAPTER 8

LONGITUDINAL IN VIVO IMAGING SYSTEM

FOR A MURINE MODEL OF TRAUMATIC

BRAIN INJURY

8.1   Diffuse Axonal Injury

The human brain can be described as viscoelastic, and it can tolerate the gradual accelerations associated with normal, daily living. With slowly applied forces, the brain tissue is ductile and can recover its original geometry unscathed [7]. When a force is rapidly applied (< 50 ms), the brain acts like a more brittle solid, resulting in shearing of the cell membrane and cytoskeleton, followed by a delayed elastic return to its pre-injury state. The injury is further intensified if the force applied surpasses the threshold of the axons [135]. As a result, axon damage is dependent on the rate and the magnitude of strain during a TBI.

The most common closed head injury to occur is known as diffuse axonal injury (DAI), which results in subtle, but significant widespread damage throughout the brain parenchyma and primarily affecting the corpus callosum, the communication lines between the two hemispheres of the brain. These progressive changes are a direct consequence of the primary mechanical forces at the time of injury. Characteristics of this injury were experimentally detected as early as 1943 by Holbourn et al., who used gelatin molds of brain sections and found that rotational forces caused shear and tensile strains

throughout the material [136]. Morphological alterations in white matter were histologically found in severely injured TBI patients and it was proposed that the shear strains at the moment of injury were responsible for the damage [137]. Furthermore, the axons exhibited swollen profiles in the moderate to severe range of injury [138].

While immediate disconnection of axons is seen in severe brain injury, the major damage of DAI is secondary axon disconnection which occurs over a prolonged period of time. As a result of mechanical forces, the axonal cytoskeleton breaks down, becoming twisted and misaligned, leading to secondary physiological changes such as interrupted axonal transport, periodic swellings along the axon, and in some cases neurodegeneration [135]. The injury not only causes changes on a cellular level, but also leads to a disruption in cognition and behavior, resulting in poor outcomes for the patient [39], [139]. Therefore, it is necessary to not only better understand the progression of axonal damage, but also identify potential therapeutics to mitigate secondary damage.

8.1.1   Undulations

Microtubules represent the stiffest component of the axon and are made of stable and dynamic tubulin polymers. The dynamic portions of microtubules allow a rapid change in length during axonal development and regeneration [140]. Conversely, this trait of axons may make them more susceptible to mechanical trauma seen in diffuse axonal injury.

Cultured axon models have been developed to observe the pathologies seen in *in vivo* traumatic brain injury. A threshold for primary axotomy and temporal evolution of axon response to stretch injury was investigated and it was found that primary axotomy did not occur for strains under 65% and in fact, strains of 77% did not sever all axons.

Rather, it was discovered that some axons could stretch beyond their original length, but upon relaxation would develop areas with the geometry of half circles or triangles, known as undulations. While some axons developed these undulations, other axons were able to return to their pre-stretch state, elastically recovering. The data suggest that the distortion is nonuniform following dynamic stretch injury [141].

In another *in vitro study*, axons were cultured and subjected to either a slow or rapid loading condition. Under a slow loading rate, the axons were able to easily tolerate being stretched two times their original length. However, when rapid loading conditions were applied (<50 ms), axons consistently showed undulating areas after stretch injury. After approximately 40 minutes, the axons returned to their pre-stretched state, but an accumulation of transport proteins formed into areas of swellings. The results of the study suggest mechanical failure occurs along the microtubules at the time of injury and microtubules may fail to realign, leading to a physical blockade impeding natural axon relaxation and the formation of undulations [142].

8.1.2   Axonal Varicosities

One of the identifying features of DAI are periodic axonal swellings resulting from the accumulation of axonal proteins following microtubule breakage. These swellings are known as axonal varicosities and appear along the length of a damaged axon. In an *in vitro* model, modeling the mechanical loading experienced by neurons *in vivo*, the neurofilament structure changes following a stretch injury, interrupting the transport of material to the cell soma [141]. The accumulation of proteins in these swollen areas is a key feature of damage and disruption of axonal transport.

In animal models, amyloid precursor protein (APP) is commonly used, with high sensitivity, as a biomarker for DAI. APP is one of the proteins that accumulates rapidly and causes areas of swelling within 2 hours of injury. APP was detected even 30 days following initial injury, suggesting not only axonal transport is impaired, but that this damage is long term [143]–[145].

Neurofilament is a key component of the axonal cytoskeleton. Its accumulation has also been found in areas of swelling [146], [147], demonstrating that damaged neurofilaments play a role in the development of varicosities. Neurofilament compaction, which is the reduction in the interfilament spacing caused by the breakdown of side arms, contributes to the blockade of axonal transport. *In vitro* studies have shown that, following axonal stretch injury, both microtubule and neurofilament damage correlated with undulations and within hours of the injury developed into varicosities [148].

To date, the evidence found concerning the development of varicosities has been limited to histopathological examination of post-mortem brain tissue or *in vitro* models. In order to better understand the development and fate of this post-TBI feature, longitudinal *in vivo* analysis is needed.

8.1.3   Axonal Bulbs

A widely recognized, but not necessarily more common pathology discovered after DAI is the presence of large single swellings known as axonal bulbs. Primary axotomy is rare event, but secondary axotomy, the weakening of the axons by undulations and axonal varicosities, occurs over the course of hours to days, and in some cases months following the injury [7], [36]. Not all injured axons will develop into axonal bulbs. In fact, many axons are able to become undulated, develop varicosities, recover

and return to their relaxed state. While the mechanical damage cannot be reversed, the recovery phase offers an opportunity to intervene with a therapeutic.

8.2 Minocycline as a Treatment for Traumatic Brain Injury

Minocycline has been effective when administered acutely following traumatic brain injury. It limits both early and chronic neuroinflammation and preserving the integrity of the brain [91], [92]. Additionally, the drug has shown promise in protecting long term behavioral and functional outcomes, which are negatively impacted by traumatic brain injury [93]. While minocycline cannot prevent the early effects of mechanical damage, such as the accumulation of β-APP [91], long term it protects the volume of high populated axonal areas, such as the corpus callosum, suggesting the drug is preventing axonal loss which can occur after undulations, varicosities, and terminal bulb formation.

8.3 Longitudinal Data Need

Longitudinal data are needed to better understand the time course of axonal damage after traumatic brain injury and the mechanism by which treatments, such as minocycline, intervene and protect the brain. Additionally, while minocycline was effective when administered acutely, it is not always possible to treat individuals early on following injury. Therefore, it is necessary to determine if the drug has protective effects at later time points and if the protection is comparable to early administration.

To date, evidence demonstrating the progression of axonal damage following traumatic brain injury has been limited to histology, *in vitro,* and *in silico* models. While these methods have added a plethora of knowledge about defining features of diffuse axonal injury, how these features progress *in vivo* is still unknown. Thus, to better

understand the progression from the time of injury to the formation of a terminal bulb, being able to track the same injured axon longitudinally is imperative. Fortunately, the technology exists to visualize the time course of DAI. Gradient refractive index (GRIN) lenses offer an opportunity to collect longitudinal data with high cellular resolution. In addition to understanding the progression of DAI, it is also important to understand how potential therapeutics for DAI are affecting axon degeneration. Minocycline was protective against white matter degeneration and microglia activation following traumatic brain injury when acutely administered [91], [94], [131], [149].

To further facilitate these investigations, the current study uses a novel imaging method in which Thy1-YFP mice are imaged in a longitudinal manner, before and periodically over the course of 30 days following fluid percussion injury (FPI) in mice. FPI is a model of diffuse brain injury. To demonstrate the utility of this novel imaging method for preclinical trials, minocycline was administered at a known therapeutic window commencing at 45 minutes post injury [89]. Additionally, minocycline was administered to a group of mice commencing at 72 hours post-FPI to determine its therapeutic potential in a wider treatment window. As a result, progressive axonal damage and the effect of the potential therapeutic was successfully identified.

GRIN lenses were implanted just above the external capsule in Thy1-YFP transgenic mice (**Figure 5-1**). Thy1-YFP mice express yellow fluorescent protein in motor and sensory neurons that is a strong marker for axons. Following at least three weeks after GRIN lens implantation, multiphoton microscopy is used to collect baseline images for each mouse in the study. Once a baseline image is collected, FPI is used to

induce diffuse brain injury. Images were taken at 1 hour, 3 days, 7 days, 14 days, 30 day, and 60 days following injury in order to evaluate progressive axonal damage.
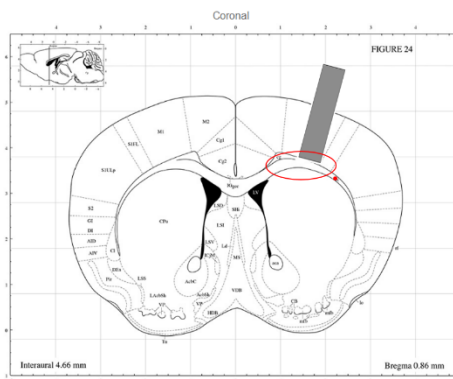
Figure 51. A GRIN lens (**gray rectangle**) is implanted just above the external capsule (**red circle**) in order to image axonal damage over time. Adapted from *Paxinos and Franklin, 2012*.

To determine if the implanted imaging device is an effective tool for preclinical trials, a clinically relevant drug was administered. Minocycline, an FDA-approved antibiotic, has mitigated some of the effects of diffuse brain injury when administered between 45 minutes and 4 hours following injury [89]. Serving as the positive control in the experiment, minocycline (45 mg/kg) was administered at 45 minutes following injury. In order to experimentally determine if minocycline had positive outcomes at a later time point, since it is not always possible to treat individuals immediately following injury, minocycline was administered at 72 hours following injury. Subsequent doses, as done in previous trials [89], were administered at 24 hours and 48 hours following the initial doses at both the 45 minute and 72 hour time point.

In order to relate structural changes to behavioral changes and further characterize the effect of the minocycline, the rotarod, neurological severity score (NSS), open field, novel object recognition, and tail suspension tests were used. The rotarod and NSS tests

were conducted within the first week (Days 2, 5, and 7) following injury to insure the animal maintained a diffuse brain injury. The open field, novel object recognition, and tail suspension test are conducted on Day 60 to test for anxiety, memory, and depression, respectively. Immediately following behavioral studies at Day 60, animals were perfused to prepare for histological analysis. A summarized timeline for the experiments can be found in **Figure 5-2**.
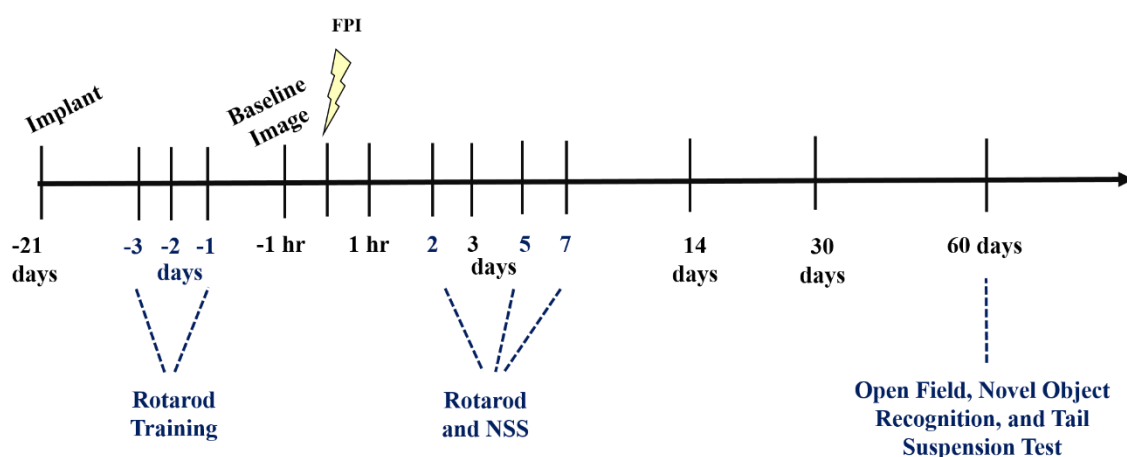
Figure 52. Experimental Timeline.

8.4 Materials and Methods

8.4.1   Lens Implantation

Mice were briefly anesthetized with 5% isoflurane and subsequently given an intraperitoneal injection of ketamine/xylazine cocktail (10 mg/kg ketamine and 1 mg/kg xylazine in 0.9% sterile saline) and transferred to a stereotaxic frame (Stoelting Co., Wood Dale, Illinois, USA), equipped with ear bars and a nose cone for isoflurane delivery (Leica Biosystems. Inc., Buffalo Grove, Illinois, USA). A SomnoSuite® system (Kent Scientific, Torrington, Connecticut, USA) was used to control isoflurane delivery. Throughout surgery, anesthesia was maintained with 1.0%-1.5% isoflurane. To ensure

the animal was fully anesthetized, toe pinches were performed every 15 minutes. Aseptic surgical techniques were used to make a midline incision, and a surgical bone scraper was used to remove the periosteum. A micro drill and 0.5 mm dental burr were used to make a 1 mm craniectomy over the right hemisphere of the cerebral cortex and the tip of a 28 G hypodermic needle was used, at a low angle to the dura, to remove the dura mater. [14], [15]. Each lens implant consisted of a 500 μm diameter, 1.7 mm long, just under ½ pitch, ILH, uncoated GRIN lens (Go!Foton, Somerset, New Jersey, USA) affixed to a 500 μm diameter, 0.6 mm long custom made glass window. NOA 71 optical adhesive (Norland Products, Inc., Cranbury, New Jersey, USA) was used to glue the window and lens to a #1.5 glass 3 mm diameter cover slip (Electron Microscopy Sciences, Hatfield, Pennsylvania, USA) as previously described [14], [78] The cover slip facilitates lens handling and serves to correct for some of the spherical aberration inherent in GRIN lenses [78]. The same adhesive was used to permanently affix a small, stainless steel washer, 1 mm thick to the cover slip (Figure 53). The washer was mounted in a cannula holder for stereotaxic insertion of the lens. The cannula holder was angled 15° toward the midline and the lens was implanted 0.9 mm rostral to bregma, 2.25 mm lateral to the midline, and lowered to a depth of 1.5 mm at a rate of 0.1 mm/min so that it was implanted just above the corpus callosum. The implant was secured to the skull with dental adhesive (RelyX, 3M Corp) which was allowed to set for 15 minutes before disconnecting the cannula insertion tool. This procedure immobilized the lens and sealed the craniectomy. Mice were returned to their cages with a warm heating pad (Braintree Scientific, Inc., Braintree, Massachusetts, USA) and were monitored until they maintained an upright posture. To minimize post-surgical pain, an analgesic was

dissolved in the animal's water (Children's Ibuprophen, 30 mg/kg/day in 8 oz of water)

for 72 hours following the procedure. Mice were allowed to recover at least three weeks

before imaging [14].
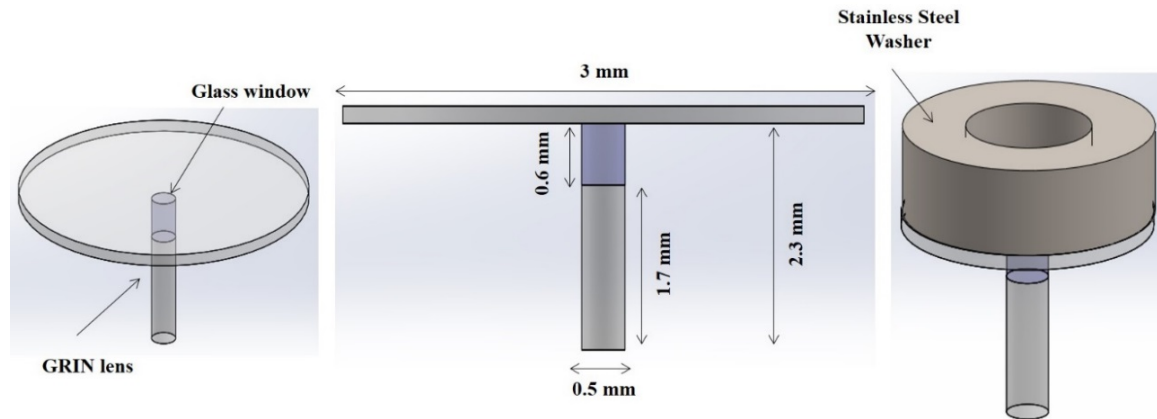
Figure 53. GRIN lens fabrication. Each implantable lens has 600 μm x 500 μm glass window and a 1.7 mm long GRIN lens glued to a #1.5 3 mm in diameter glass window. These lenses were affixed to a 1 mm thick stainless steel washer.

8.4.2   Head Plate Construction

Head plates were designed in SolidWorks software and then 3D printed in house

from PLA filament. The head plates were designed to secure the animal's head while

imaging such that the GRIN lens was normal to the laser beam. If the GRIN lens is tipped

with respect to the laser beam, the image quality degrades. The head plate is 20 mm x 11

mm x 1 mm (L x W x H) and has a cut out for the washer portion of the GRIN lens

components. (Figure 54**A**). The back end of the head plate is open to allow an injury hub,

a vital part of the fluid percussion injury system, to be attached during a second surgery

(**Figure 5-4B**).
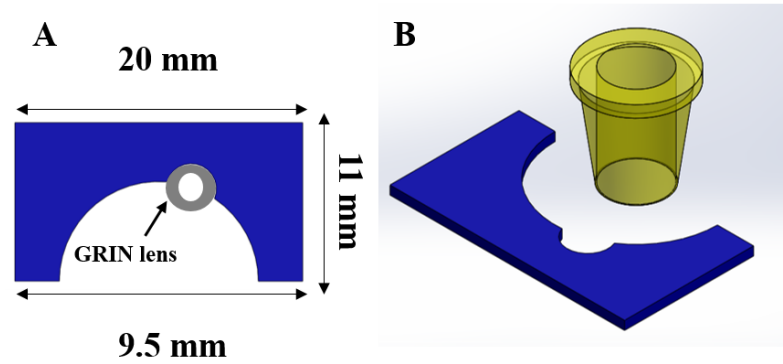
Figure 54. Head plate construction was adapted to allow access to the craniectomy **(A)** in order to attach the injury hub during the fluid percussion injury surgery **(B).**

8.4.3   Head Plate Attachment

Head plates were attached two weeks post GRIN lens implant. Gel cyanoacrylate (Loctite ®) was used to attach the head plate. The animal was briefly anesthetized with 5% isoflurane and transferred to a stereotaxic frame (Stoelting Co., Wood Dale, Illinois, USA), equipped with ear bars and nose cone for isoflurane delivery. For the duration of head plate attachment, isoflurane was maintained at 1.5%. The head plate is carefully placed so that it is lined up with the washer portion of the lens. Once it is successfully aligned, additional gel cyanoacrylate (Loctite ®) is placed around the edges of the head plate to firmly secure the head plate. The cyanoacrylate is allowed to dry for 20 minutes before the animal is returned to its cage. The head plate remains attached for the duration of the experiment.

8.4.4   Imaging

Mice were briefly anesthetized with 5% isoflurane and then transferred to a TRIO platform imaging support system, as previously described [15]. Anesthesia was maintained throughout the imaging session with 1.5% isoflurane. A Chameleon Vision-2 multiphoton laser (80 MHz, Coherent) tuned to 890 nm was used to excite YFP

fluorescence. Emitted light was filtered through a green fluorescent protein filter (Brightline® filters, Semrock, Inc). Scanned images were acquired on a custom, upright, multiphoton microscope system, equipped with a Pockels cell and GaAsP detectors (Intelligent Imaging Innovations, Inc., Denver, Colorado, USA), a 40x/0.6 NA objective with a correction collar for up to 2 mm of glass (Nikon Instruments, Inc., Japan [78] and Slidebook 6 software, 3i, Inc.). A pixel dwell time of 2 μs was used with pixel averaging (5/scan) to acquire three-dimensional (z-stack) images composed of 100 images with a 1 μm step size. Baseline images were acquired at least three weeks after lens implantation and one week prior to the fluid percussion injury procedure. Post-treatment images were acquired at 1 hour, 3, 7, 14, 30, and 60 days after the procedure. However, between Day 30 and Day 60, most of the animals lost their head plates and as a result, the image sets were not analyzed at Day 60. Image sets were exported and stored as TIFF files on an external hard drive for offline analysis.

8.4.5   Fluid Percussion Injury Surgery

To obtain images following a traumatic brain injury in mice, a second surgery was necessary. The midline fluid percussion injury (mFPI) model surgery [150] was adapted such that the procedure could be performed after successful GRIN lens implantation and baseline imaging. To perform mFPI, a craniectomy, was created with the dura intact and an injury hub was attached. The injury hub facilitates attachment of the animal to the mFPI device. Once the injury was completed, the hub was removed and the skin was sutured to cover the craniectomy. The primary change was made during the injury hub attachment step. Kwik-Sil (World Precision Instruments) was used in place of dental

cement. This step protects the GRIN lens from being removed when the injury hub was removed.

The animal was initially anesthetized with 5% isoflurane. Once the animal no longer exhibited a righting response, it was transferred to a stereotaxic frame equipped with ear bars and nose cone for anesthesia delivery. The surgical area was cleaned with 91% isopropyl and iodine. Once the area was dry, a 1 mm thick piece of weed whacker line was glued on the midline between bregma and lambda with liquid cyanoacrylate (Krazy Glue ®), which served as a guide for a trephine to create a craniectomy.

After the cyanoacrylate dried, trephining began so that a 3 mm craniectomy was created. Trephining continued until the bone flap was able to move independently of the skull. Care was taken not to cut into the dura with the trephine. If the dura was compromised, the animal was removed from the study. The bone flap was removed by pulling on the piece of weed whacker. If the weed whacker line came off prior to removal, a pair of fine forceps was used to gently remove the bone flap without piercing the dura. Once the bone flap was removed, cotton pads and sterile 0.9% saline were used to control the bleeding. The injury was then prepared.

Injury hubs were constructed using 24 G hypodermic needles. The needle hub was cut just above the second white line so that the hub opening could fit over the 3 mm diameter craniectomy. To determine if the hub opening was the proper size, the trephine was placed in the cut end of the hub to ensure a sufficient opening for the fluid used in the FPI procedure. The hub was placed over the craniectomy and secured with gel cyanoacrylate (Loctite ®). Next, Kwik-Sil, (World Precision Instruments, LLC) a biocompatible, silicone adhesive was used in place of dental cement to secure the injury

hub to the skull. The Kwik-Sil touched the head plate, but was easily removed following injury. Kwik-Sil's elastomer properties cause it to deform more than dental cement when forces are applied. Consequently, this caused inconsistent degrees of injury in animals in preliminary studies. To circumvent this challenge, once the Kwik-Sil had cured, dental cement was placed over the Kwik-Sil to prevent movement of the Kwik-Sil that could reduce the fluid pressure that reached the brain (**Figure 5-5**). The dental cement should only cover the Kwik-Sil and not run onto the head plate or the head plate could potentially be pulled off during injury hub removal. Once the dental cement was dry, the hub was filled with 0.9% saline and checked for leaks. Any leaks were sealed before terminating anesthesia. Once it was determined that there were no leaks, the animal was removed from anesthesia and transferred to a heating pad until recovered.
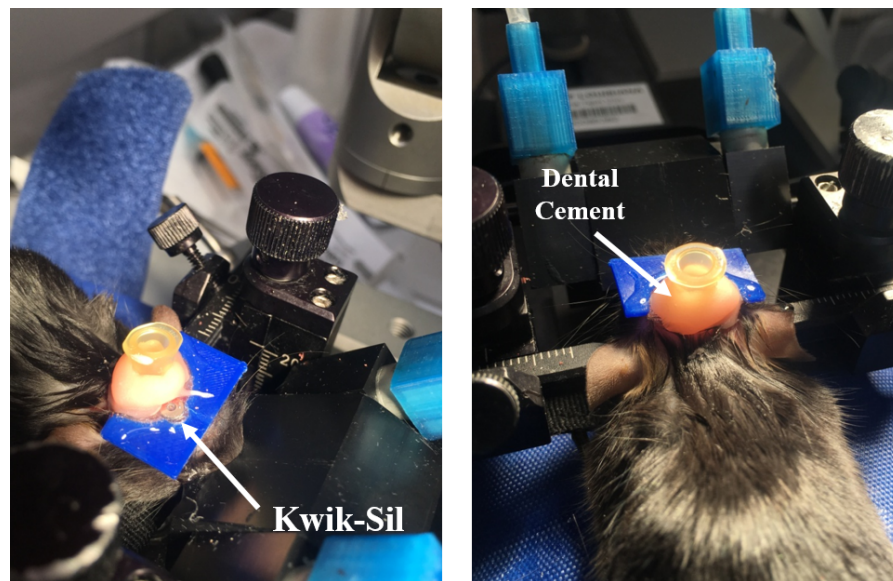
Figure 55. Injury hub attachment required the use of both Kwik-Sil, to cover and protect the GRIN lens, and dental cement, to ensure proper pressure for the FPI procedure.

8.4.6   Fluid Percussion Injury

Animals were randomly divided into either sham (n=4) or FPI (n=14). Each animal was anesthetized with 5% isoflurane for 5 minutes in an anesthesia chamber. Immediately after removal from the chamber, the injury hub was filled with 0.9% saline and connected to the fluid percussion injury device (Custom Design & Fabrication, Virginia Commonwealth University, Richmond, VA) (**Figure 56A**). The device causes injury by applying a brief fluid pressure pulse to an intact area of dura. The pulse was created by a heavy hammer (**Figure 56B**) head on a swinging pendulum (**Figure 56C**) that strikes a fluid filled cylinder (**Figure 56D**). This caused a brief compression of the brain (<20 ms). The animal was checked with toe pinches and when a response was exhibited, but before the animal had fully regained consciousness, the pendulum was released [150]. After impact, the animal was detached from the device and placed on a heating pad until the animal righted itself (Braintree Scientific, INC.). The elapsed time from injury to the righting response was recorded. For a moderate injury, a righting response between 6-10 minutes was needed. For sham injured animals, the same procedure was followed except, the pendulum was not allowed to hit the fluid filled cylinder. After the animal had righted itself and the parameters of injury were recorded, and the animal was returned to its home cage.
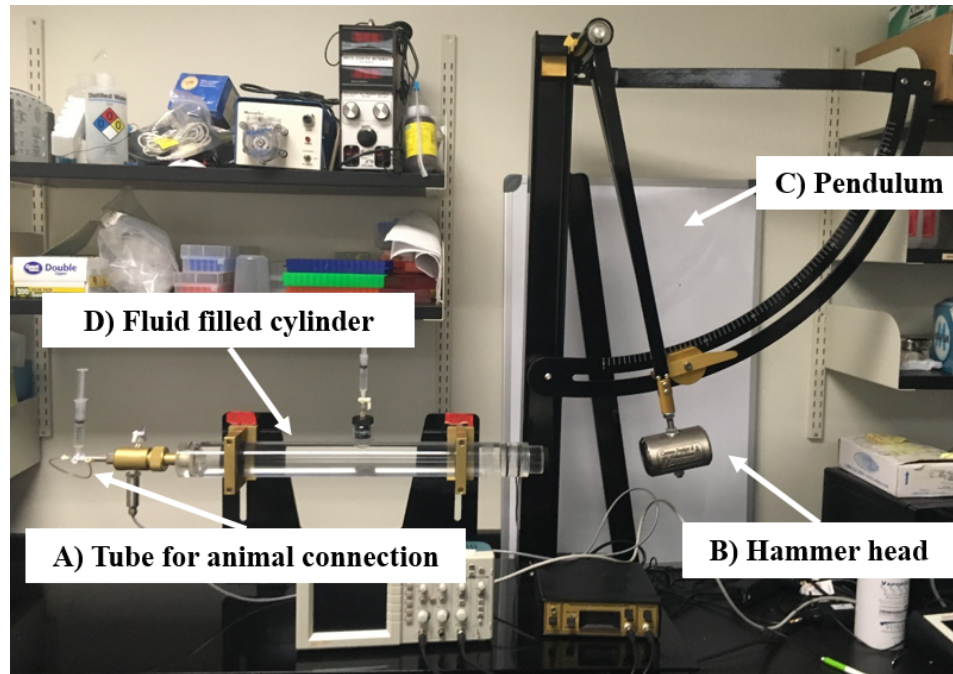
Figure 56. Fluid percussion injury device. The animal is connected to the device via tube with a leur lock ending **(A)** and a hammer head **(B)** on a pendulum **(C)** hits the fluid filled cylinder **(D)** which causes a brief pressure pulse (< 20 ms) onto the intact dura of the mouse brain.

To seal the craniectomy after injury, the animal was briefly anesthetized for five

minutes and then transferred to a frame equipped with ear bars and a nose cone.

Anesthesia was maintained at 1.5% for the duration of craniectomy sealing. Sterile saline

was used to clean the area before sealing. After the area was sterile, 1.5% low melt

agarose (IBI Scientific, Peosta, Iowa) was placed on the craniectomy followed by a #1.5

cover glass, 3 mm in diameter (Electron Microscopy Sciences, Hatfield, Pennsylvania,

USA). Once the agarose had solidified, gel control cyanoacrylate (Loctite®) was

carefully placed around the edges of the cover glass. Care was taken to not allow the

cyanoacrylate to run under the cover glass and agarose and onto the dura mater. Once the

cyanoacrylate had cured (about five minutes), Aplicap™ (RelyX ™ Unicem) was placed

on the skull, beginning on the edges of the cover glass until it had completely covered

any openings to the skull. Aplicap™ was allowed to cure for at least 20 minutes before transferring the animal to the TRIO system[15] for the one hour imaging time point.

8.4.7 Minocycline Administration

Animals were randomly divided into four groups as follows: sham injury with saline treatment (sham-vehicle), TBI with saline treatment (TBI-vehicle), TBI with minocycline treatment beginning at 45 min (TBI-45-min), and TBI with minocycline treatment commencing at 72 hr post TBI (TBI-72-hr). Minocycline (45 mg/kg) (Tocris Bioscience) or 0.9% saline was administered intraperitoneally three times for each group, the initial dose, and then another at 24 hours and 48 hours after the first dose.

8.4.8 Acute Behavioral Evaluations

To determine if acute cognitive and sensorimotor deficits are present following fluid percussion injury, the rotarod and neurological severity score (NSS) were evaluated at Days 2, 5, and 7 [151].

8.4.8.1 *Rotarod score*

The Accurotor Rotarod (AccuScan Instruments, Inc. Columbus, Ohio USA) was used to assess sensorimotor functions. Animals were acclimated to the device three days before injury (acclimation period). The animal was placed on the stationary rod and allowed to explore the rod for 30 seconds. If the animal fell off the rod before the 30 seconds, the animal was placed back on the rod. Once the animal had successfully explored the stationary rod for 30 seconds, the angular frequency of the rotarod was adjusted to a constant rate of five revolutions per minute (rpm). If the mouse fell off the rod, it was placed back on the rod and the timer restarted until it could walk for 15 seconds. After this, the rotarod speed was adjusted to an acceleration of 0.2 rpm/s. The

trial ended once the animal fell off the rod. The animal was returned to its cage for 10 minutes and the accelerating rod portion of the test was re-run. Again, once the animal fell, the animal was returned to its home cage, and the acclimation phase ended.

The testing procedure began three days before injury and was run on Days 3, 2, and 1 before injury. The procedure took place at the same time each day, between four and seven pm, to minimize any variability. The mice were placed on the apparatus and were tested for their ability to remain on the rotarod with an acceleration of 0.2 rpm/s. The apparatus is equipped with sensors to detect when the animal falls and records the time in seconds. Three trials were run on each testing day, with trial one and two run back to back and the third trial run after a 10 minute break. The two best times were averaged for the day. The average time for one day before injury was used as the baseline data point. The rotarod test was used on Days 2, 5, and 7 following FPI to detect if motor deficits were present.

8.4.8.2   *Neurological severity score*

To evaluate neurological impairment following FPI, eight behavioral tests were performed. The tests determined the function of the cortex and cerebellum, and if any additional motor deficits were present. The mice were assessed on the presence of 1) hind limb flexion, 2) seeking behavior, 3) startle response, ability to walk across 30 cm long, square cross section, beams with progressively smaller widths of (4) 3 cm, (5) 2 cm, and (6) 1 cm width, and to (7) balance on a 0.5 cm square beam and a (8) 0.5 cm rod with a circular cross section. Each of these 8 tasks was scored either as a one for failure or zero for success. The sum of the scores was the Neurological Severity Score (NSS). These

tests were conducted on Days 2, 5, and 7 following injury. Data are presented as a score ranging from zero to eight, with a high score indicative of impairment.

8.4.9   Long Term Behavioral Evaluations

To determine the presence of long term deficits following fluid percussion injury and minocycline administration, behavioral function was evaluated at 60 days post-FPI. The open field, novel object recognition, and tail suspension were used to assess anxiety, memory, and depression, respectively. Evaluations were recorded and evaluated offline by observers who were blinded to treatment conditions. Animals were acclimated to the testing environment 30 minutes prior to testing. The open field, novel object recognition and tail suspension test were run serially. Open field and novel object recognition tests were run in a 30 cm³ arena painted white and marked with 16 square crossings [152].

8.4.10   Open Field Test

The open field test evaluates locomotor and anxiety like behavior. Mice inherently will avoid brightly lit areas, but also have an innate drive to explore for perceived threats. When these two drives conflict, the result is anxiety. If anxiety increased, the mouse would have had increased preference toward the edges of the box and would have decreased locomotor activity.

To begin the test, the animal was placed in the middle of the empty arena and allowed to explore for five minutes. The movement was tracked by an overheard camera and analyzed offline. The distance traveled, time spent in the center of the arena, and number of entries into the center was recorded.

8.4.11   Novel Object Recognition

Two identical objects are placed in opposing corners of the arena. Animals were placed in the center of the arena with their snouts opposing the objects. Animals were allowed to explore the objects for five minutes and then they were returned to their home cages. One of the objects was removed and a novel object was put in its place. The animals were placed in the arena and allowed to explore for five minutes before returning them to their home cages. The task was recorded by an overhead camera and the amount of time spent with the objects was recorded by blind observers. If no memory impairment was present, the animals spent more time with the novel object.

8.4.12   Tail Suspension

The animal is hung by its tail, taped to a beam approximately 20 cm from the ground for six minutes. During this time, the animal will attempt to escape and reach for the ground. The task was recorded by a camera and the time it takes for the animal to become immobile was calculated offline by blind observers. If depressive like symptoms were present, the animal spent less time attempting to escape.

8.4.13   Animal Perfusions

Within 1 – 3 hours following Day 60 imaging, mice were deeply anesthetized with an intraperitoneal injection of a ketamine (10 mg/kg)/xylazine (1 mg/kg) solution. After deep anesthesia was confirmed with noxious toe pinches, mice were transcardially perfused first with phosphate buffered saline (PBS) until blood was cleared, and then with 20 mL of cold (4 °C), 4% paraformaldehyde solution, 7.2 pH (PFA) [14]. Heads were decapitated and then post-fixed in PFA overnight. Next, lenses were removed from the brain and the brains were removed from the skull [14]. After removal, brains were

immersed in PBS with 30% sucrose in preparation for future cryosectioning and antibody staining.

8.4.14   Image Analysis

Exported 16-bit TIFF files were analyzed in ImageJ (version 1.51i) software (NIH). Each stack for each time point was realigned using "StackReg", a downloadable plug-in, to correct minor misalignment of successive images caused by motion artifacts[153]. After correcting image alignment, an average intensity z projection of 11 successive images acquired in 1 μm z steps was created for each time point. An identical field of view was chosen for each time point to track the same axons over time.

The percent of axons with undulations, varicosities, and terminal bulbs was determined at each time point. Individuals blind to the treatment groups, compared images at the post-injury time points to baseline. Observers used the drawing and region of interest (ROI) tools in ImageJ (version 1.51i) to indicate which axons had the features of damage by drawing a box around the axon and naming it U, V, or T, if the axon exhibited an undulation, varicosities, or a terminal bulb, respectively. Only the damaged axons were counted and not the number of features (i.e., not each swelling) present on the axon since the entire axon may not be in the entire field of view. The ROIs were saved at each time point and uploaded to a Google Drive. The ROIs were tabulated at each time point for each animal in Microsoft ® Excel. Data were presented as the mean ± SEM percentage of axons with each feature at each time point in each treatment group. Data were transferred to GraphPad Prism for statistical analysis.

8.4.15   Progressive Axonal Damage

To demonstrate progressive axonal injury, individual axons were tracked over time. If an axon demonstrated varicosities or an axonal bulb in the baseline image, the damaged axon was excluded from future analysis (approximately one axon per animal had either varicosities or was a terminal bulb in baseline). Undulated axons at the one-hour time point were followed over the course of the experiment and their outcome was recorded as either developing into a varicosity or returning to its baseline state. The percent of undulated axons developing into varicosities or recovering was determined. Axons with varicosities were tracked over time and at the end of the 30-day time period were identified as 1) developed into a terminal bulb or lost axon, 2) recovered (no sign of injury), or 3) unrecovered (varicosities remained). The time point at which the axons exhibited these traits was recorded. The percent of axons developing into a terminal bulb, recovering, or being unrecovered was determined. Additionally, the percent of varicosities was determined at each time point. Data were recorded in Microsoft ® Excel and then transferred to GraphPad Prism for statistical analysis.

8.4.16   Statistical Analysis

Data were expressed as a mean ± SEM of n, where n represents the number of animals used. The data collected was analyzed with GraphPad Prism software. A one-way ANOVA was used to compare mean results. A Bonferri *post hoc* test was used to adjust for multiple comparisons and statistical significance was defined as $p < 0.05$.

8.5   Results

8.5.1   Injury Severity

Animals were either subjected to moderate fluid percussion injury (n=14) or sham injury (n=4), in which the animals undergo the same procedures as the injured group

except the hammer on the device was not allowed to hit the piston. An injury was classified as moderate if the righting time between 6-10 minutes. **Figure 57** represents the mean righting time in each experimental group (TBI-vehicle, n = 5, TBI-45-min minocycline, n =4, TBI-72-hr minocycline, n =5).
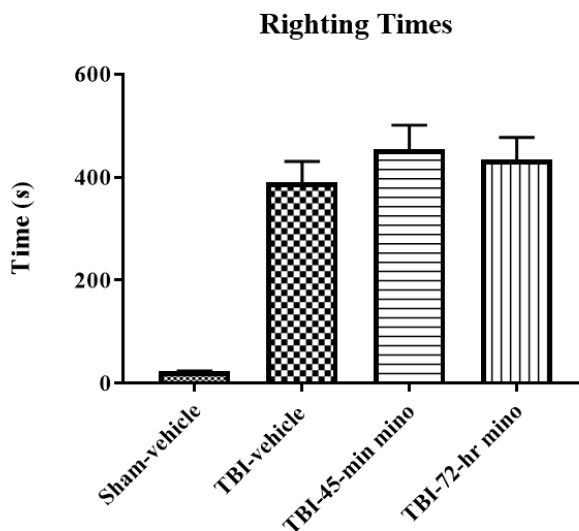
Figure 5-7. Average righting times (s) for each group. All injured groups were subjected to moderate fluid percussion injury. Data is represented a mean ± SEM.

8.5.2 Neurological Severity Score

To assess acute neurological deficits post-injury, a neurological severity score (NSS) was given on Days 2, 5, and 7 post injury by a blinded assessor. On Day 2, as expected, all injured groups, regardless of treatment, had significantly higher NSS than the sham-vehicle treated group. On Days 5 and 7, the TBI-45-min minocycline treated group was not significantly different from the sham-vehicle group. On Day 7, the TBI-72-hr treated minocycline group was not significantly different from the sham-vehicle group. Both treated groups showed signs of neurological recovery by Day 7.
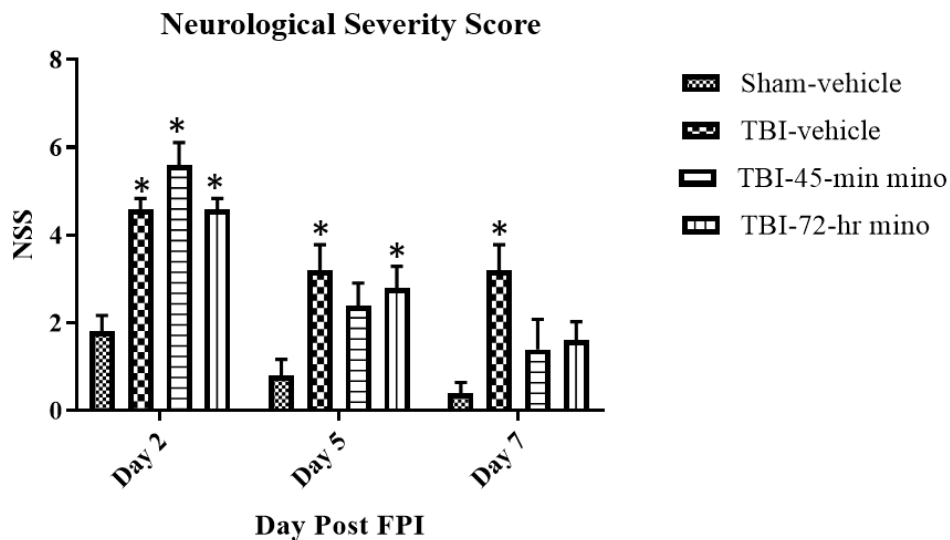
Figure 56. NSS tests results. The TBI-45-min minocycline treated group recovered by Day 5, as it was no longer significantly different than sham-vehicle. At day 7, TBI-72-hr minocycline treated animals were not significantly different than sham-vehicle. The TBI-vehicle treated animals had significant neurological deficits for the first week following injury. Data is represented as mean ± SEM. *p < 0.05 vs. sham-vehicle at the same time point

8.5.3   Rotarod Performance Test

Acute motor deficits were measured on Days 2, 5, and 7 immediately following the NSS assessment. Latency to fall was normalized with baseline values to account for variabilities between animals. The TBI-vehicle treated and TBI-72-hr minocycline treated group had the expected motor deficits as compared to the sham-vehicle treated mice (**Figure 57**). The TBI-45-min minocycline treated group did not have significant motor deficits at Day 2 and performed even better than the sham-vehicle treated group by Day 5. At Day 5, while the TBI-vehicle treated and TBI-72-hr minocycline treated group did not perform significantly worse than the sham-vehicle animals, they still exhibited motor deficits as compared to sham-vehicle.

Rotarod
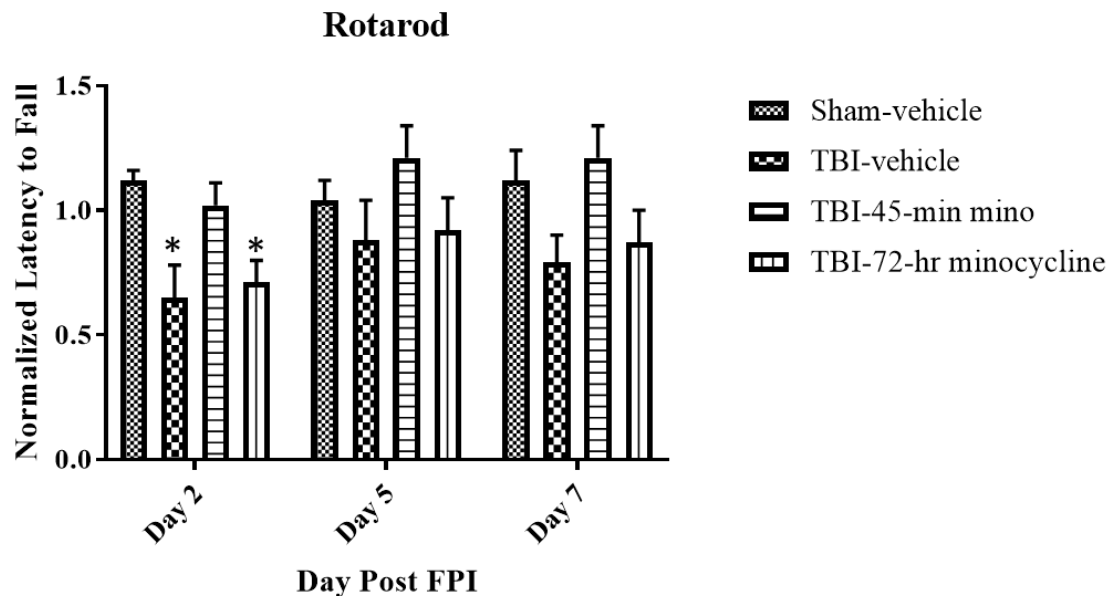
Figure 57. Latency to fall times were normalized with baseline to reduce inter-animal variability. The TBI-45 minute minocycline treated group did not have motor deficits at any time point. Both TBI-vehicle and TBI-72-hr minocycline treated animals had significant motor deficits at Day 2 and continued to exhibit deficits at Day 5 and Day 7 as compared to sham-vehicle treated animals. Data represented as mean ± SEM. * p < 0.05 vs sham-vehicle at each time point

8.5.4   Evidence of Undulated Axons *In Vivo*

Undulations are caused by rapid compression and elongation of axons when the brain is subjected to accelerative forces, causing breaks in the microtubules. Undulations were apparent at the 1 hour time point (**Figure 58B**). Some undulations persisted on Days 3 and 7 but by Day 14, no axons were undulated (**Figure 58A**). Since undulations are a property of mechanical damage, minocycline was not expected to prevent the development of this feature. The groups were not significantly different. While all FPI groups exhibited, on average, more undulated axons following injury than the sham injured group, some animals did not have undulated axons, but already began exhibiting

varicosities. The identification of undulations confirms the *in vitro* and *in silico* work

done by others [141], [142], [148].
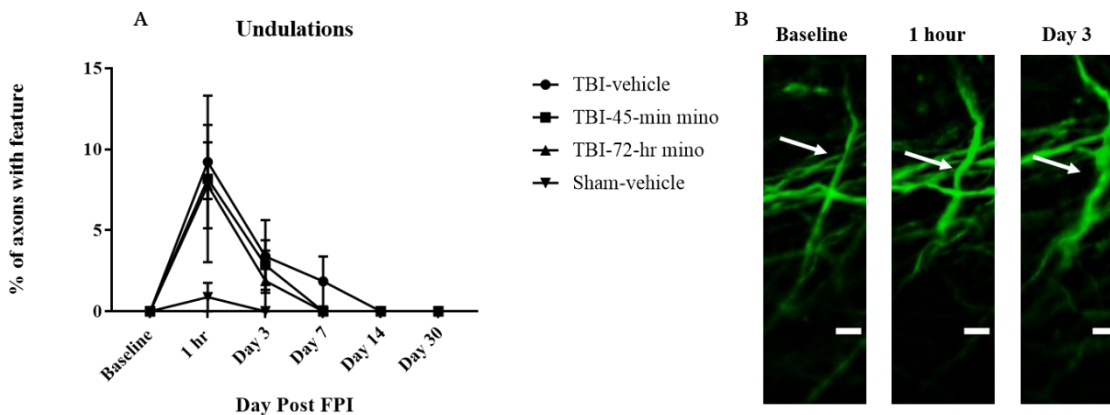
Figure 58. Undulations result from mechanical stretching and elongation of axons. All injured groups exhibited more undulations than the sham injured group **(A)**. Some undulations persisted until Day 7, but by Day 14, no undulations were apparent in any of the injured groups. Representative images of undulated axons (**white arrows**) persisting until day 3 **(B)**. Each image is a z projection of 11 x 1 μm slices. **Scale bar = 10 μm.**

8.5.5   Varicosities Persist Through 30 Days

Following diffuse axonal injury, varicosities are caused by damaged microtubules

and interrupted axonal transport. Axons with varicosities are identified by the presence of

periodic swellings (**Figure 59B, white arrows**). Additionally, secondary injuries, such

as calcium overloads, cause microtubules to break down, leading to the development of

additional varicosities. Beginning at one hour, all groups undergoing injury developed

varicosities, independent of treatment. At Day 3, while both the TBI-vehicle and TBI-72-

hr minocycline treated group had significantly more varicosities than the sham-vehicle

treated group ($p = 0.0195$ and $p = 0.0095$, respectively), the TBI-45-min minocycline

treated group was not significantly different than the sham-vehicle group (**Figure 5-9,**

Day 3). Furthermore, while both the TBI-vehicle and TBI-72-hr minocycline treated

animals had an increase in the percent of axons with varicosities at Day 3 as compared to 1 hour, the TBI-45-min minocycline treated animal had little change. Throughout all time points, the TBI-vehicle treated group exhibited a higher percentage of varicosities with a progressive increase until Day 7, at which point the percent of varicosities begins to decrease, but the percent of axons with varicosities remains higher than the TBI-72-hr minocycline treated or sham-vehicle groups (p = 0.07 and 0.003, respectively) at Day 14 (**Figure 59A, Day 14**). At Day 7, the TBI-45-min minocycline treated group had significantly fewer varicosities than the TBI-vehicle treated group (p = 0.016) (**Figure 5-9A, Day 7**). When minocycline is administered at 72 hours, the average percent of axons with varicosities shows a decrease at Day 7. By Day 14, while it is not significantly different than the TBI-vehicle treated group, the p-value was 0.07, which demonstrates a nonsignificant trend (**Figure 5-9A, Day 14**). Axons in both minocycline treated groups exhibited less damage as compared to the TBI-vehicle treated group.
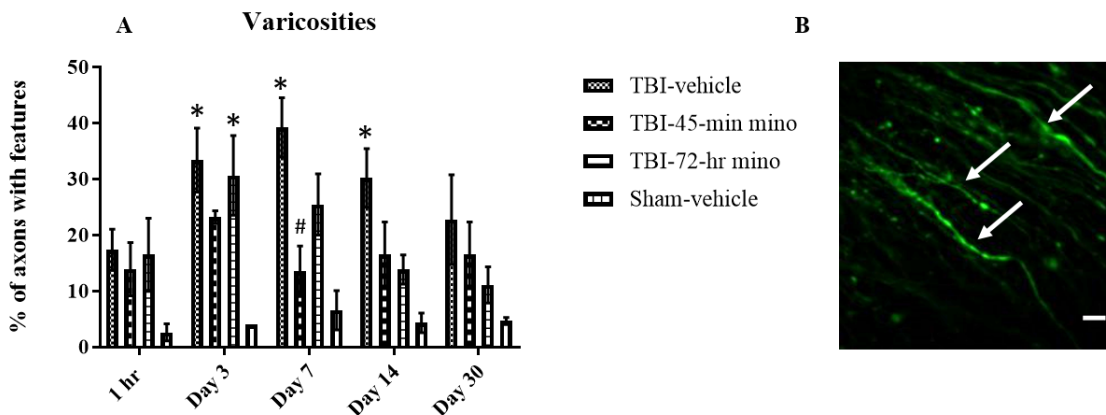
Figure 59. Varicosities develop due to interrupted axonal transport after injury (**white arrows**) **(B)**. The TBI-vehicle treated group developed more varicosities over time versus the sham injured and minocycline treated groups. When minocycline is administered beginning at 45 minutes, it exhibits a protective effect by preventing development of varicosities during the first week and is not significantly different than the sham-vehicle at any time point. Administering minocycline beginning at 72 hours also protects against the development of future varicosities, apparent at day 14 (p = 0.07 versus TBI-vehicle) **(A)**. * $p < 0.05$ (versus sham-vehicle), # $p < 0.05$ (versus TBI-vehicle). Each image is a z projection of 11 x 1 μm slices. **Scale bar = 10 μm (B)**.

8.5.6   Terminal Bulbs and Axon Loss

Persistent varicosities can cause the axon to become weak and eventually lead to disconnection and axon loss. When this occurs, the proximal end of the axon retracts toward the cell body, characterized by a large area of swelling at the end of the axon (**Figure 510C-E**). In this study, terminal bulbs were not counted as axon loss until the terminal bulb was entirely out of the field of view. Additionally, due to the nature of diffuse injury, axon loss would appear to occur without the development of a terminal bulb. The point of disconnection was most likely at a site outside the field of view or terminal bulb development occurred but was not imaged at the time point.

Over time, as expected, the TBI-vehicle treated group had the most terminal bulbs and/or axon loss. While not statistically significant, the TBI-45-min minocycline treated group showed no terminal bulbs or axon loss until Day 14 and Day 30, respectively. In

fact, the TBI-45-min treated group had fewer axonal bulb developments over time than even the sham-vehicle treated group. The TBI-72-hr minocycline treated group had an increase in axonal bulb development and axon loss at Day 14, with this trend persisting until Day 30 (**Figure 510A, B**).
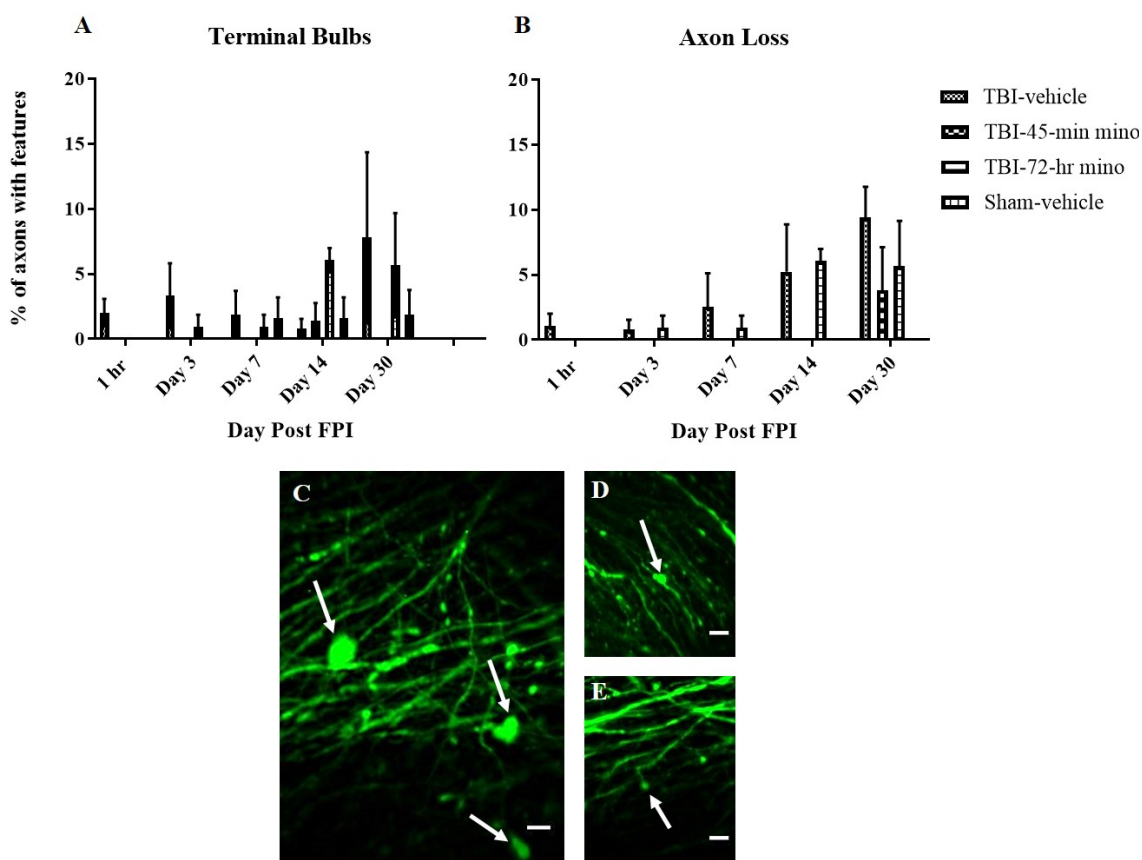
Figure 510. Terminal bulbs develop when an axon disconnects, eventually leading to axon loss. (**A, B**) TBI-vehicle treated had the most persistent axonal bulbs and axonal loss overtime. The TBI-45-min treated minocycline group had few terminal bulbs and minimal axonal loss, with no development until day 14. (**C-E**) Representative images of terminal bulbs (**white arrows**). Each image is a z projection of 11 x 1 μm slices. **Scale bar = 10 μm.**

8.5.7   Progressive Axonal Damage

While identifying features at each time point offers information about the total damage occurring post-injury, it does not demonstrate how the damage progresses. Since minocycline is not administered until after the primary mechanical damage occurs, it does not protect against the development of undulations (**Figure 58A**) and early varicosities (**Figure 59A, 1 hr**). However, when administered in a short window after injury, it was shown to protect the white matter regions of the brain long term [92]. With this novel imaging system, it was possible to track individual axons over time. As a result, a better understanding about the progression of diffuse axonal injury and how and when minocycline exhibits a protective effect was discovered. Damaged axons were tracked over time to determine axon fate. Undulations either developed into varicosities or recovered back to their baseline state. Varicosities, over time, recovered, developed into terminal bulbs, or persisted until the Day 30 time point. The data represented in **Figure 58Figures 5-8, 5-9, and 5-10** were further investigated to determine the time course of injury and minocycline protection.

8.5.8   Undulations

Undulations occur at the moment of injury, and because they involve breaks in microtubules and neurofilaments, they can lead to varicosities (**Figure 511A**). They can also recover back to their baseline state (**Figure 511B**). Since undulations are a direct result of the mechanical forces applied to the brain during injury, minocycline administration protected against the development of these features. However, *in vitro* and *in silico* research has demonstrated undulations develop into varicosities after dynamic stretch injury [141], [142], [148]. This study confirms this mechanical damage *in vivo* as the majority of identified undulated axons developed into varicosities (**Table 5-1**).

Table 51. Undulated axons develop into varicosities. The undulated axons were tracked to determine if they developed into varicosities or recovered. The percent of undulated axons developing into varicosities was calculated. Data is represented as mean ± SEM.

Treatment Group	Undulated Axons (%)	Undulated Axons to varicosities (%)
Sham-vehicle	0.9 ± 0.9	0 ± 0
TBI- vehicle	9.2 ± 2.1	70 ± 20
TBI- 45 min	11.1 ± 5.3	100
TBI- 72 hour	11.9 ± 2.4	86.7 ± 13.3
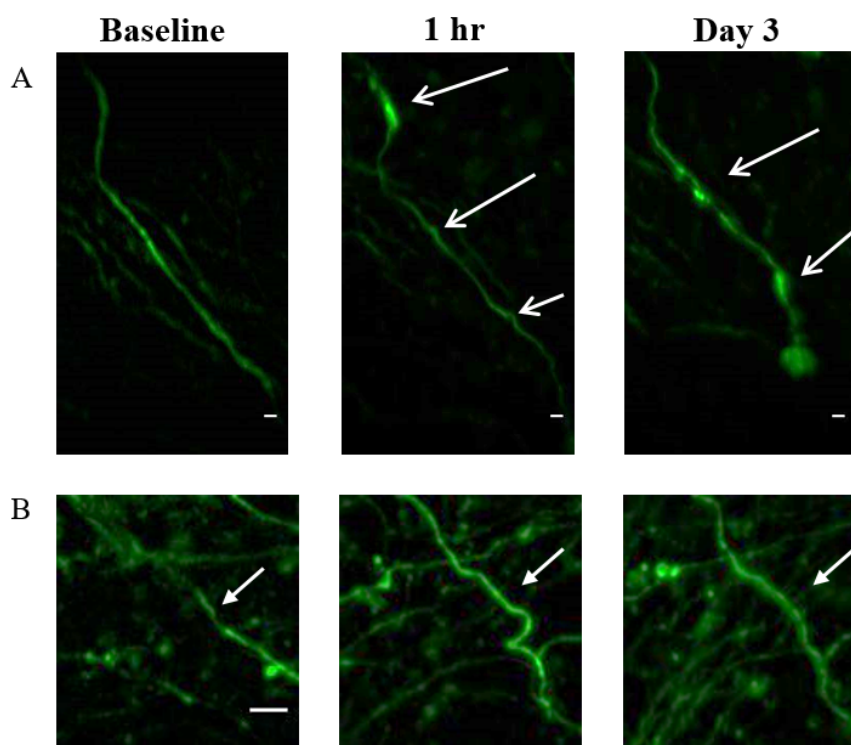
Figure 511. Undulated axons can been seen at 1 hour **(white arrows**) and **A)** develop into varicosities (**white arrows**) or **B)** recover over time (**white arrows**). Each image is a z projection of 11 x 1 μm slices. **A) Scale bar = 5 μm, B) Scale bar = 10 μm.**

8.5.9   Minocycline Mitigates Progressive Damage

The novel imaging system was used to measure the varicosities' fate over 30 days

following TBI to determine the long-term protective properties of minocycline. The

average percent of total axons developing varicosities was measured for each treatment

group. The varicosities were tracked and identified as 1) developing into a terminal bulb or resulting in axon loss, 2) recovering back to baseline state (**Figure 512, solid white arrow**), or remaining unresolved (**Figure 512, white dashed arrow**) during the 30 day time period.
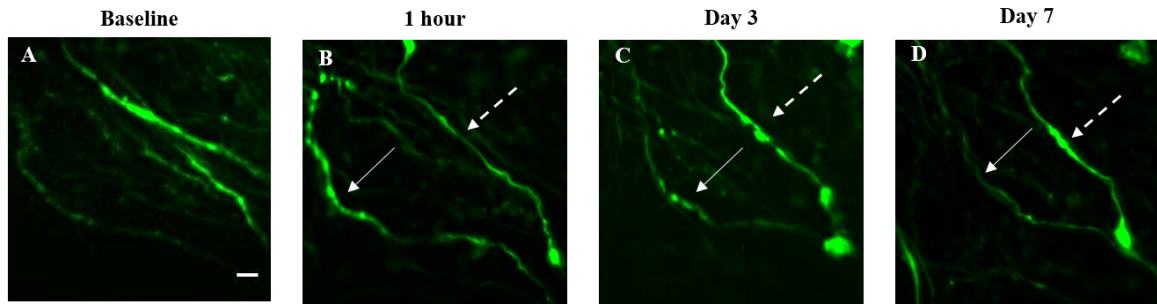
Figure 512. Representative images demonstrating the difference in recovered varicosities (**solid, white arrow**) or unresolved varicosities (**dashed, white arrow**). Each image is a z projection of 11 x 1 μm slices from identical field of views. **Scale bar = 10 μm**.

As expected, the sham-vehicle treated group had significantly fewer varicosities develop over the 30 day time period as compared to TBI-sham treated (p = 0.0009) and TBI-72-hr minocycline treated (p = 0.015) groups (**Table 5-2**), since early damage could not be prevented. The TBI-45-min minocycline treated group had fewer varicosities develop than the TBI-vehicle group (p = 0.056). While the injured groups had more varicosities develop overall than the sham-vehicle treated group, the fate of the axons at Day 30 varied. The TBI-45-min minocycline treated group had less than half (47 ± 20 %) of the axons resolve, while the others remained unresolved (53 ± 20 %) at the 30 day time point. Since this number was similar to the TBI-vehicle treated group (46 ± 6), the percent of varicosities developing into terminal bulbs was considered. The TBI-45-min minocycline-treated group had no tracked varicosities develop into terminal bulbs, while

the TBI-vehicle group had approximately a quarter (27 ± 7 %) develop into terminal

bulbs.

Table 52. Individual axons with varicosities were tracked over 30 days and their fate was assigned as recovered, unresolved, or resulting in a terminal bulb or axon loss for each treatment group. Data is represented as mean ± SEM. * p< 0.05 (vs. sham-vehicle), # p < 0.05 (vs. TBI-vehicle)

Treatment Group	Varicosities formed (%)	Recovered varicosities (%)	Unresolved varicosities (%)	Varicosities resulting in terminal bulbs or axon loss (%)
Sham-vehicle	13.2 ± 1.1	62.5 ± 14.2	29.2 ± 10.5	8.3 ± 8.3
TBI-vehicle	58.5 ± 6.3*	45.8 ± 5.9	30.45 ± 8	27 ± 6.7
TBI- 45-min	35.1 ± 6.6 (p = 0.056 vs TBI-sham)	46.9 ± 21.9	53.1 ± 21.9	0 ± 0 #
TBI- 72-hr	46 ± 4.3*	69.2 ± 8.3	22.5 ± 6.7	5 ± 5 (p = 0.09, vs TBI-sham)

However, while none of the tracked axons developed into terminal bulbs in the

TBI-45-min minocycline treated group, terminal bulbs and axon loss were present (**Table**

53), albeit significantly less than the TBI-vehicle group (p = 0.027). Occasionally,

terminal bulbs and axon loss were identified without the presence of varicosities. Because

the injury was diffuse, the axon could have had varicosities outside of the field of view

(**Figure 5-13**).

Table 53. Average percent of total axons resulting in terminal bulbs or axon loss.
Data is represented as mean ± SEM. * p < 0.05 (vs. sham-vehicle), # p < 0.05 (vs. TBI-vehicle)

Treatment Group	Terminal Bulb and Axon Loss (%)

Sham-vehicle	3.1 ± 1.4
TBI-vehicle	25.3 ± 0.9 *
TBI-45 minute	5.9 ± 4.7 #
TBI-72 hour	9.2 ± 5.3 (p = 0.09 vs TBI-sham)
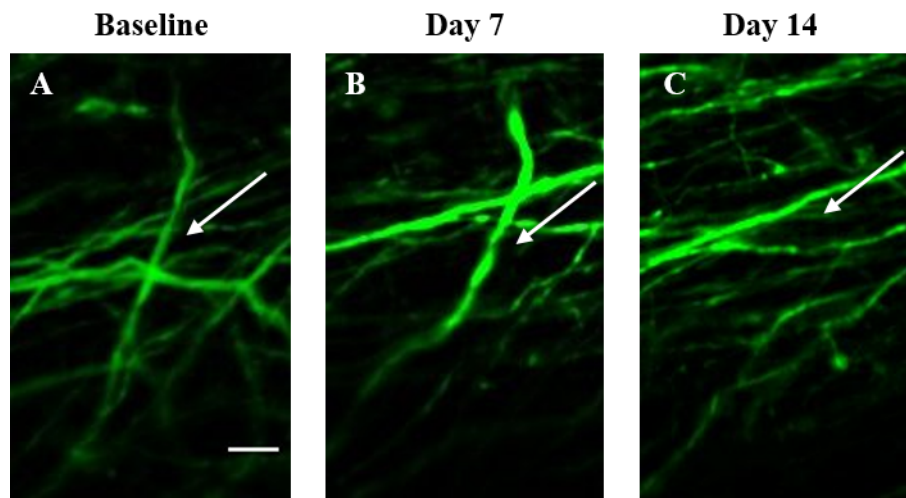
Figure 513. Representative image of axon disappearing (**white arrow**) without the formation of varicosities. It is possible the axon was damaged in an area outside the field of view or the development of a terminal bulb was not identified at the imaging time point. Each image is a z projection of 11 x 1 μm slices. **Scale bar = 10 μm**.

While minocycline may not resolve all varicosities, it protects damaged axons from developing into terminal bulbs and consequently, leading to axon loss (**Table 5-3**). The TBI72hr minocycline treated group had nearly 70% of the varicosities recover and a low percentage of tracked varicosities developed into terminal bulbs (5 ± 5 %, p = 0.09 vs. TBI-vehicle) (**Table 52**). Furthermore, the TBI-72-hr minocycline-treated group had overall fewer terminal bulbs than the TBI-vehicle treated group (p = 0.09) (**Table 53**). This demonstrates by extending the therapeutic window out to 72 hours, axons are protected from loss, and minocycline may be creating an environment where axons are able to recover.

8.5.10   Development of New Varicosities

Varicosities are apparent when mice are imaged at one hour and persist for the 30 day timeframe (**Figure 514, white arrowheads**). Some varicosities are present in the baseline, but these axons were not included in future analysis (**Figure 514 A, G, M, and S**). Furthermore, varicosities can develop due to secondary injuries and are not apparent until later time points (**Figure 514, white arrowheads**). To further investigate if the varicosities persisted over time or if new varicosities were contributing to the overall measurements at each time point, individual axons were tracked to determine the time point at which they developed varicosities.
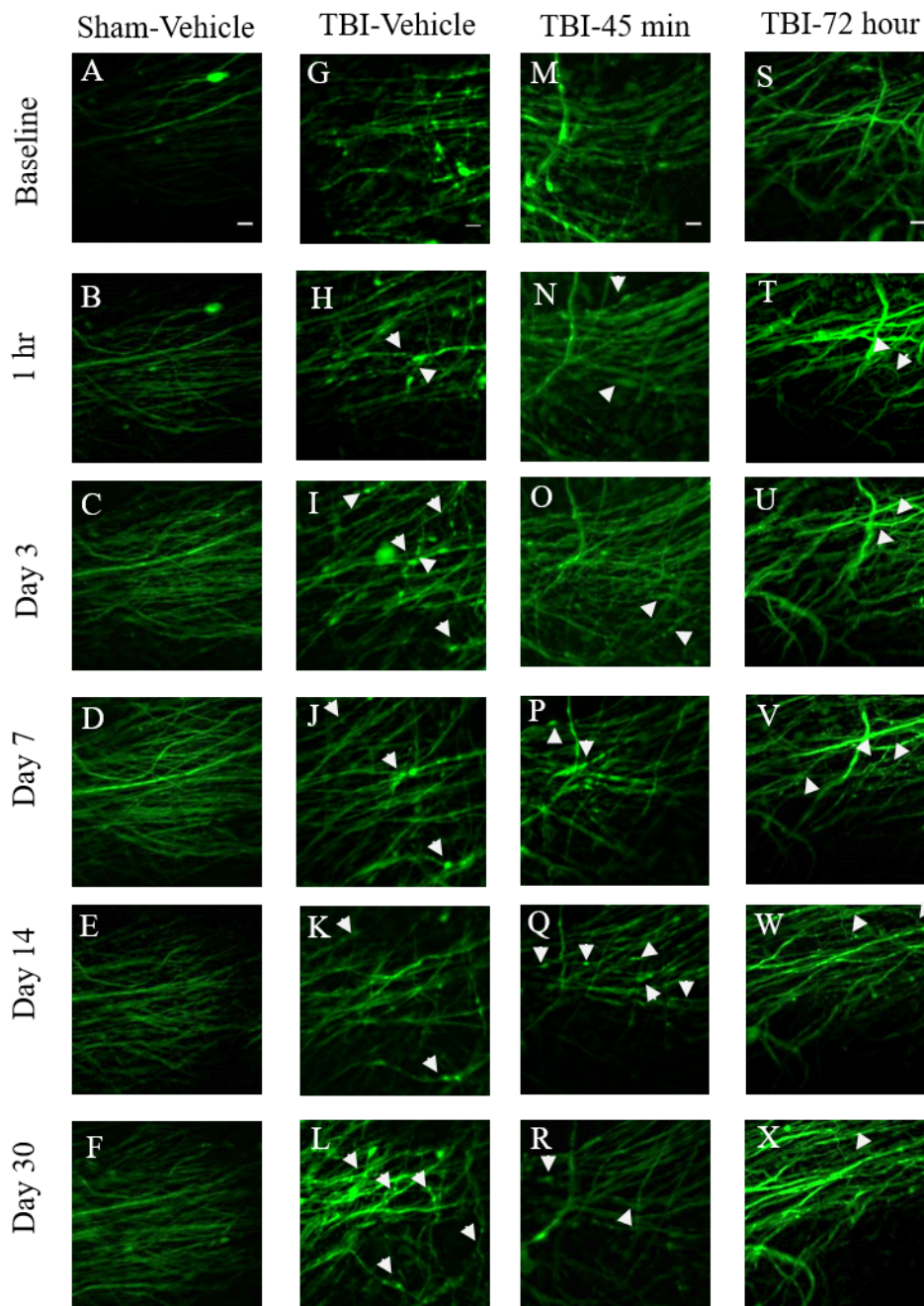
Figure 514. Representative images demonstrating progressive axonal damage for each of the treatment groups. Overall, less damage is apparent in the sham-sham **(A-F)** and groups treated with minocycline at 45 minute **(M-R)** and 72 hours **(S-X).** Individual axons with varicosities (**white arrow heads**) could be tracked over time to determine their fate and time point at which they appear and recover. **Scale bar = 10 μm**.

When minocycline is administered at 45 minutes, no difference is found in the

total percent of undulations or percent of varicosities at the one hour time point, as

compared to the other injured groups (**Figure 58A & Figure 59A**). The protective effect

of minocycline administration beginning at 45 minutes is not seen until Day 7 when the

average percent of varicosities is significantly lower than TBI-vehicle (p = 0.016), and

only 12.5 ± 12.5 % of those are new varicosities (**Table 54**). At Day 3, the TBI-72-hr

minocycline treated group began their treatment. The average percent of varicosities at

Day 3 is not significantly different than the TBI-sham treated group (p > 0.99) (**Figure

59A**). However, at Day 14, the TBI-72-hour minocycline treated group, had a lower

average percent of axons with varicosities than the TBI-vehicle treated group (p = 0.07)

(**Figure 55A**), with 30 ± 20% of the varicosities being new (**Table 54**). At this time

point, TBI-vehicle had the fewest new varicosities developing (18 ± 5 %) (**Table 54**), but

also had the highest percent of terminal bulbs and axon loss (**Figure 58A)** up until this

time point, signifying that a great deal of damage had already occurred.

Table 54. Development of new varicosities over time. The average percent of axons
with new varicosities at each time point was measured. Data are represented as mean ±
SEM.

Treatment Group	1 hr (%)	Day 3 (%)	Day 7 (%)	Day 14 (%)	Day 30 (%)
TBI-vehicle	100	59 ± 14	24 ± 10	18 ± 5	30 ± 21
TBI- 45 min	100	46 ± 21	13 ± 13	25 ± 14	0.0 ± 0.0
TBI-72 hr	100	52 ± 17	37 ± 16	30 ± 20	0.0 ± 0.0

Taken together, minocycline does not have an immediate protective effect, but

takes time to intervene in the progression of axonal damage. Additionally, by

administering minocycline beginning at both 45 minutes and 72 hours, while the time

course of protection is different, no new varicosities develop at 30 days (**Table 54**).

Additionally, the development of terminal bulbs or axonal loss from identified

varicosities is decreased (**Table 52)** and overall the two treated groups had fewer terminal

bulbs develop than the TBI-vehicle treated group (**Table 53**). As a result, while

minocycline cannot protect against the initial mechanical injury, it has a long term role in

mitigating further damage and preventing axon loss.

8.5.11   Late Behavioral Outcomes

Three behavioral tests were used on Day 60 to determine if minocycline protected

late behavioral outcomes: open field, novel object recognition, and tail suspension test.

The open field test was used to measure anxiety like behavior. If animals' spent more

time in the periphery of the arena, anxiety like behavior was present. The novel object

recognition test was used to determine if memory deficits were present. If an animal

spent an equal amount of time with familiar and novel objects, they were not able to

discern between the two objects and memory deficits were present. The tail suspension

test was used to measure depressive like behavior. If animals spent less time actively

attempting to escape while being suspended by their tails, depressive like behaviors were

present.

In the open field test, there was no statistical difference between injured and

uninjured groups. All animals spent a comparable amount of time in the peripheral zones

of the arena, independent of treatment (**Figure 5-15**).

Open Field (Time in Peripheal Zones)
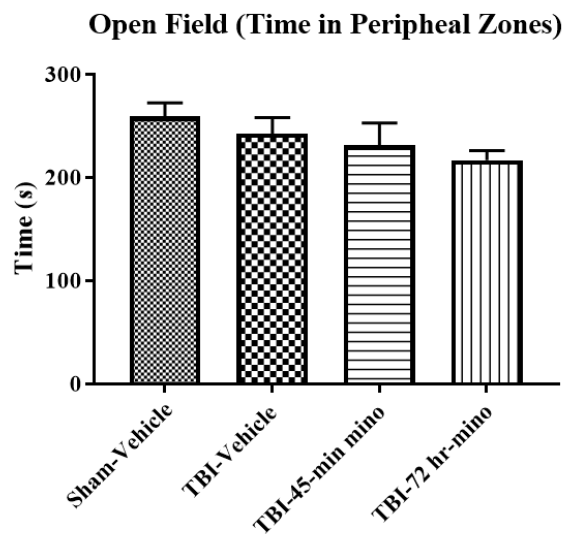
Figure 515. No statistical significant difference was measured between injured and uninjured groups. All animals spent comparable time in the peripheral zones of the arena.

In the tail suspension test, no statistical difference was found between groups. However, the TBI-45-min minocycline treated group and TBI-vehicle treated group spent the least amount of time actively seeking escape, while the TBI-72-hr minocycline treated group spent the most amount of time actively seeking escape.
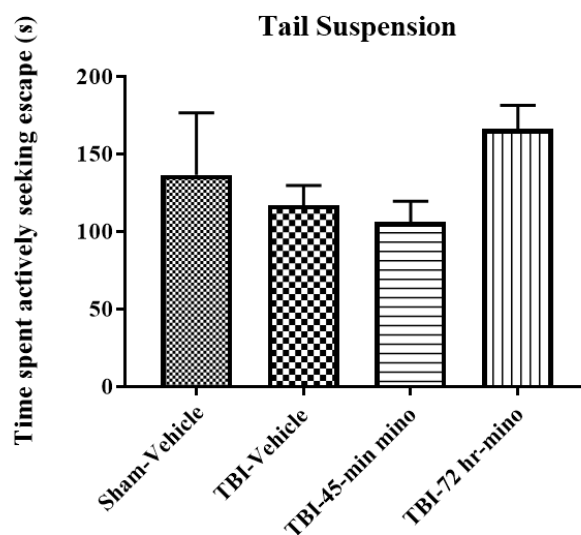
Tail Suspension

Figure 516. There was no statistical difference between injured or uninjured groups in the tail suspension test. However, it appears the TBI-72 hr minocycline treated group spent the most time actively attempting to escape.

In the novel object recognition test, sham-vehicle treated animals spent significantly more time with the novel object than the familiar object (p = 0.016), which is expected. The TBI-vehicle treated animals were not able to discern between the familiar and novel object (p = 0.946), indicating a memory deficit is present long term following TBI. When minocycline was administered 45 minutes following TBI, memory impairment was protected as the TBI-45-min minocycline treated group spent significantly more time (p = 0.045) with the novel object than the familiar object. While the administration of minocycline at 72 hours post TBI appears to be protective against axonal degeneration, it did not protect against memory impairment as the TBI-72-hr treated animals appear to spend more time with the familiar object, indicating memory impairment is present (**Figure 5-17**).
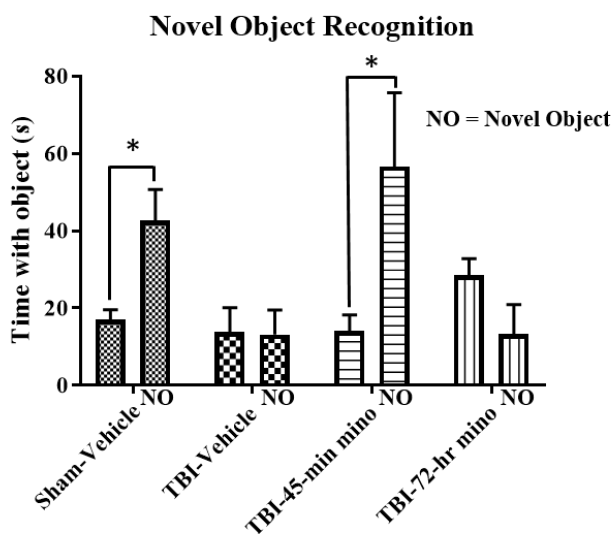
Figure 517. Novel object recognition scores indicate that the TBI-vehicle and TBI-72-hr minocycline treated animals were unable to discern between familiar and novel objects,

indicating a memory deficit is present. Both the sham-vehicle and TBI-45-min minocycline treated spent significantly more time with the novel objects as compared to the familiar objects, indicating administration of minocycline at 45 minutes post TBI is protective against the development of memory deficits. * $p < 0.05$ vs. familiar object

8.6   Discussion and Conclusion

Diffuse axonal injury, while resulting in wide spread damage, primarily affects

the corpus callosum, a region deep within the brain. Rapid compression and elongation of

the tissue causes small breaks in the microtubules and neurofilaments that cause axons to

become undulated. These small breaks disrupt the transport of axonal proteins, resulting

in periodic swellings, called varicosities. The varicosities weaken the axon and can

eventually lead to terminal bulbs and ultimately axon loss. To date, the research

conducted about the progression of these features has been limited to *in vitro*, *in silico*,

and histological studies [7], [36], [141], [142], [144], [148], [154]. While these

techniques are essential, no data were collected *in vivo* to confirm these results, until

now. For the first time, the research conducted in this longitudinal study confirms that the

forces from traumatic brain injury cause undulations, which lead to varicosities, and

ultimately result in terminal bulbs and axonal loss.

Traumatic brain injury affects a large amount of the population, and as result it is

imperative the scientific community discovers therapeutic interventions to diminish the

progression of this injury. Minocycline, an FDA approved antibiotic with anti-

inflammatory properties when given in high doses, has shown promise in mitigating

damage from diffuse axonal injury [87], [153], [92], [154], [155], [91], [94]. While this

drug has shown promise in protecting the white matter in the brain when given in a short

time frame after injury [16], how and when the drug is contributing to this protection is

still unknown. Additionally, it is not always possible to treat individuals immediately

following injury. Therefore, it is necessary to investigate if minocycline exhibits protective effects when administered in a longer therapeutic window. Contributing to this research, the novel longitudinal imaging system used in this study demonstrated both the short and long term effects of the drug and established that administering minocycline at 72 hours after injury has protective properties.

When minocycline is first administered 45 minutes after injury, the effect is not immediate, with no statistical difference measured in the percent of varicosities at the one hour time point (**Figure 59A**). However, the total axon damage is mitigated long term. This mitigation is seen as a smaller percent of axons developing varicosities overall ($p = 0.056$, vs TBI-vehicle) (**Table 52**). In fact at Day 7, the TBI-45-min treated group had significantly fewer varicosities than the TBI-vehicle treated group ($p = 0.016$). Additionally, while some varicosities persisted during the 30 day time frame of the experiment, no new varicosities were present at Day 30 (**Table 54**) and significantly fewer axons resulted in terminal bulbs or axons loss as compared to the TBI-vehicle treated group ($p = 0.027$) (**Table 53**).

The results of the study demonstrated that administering minocycline at 72 hours may be beneficial. Again, when minocycline is first administered, the result is not immediate, and a difference in the percent of varicosities is not seen until Day 14 when compared to the TBI-vehicle treated group ($p = 0.07$) (**Figure 59A**). Furthermore, 70% of the varicosities that developed recovered by ay 30, which was more than both the TBI45min minocycline-treated group (47%) and the TBI-vehicle treated group (46%) (**Table 52**). Similar to the TBI-45-min treated group, the TBI-72-hr treated group had no new varicosities develop at Day 30 (**Table 54**). Additionally, the total terminal bulb

development and axonal loss was less than the TBI-vehicle treated group ($p = 0.095$)

(**Table 53**). These data demonstrate that this longer therapeutic window not only protects

from axon loss, but also creates an environment in which the axons can recover.

Microglia have a key role in the injury cascade following TBI. After injury,

microglia become chronically activated [154], [158] and microglia DNA was found in

white matter regions months after injury in both rats and humans [38]. Minocycline,

given its anti-inflammatory properties, was shown to mitigate microglia activation

following TBI [87], [92], [159]. As a result, the regulation of microglia through

minocycline may be contributing to the protection of axons. While axons develop

varicosities, they are still functional and in some cases, as shown in this study, recover

back to their baseline state. Activated microglia, in order to maintain homeostasis, will

phagocytose damaged material in the brain. However, in this case, creating an

environment in which microglia are not activated may allow for axons to recover from

the varicosities and prevent terminal bulbs from developing.

In late behavioral outcomes, no difference was found in the open field or tail

suspension test, indicating there was no presence of anxiety or depressive like behavior at

60 days post TBI (**Figure 5-15** and **Figure 5-16**). These results are consistent with

another research study, as no anxiety like behaviors were present at 9 weeks post TBI

[93]. However, in the novel object recognition test, the TBI-vehicle and TBI-72-hr

minocycline treated group were unable to discern between the novel and familiar object,

indicating a memory deficit was present at Day 60. In both the sham-vehicle and TBI-45-

min minocycline treated group, animals spent significantly more time exploring the novel

object as compared to the familiar object. These results suggest administration of

minocycline at 45 min, but not at 72 hours post TBI, is protective against the development of memory deficits (**Figure 5-17**).

In summary, this study demonstrated the use of a novel imaging system for identifying the progression of diffuse axonal injury *in vivo* following a fluid percussion injury model. Varicosities developed from undulated axons, recovered, persisted, or advanced into terminal bulbs, which is consisted with other research [121], [142], [145], [148], [160]. Furthermore, this study demonstrated the efficacy of this system in preclinical trials by confirming that when minocycline is administered at 45 minutes after injury, it protects the white matter regions of the brain. Finally, this system was used to determine the effectiveness of expanding the therapeutic window of minocycline treatment to 72 hours after injury. While administration at this late time point cannot protect early damage from progressing, it creates an environment which has long term protective effects. Future studies will include examining the mechanisms of protection, such as mitigating microglia activation over time, which may be contributing to this protection.

CHAPTER 9

CHAPTER 10

IN VIVO DIFFUSION OF PGP

10.1   Poly(lactide-co-glycolide)-Praft-Polyethylenimine

While viral vectors have shown promise as a delivery mechanism for gene therapies, they cause immune responses and lack specificity. As a result, the scientific community has moved toward developing nonviral vectors, which can be manufactured at large scales, decrease off target effects, and reduce the inflammatory response [103]. Poly(lactide-co-glycolide)-praft-polyethylenimine (PgP), a synthetic polymer has previously shown promise as an efficient vector for stable intracellular delivery of nucleic acids, while reducing cytotoxicity as compared to the conventional polyetherimide (PEI) normally used. Additionally, this carrier successfully delivered siRhoA, a gene involved in cytoskeleton regulation, via a local injection after a rat compression spinal cord injury model. The treatment increased axonal regeneration and reduced astrogliosis [104]. Based on these results, PgP carrier may be a candidate for delivering treatment to the brain after diffuse axonal injury, which results in progressive axonal loss.

In order to determine PgP's potential as a delivery platform in brain injury, its diffusion capability in a murine brain was investigated in a short, qualitative study. PgP, loaded with DiR, a lipophilic near infrared fluorescent dye, was locally injected into the brain (n = 4) and imaged through a cranial window over 72 hours to determine its diffusion capabilities.

10.2   Materials and Methods

10.2.1   <u>Preparation of PgP Polyplexes</u>

PgP polyplexes were prepared by Dr. Jeoungsoo Lee's lab at the Clemson University Bioengineering Innovation Campus (CUBEInC), as previously described [103]. Prepared polyplexes, with a molecular weight of 38,168, were sent to Dr. Teresa Murray's lab at Louisiana Tech University.

10.2.2   <u>DiR-PgP Injection</u>

A 1 μL sample of DiR-PgP was loaded into a 5 μL Hamilton syringe (Hamilton Company, Reno, Nevada, USA) and stereotaxically injected through a craniectomy. Mice were briefly anesthetized with 5% isoflurane and then transferred to a stereotaxic frame (Stoelting Co., Wood Dale, Illinois, USA) equipped with ear bars, heating pad, and a nose cone for isoflurane delivery (Leica Biosystems, INC., Buffalo Grove, Illinois,USA). A SomnoSuite® system (Kent Scientific, Torrington, Connecticut, USA) was used to control isoflurane delivery. To ensure the animal was fully anesthetized, toe pinches were performed every 15 minutes. Aseptic surgical techniques were used to make a midline incision, and a surgical bone scraper was used to remove the periosteum. A micro drill and 0.5 mm dental burr were used to make a 2 mm craniectomy in the right hemisphere of the cortex, and the tip of a 28 G hypodermic needle was used at a low angle to the dura to remove the dura [14], [15].

The 5 μL Hamilton syringe was loaded and adjusted until it is over the craniectomy. Positioning was chosen based on the location of large blood vessels, as puncturing these would cause poor imaging quality. The needle was slowly lowered until it just touched the surface of the brain. The z coordinate was recorded and the needle was

lowered 350 μm below the surface of the brain. The needle was then backed out 150 μm

so that it was 200 μm below the surface of the brain. This reversal created a small pocket

for the solution once it was injected. DiR-PgP was injected at a rate of 0.2 μl per minute

until 1 μL of DiR-PgP was injected, and 1.2% low melt agarose (IBI Scientific, Peosta,

Iowa) was placed over the craniectomy and covered with a 5 mm diameter coverslip

(Electron Microscopy Sciences, Hatfield, Pennsylvania, USA). Gel cyanoacrylate

(Loctite) was placed around the edges of the coverslip. A custom designed head plate was

3D printed in-house for use with our TRIO platform imaging support system, which is

also 3D printed in-house [15]. The plastic head plate was aligned with the coverslip and

attached with gel cyanoacrylate (Loctite). All parts were secured with dental adhesive

(RelyX, 3M Corp) before imaging the animal.

10.2.3   Tail Vein Injections

Fluorescein (FITC) conjugated to dextran (Life Technologies ©) was used as a

marker for blood plasma. FITC was injected via the tail vein prior to imaging sessions.

On the first day of imaging (1 hour, 3 hour, and 6 hour time points), FITC was only

injected once to minimize the chance of an overdose.

10.2.4   *In Vivo* Imaging

Mice were briefly anesthetized with 5% isoflurane and then transferred to a TRIO

platform imaging support system, as previously described [15]. Anesthesia was

maintained throughout the imaging session with 1.5% isoflurane. A Chameleon Vision-2

multiphoton laser (80 MHz, Coherent) tuned to 950 nm was used to excite DiR and FITC

fluorescence. Emitted light was filtered through a red and a green fluorescent protein

filter (Brightline® filters, Semrock, Inc). Scanned images were acquired on a custom,

upright, multiphoton microscope system, equipped with a Pockels cell and GaAsP

detectors (Intelligent Imaging Innovations, Inc., Denver, Colorado, USA), a 4x/0.10 NA

objective (Nikon Instruments, Inc., Japan), a 10x/0.4 NA objective (Leica, Germany), and

Slidebook 6 software (3i, Inc.). A pixel dwell time of 2 μs was used with pixel averaging

(5/scan) to acquire three-dimensional (z-stack) images composed of 176 images with a 2

μm step size. Images were acquired at 1 hour, 3 hours, 6 hours, 24 hours, 3 days, and 7

days after initial injection. Image sets were exported and stored as TIFF files on an

external hard drive for offline analysis.

10.2.5   Perfusion and Fixation of Brain Tissue.

Within 1 – 3 hr of post-procedure imaging, mice were deeply anesthetized with an

intraperitoneal injection of a ketamine (10 mg/kg)/xylazine (1 mg/kg) solution. After

confirming deep anesthesia with noxious toe pinches, mice were transcardially perfused

first with phosphate buffered saline (PBS) until blood was cleared and then with 20 mL

of cold (4 °C), 4% paraformaldehyde solution, 7.2 pH (PFA) [14]. Heads were

decapitated and then post-fixed in PFA overnight. [14]. The brain was removed from the

skull and immersed in PBS with 30% sucrose in preparation for future cryosectioning and

antibody staining.

10.2.6   Image Analysis

Image analysis was performed with ImageJ (version 1.51i) software (NIH). Sum

intensity z projections of 11 x 2 μm slices were created for each time point. Background

mean intensity was calculated and subtracted from each image. Brightness and contrast

were adjusted so similar intensity ranges were used across the time points to qualitatively

compare the diffusion of DiR-PgP.

10.3   Results

Time course images of DiR-PgP diffusion were first obtained *in vivo* with a 10x

objective to qualitatively determine if polyplex spread could be visualized over the course

of 72 hours. Beginning at the one hour time point, polyplexes spread from the injection

point and continued to spread outward from the injection site for the entire 72 hour time

period (**Figure 61**). By 24 hours, DiR-PgP spread over the entire imaging plane.

Additionally, the polyplexes seemed to have an affinity for the blood vasculature (**Figure

61F**). To determine if the diffusion was more widespread and that the polyplexes were

not confined by vasculature, later images were taken from mice (n=3) with a 4x

objective.
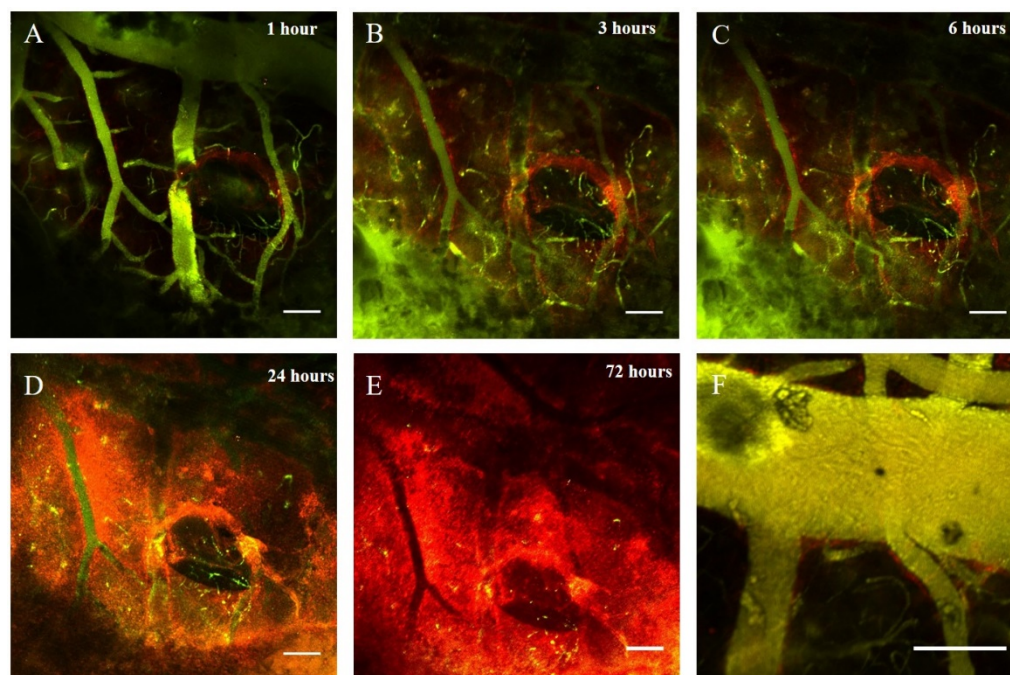
Figure 61. Representative time course images of in vivo diffusion of DiR-PgP with 10x objective. DiR-PgP spreads outward over the 72 hour time period **(A-E).** Polyplexes appear to congregate around the vasculature **(F).** Each image is a z projection of 11 x 1 μm slices. **Scale bars: 100 μm (A-F)**

Visualization with a larger field of view shows DiR-PgP began spreading outwards from the injection site at the one hour time point and continued to spread until it completely covered the field of view at 72 hours. Images were pseudo-colored with the "Jet" look up table in ImageJ (version 1.51i) to better demonstrate the spread of the polyplexes (**Figure 62**). These images demonstrate that DiR-PgP can spread over 72 hours and does not become entrapped by structures, such as vasculature.
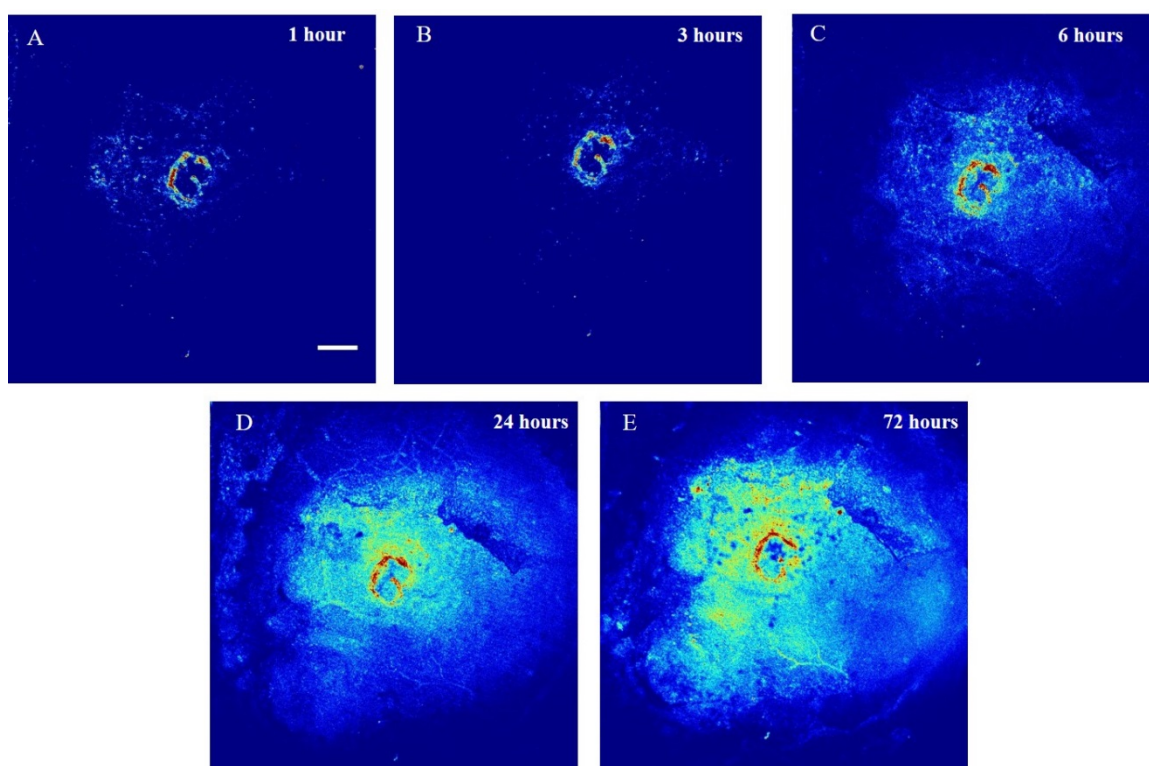
Figure 62. Representative images of DiR-PgP polyplex spread over a 2 mm in diameter craniectomy. Images are pseudo colored with the look up table "Jet" in ImageJ. DiR-PgP spreads outward beginning at 1 hour and continues to spread until it covers the field of view at 72 hours post injection (**A-E**). Each image is a z projection of 11 x 1 μm slices. **Scale bar = 250 μm**.

10.4   Discussion

Delivering effective therapies to the brain is a challenging hurdle which must be overcome, especially in the case of diffuse brain injury, where damage progressively occurs. This short, qualitative study demonstrates that PgP may be a promising carrier for drug therapy in the brain. DiR-PgP diffused over 72 hours, indicating it can efficiently move through the brain. Images were acquired at Day 7, but the damage from the injection led to poor imaging quality and an inability to draw any conclusions. Because of this drawback and since the field of view was limited to a 2 mm diameter cranial window, following the final imaging session, animals were transcardially perfused and brains were stored for future cryosectioning and antibody staining. These future studies will demonstrate the spread of the drug over a seven day time period. Additionally, this study involved a local injection into the brain, which in itself is a penetrating injury. For use in most cases of traumatic brain injury, which are closed head injuries, a local injection would not be feasible. As a result, future studies will further evaluate the potential carrier by systemically injecting the PgP and determining what dose is necessary to effectively reach the brain. Overall, PgP shows promise as an effective platform for delivery and when combined with neuroprotective or neurogenic drugs might mitigate the damage seen in diffuse brain injuries.

CHAPTER 11

CHAPTER 12

CONCLUSIONS AND FUTURE WORKS

A novel imaging system was created by chronically implanting GRIN lenses and multiphoton microscopy was used to image brain dynamics before and after two different brain injury models. Spatiotemporal data was collected related to both stroke and traumatic brain injury. Additionally, two potential therapeutics were tested, Annexin A1 and minocycline, for stroke and TBI, respectively. The novel imaging system successfully imaged both the progression of injury and the effects of the tested therapeutics, demonstrating the ability to use this tool in preclinical trials.

In a model of ischemia/reperfusion, GRIN lenses, were used to image microglia activation before and 24 hours following reperfusion injury. The tool successfully measured microglia activation in subcortical regions of the brain following injury, an area of the brain not previously studied. Furthermore, Annexin A1 was previously shown to modulate the inflammatory response following reperfusion injury and does so through the FPR2/ALX mechanism of action [96], [98]. While the small number of animals was not sufficient to provide statistically significant results, the *in vivo* data suggest that Annexin A1 has the potential to modulate microglia activation in subcortical regions of the brain, but may not do so through this mechanism of action. Furthermore, post mortem analysis with brain slices, while not significant, demonstrated Annexin A1 is effective in protecting the cortex, but not the hippocampus. The novel imaging method used in this

study was able to collect quality images of microglia and it showed results consistent with the brain slice analysis. These results demonstrate the effectiveness of this tool for monitoring microglial activation in a MCAo model and its potential to assess therapeutics.

The same imaging system used to study microglia activation following a model of MCAo was adapted and employed in a model of traumatic brain injury. GRIN lenses were implanted, animals were baseline imaged, and a second surgery was conducted to carry out fluid percussion injury (FPI). In order to use this model, the FPI surgery had to be adapted in order to protect the GRIN lens. Kwik-Sil, a silicone elastomer, was used in place of dental cement to adhere the injury hub to the skull. This elastomer prevented the GRIN lenses from being pulled out upon removal of the injury hub. The research conducted successfully carried out FPI while the GRIN lens was implanted. Spatio-temporal data were collected in the external capsule of Thy1-YFP mice over the course of 30 days. The study had several exciting outcomes, which filled several gaps in knowledge. The novel imaging system, for the first time, confirmed *in vivo* features of diffuse axonal injury that were previously studied *in vitro*, *in silico*, and with histological analysis. The device was successfully used as a tool in a preclinical trial. Longitudinal data were collected to further investigate the time course of a known therapeutic. Minocycline, an FDA approved antibiotic, protects white matter when administered in a short time window following injury [87], [91]–[93]. In this study, when minocycline was administered at 45 minutes following injury, fewer varicosities and terminal bulbs developed as compared to the sham-treated group. Overall, this time point of administration protected the white matter, which is consistent with other research

[91]–[93]. The study expanded the minocycline therapeutic window out to 72 hours. While not as protective as the 45 minute treated animals, the 72 hour window had better outcomes than the TBI-sham-treated animals. While initial damage could not be mitigated, fewer varicosities and terminal bulbs developed, and almost 70% of the damaged varicosities recovered. This recovery demonstrates that minocycline not only protects against axon loss, but is creating an environment in which repair can occur.

Minocycline has anti-inflammatory properties and was shown to mitigate microglia inflammation after injury [87], [92]. The study conducted in Chapter 5 demonstrates that the protective effects of minocycline are time dependent, as it does not have an immediate effect. The same experimental method used in Chapter 5 could be employed to look at the effect of the drug on microglia. It would be interesting to determine if minocycline has a long-term effect on microglia activation or if the protection only occurs while the drug is being administrated. Furthermore, when microglia activation occurs and how this correlates to axonal damage would reveal how and when the environment is changing. This would allow for the optimal therapeutic window to be determined and lead to recovery of the primary mechanical damage.

From the research conducted in Chapter 5, the effect of minocycline is not immediate, but takes time to exhibit protective properties. As a result, it may be beneficial to co-administer this drug with another therapy. For instance, the co-administration of minocycline and N-acetylcysteine at one hour after injury, was shown to preserve the white matter of the brain, and improve spatial learning [161]. Future studies conducted should examine the effect of combinatorial therapeutics at differing time points to discover the best outcome.

Overall, GRIN lens technology has been shown to be effective as a preclinical research tool. The device can collect quality spatiotemporal data in deep regions of the brain, an area inaccessible with current imaging modalities. Imaging windows can be extended out days and even months after injuries occur to identify the time course of injuries. Furthermore, in drug development, the tool makes it possible to track the effects while therapeutics are being administered and identify what occurs once a therapeutic is stopped in the same mouse. This capability not only reduces the inter-animal variability but minimizes the number of animals needed in a study. This device has potential far beyond the studies employed here and will aid other scientists in collecting data about brain dynamics, the progression of brain injuries, and the development of therapeutics.

REFERENCES

[1]   J. Corrigan, A. W. Selassie, and J. A. Orman, "The Epidemiology of Traumatic Brain Injury," *J Head Trauma Rehabil.*, vol. 25, no. 2, pp. 72–80, 2010.

[2]   A. W. Selassie, E. Zaloshnja, J. A. Langlois, T. Miller, P. Jones, and C. Steiner, "Incidence of Long-term Disability Following Traumatic Brain Injury, United States, 2003," vol. 23, no. 2, pp. 123–131, 2008.

[3]   E. Zaloshnja, T. Miller, J. a Langlois, and A. W. Selassie, "Prevalence of long-term disability from traumatic brain injury in the civilian population of the United States, 2005.," *J. Head Trauma Rehabil.*, vol. 23, no. 6, pp. 394–400, 2008.

[4]   J. M. Silver, R. Kramer, S. Greenwald, and M. Weissman, "The association between head injuries and psychiatric disorders: findings from the New Haven NIMH Epidemiologic Catchment Area Study.," *Brain Inj.*, vol. 15, no. August, pp. 935–945, 2001.

[5]   P. Corso, E. Finkelstein, T. Miller, I. Fiebelkorn, and E. Zaloshnja, "Incidence and lifetime costs of injuries in the United States," *Inj Prev*, vol. 12, no. 4, pp. 212–218, 2006.

[6]   A. I. Maas, N. Stocchetti, and R. Bullock, "Moderate and severe traumatic brain injury in adults," *Lancet Neurol.*, vol. 7, no. 8, pp. 728–741, 2008.

[7]   D. H. Smith and D. F. Meaney, "Axonal damage in traumatic brain injury," *Neuroscientist*, vol. 6, no. 6, pp. 483–495, 2000.

[8]   "Stroke Facts." Centers for Disease Control, 2015.

[9]   American Heart Association, "Heart and Stroke Statistics," 2016. [Online]. Available: https://www.heart.org/HEARTORG/General/Heart-and-Stroke-Association-Statistics_UCM_319064_SubHomePage.jsp.

[10]   M. G. Lansberg, E. Bluhmki, and V. N. Thijs, "Efficacy and safety of tissue plasminogen activator 3 to 4.5 hours after acute ischemic stroke:A metaanalysis," *Stroke*, vol. 40, no. 7, pp. 2438–2441, 2009.

[11] E. S. Sena, C. L. Briscoe, D. W. Howells, G. a Donnan, P. a G. Sandercock, and M. R. Macleod, "Factors affecting the apparent efficacy and safety of tissue plasminogen activator in thrombotic occlusion models of stroke: systematic review and meta-analysis.," *J. Cereb. Blood Flow Metab.*, vol. 30, no. 12, pp. 1905–1913, 2010.

[12] T. Mabuchi, K. Kitagawa, T. Ohtsuki, K. Kuwabara, Y. Yagita, T. Yanagihara, M. Hori, M. Matsumoto, D.-I. Chang, and G. J. del Zoppo, "Contribution of microglia/macrophages to expansion of infarction and response of oligodendrocytes after focal cerebral ischemia in rats," *Stroke*, vol. 31, no. 7, pp. 1735–1743, 2000.

[13] T. Cao, T. C. Thomas, J. M. Ziebell, J. R. Pauly, and J. Lifshitz, "Traumatic Brain Injury in the Rat," *Neuroscience*, vol. 225, pp. 65–75, 2012.

[14] S. A. Lee, K. S. Holly, V. Voziyanov, S. L. Villalba, R. Tong, H. E. Grigsby, E. Glasscock, F. G. Szele, I. Vlachos, and T. A. Murray, "Gradient index microlens implanted in prefrontal cortex of mouse does not affect behavioral test performance over time," *PLoS One*, vol. 11, no. 1, 2016.

[15] V. Voziyanov, B. S. Kemp, C. Dressel, and T. A. Murray, "TRIO Platform: A Novel Low Profile In vivo Imaging Support and Restraint System for Mice," *Front. Neurosci.*, vol. 10, no. 67, pp. 1–11, 2016.

[16] R. Diaz Arrastia, P. Kochanek, P. Bergold, K. Kenney, C. Marx, C. J. Grimes, Y. Loh, G. E. Adam, D. Oskvig, K. Curley, and C. W. Salzer, "Pharmacotherapy of Traumatic Brain Injury: State of the Science and the Road Forward: Report of the Department of Defense Neurotrauma Pharmacology Workgroup," *J. neurotrauma2*, vol. 31, no. 2, pp. 135–158, 14AD.

[17] D. J. Schretlen and A. M. Shapiro, "A quantitative review of the effects of traumatic brain injury on cognitive functioning," *Int. Rev. Psychiatry*, vol. 15, no. 4, pp. 341–349, 2003.

[18] D. Hoofien, A. Gilboa, E. Vakil, and P. J. Donovick, "Traumatic brain injury (TBI) 10-20 years later: a comprehensive outcome study of psychiatric symptomatology, cognitive abilities and psychosocial functioning.," *Brain Inj.*, vol. 15, no. 3, pp. 189–209, 2001.

[19] J. Shames, I. Treger, H. Ring, and S. Giaquinto, "Return to Work following traumatic brain injury: Trends and challenges," *Disability & Rehabilitation*, vol. 29, no. 17. pp. 1387–1395, 2007.

[20] H. S. Levin, S. A. Brown, J. X. Song, S. R. McCauley, C. Boake, C. F. Contant, H. Goodman, and K. J. Kotrla, "Depression and posttraumatic stress disorder at three months after mild to moderate traumatic brain injury," *J. Clin. Exp. Neuropsychol.*, vol. 23, no. 6, pp. 754–769, 2001.

[21]   J. L. Ponsford, M. G. Downing, J. Olver, M. Ponsford, R. Acher, M. Carty, and G. Spitz, "Longitudinal follow-up of patients with traumatic brain injury: outcome at two, five, and ten years post-injury.," *J. Neurotrauma*, vol. 31, no. 1, pp. 64–77, 2014.

[22]   S. Maday, A. E. Twelvetrees, A. J. Moughamian, and E. L. F. Holzbaur, "Axonal Transport: Cargo-Specific Mechanisms of Motility and Regulation," *Neuron*, vol. 84, no. 2, pp. 292–309, 2014.

[23]   C. Koch, "Action Propagation in Myelinated Fibers," in *Biophysics of Computation*, New York: Oxford University Press, 1999, pp. 164–168.

[24]   A. Sierra, F. de Castro, J. del Río-Hortega, J. Rafael Iglesias-Rozas, M. Garrosa, and H. Kettenmann, "The 'Big-Bang' for modern glial biology: Translation and comments on Pío del Río-Hortega 1919 series of papers on microglia," *Glia*, vol. 64, no. 11, pp. 1801–1840, 2016.

[25]   J. a Glenn, S. a Ward, C. R. Stone, P. L. Booth, and W. E. Thomas, "Characterisation of ramified microglial cells: detailed morphology, morphological plasticity and proliferative capability.," *J. Anat.*, vol. 180, pp. 109–118, 1992.

[26]   D. J. Loane and K. R. Byrnes, "Role of Microglia in Neurotrauma David," *Neurotherapeutics.*, vol. 7, no. 4, pp. 366–377, 2010.

[27]   C. Obreja, "The stereotactical phenomena in traumatic brain injury biomechanics-diffuse axonal injury and brain concussion," *Restor. Neurol. Neurosci.*, vol. 16, pp. 310–311, 2000.

[28]   R. R. Benson, S. a Meda, S. Vasudevan, Z. Kou, K. a Govindarajan, R. a Hanks, S. R. Millis, M. Makki, Z. Latif, W. Coplin, J. Meythaler, and E. M. Haacke, "Global white matter analysis of diffusion tensor images is predictive of injury severity in traumatic brain injury.," *J. Neurotrauma*, vol. 24, no. 3, pp. 446–459, 2007.

[29]   D. R. Rutgers, F. Toulgoat, J. Cazejust, P. Fillard, P. Lasjaunias, and D. Ducreux, "White matter abnormalities in mild traumatic brain injury: A diffusion tensor imaging study," *Am. J. Neuroradiol.*, vol. 29, no. 3, pp. 514–519, 2008.

[30]   J. Xu, I.-A. Rasmussen, J. Lagopoulos, and A. Håberg, "Diffuse axonal injury in severe traumatic brain injury visualized using high-resolution diffusion tensor imaging.," *J. Neurotrauma*, vol. 24, no. 5, pp. 753–765, 2007.

[31]   K. M. Kinnunen, R. Greenwood, J. H. Powell, R. Leech, P. C. Hawkins, V. Bonnelle, M. C. Patel, S. J. Counsell, and D. J. Sharp, "White matter damage and cognitive impairment after traumatic brain injury," *Brain*, vol. 134, no. 2, pp. 449–463, 2011.

[32]   A. L. Alexander, J. E. Lee, M. Lazar, and A. S. Field, "Diffusion tensor imaging of the brain.," *Neurotherapeutics*, vol. 4, no. 3, pp. 316–29, 2007.

[33]   C. Werner and K. Engelhard, "Pathophysiology of traumatic brain injury," *Br. J. Anaesth.*, vol. 99, no. 1, pp. 4–9, 2007.

[34]   E. Park, J. D. Bell, and A. J. Baker, "Traumatic brain injury: Can the consequences be stopped?," *CMAJ*, vol. 178, no. 9, pp. 1163–1170, 2008.

[35]   J. M. Ziebell and M. C. Morganti-Kossmann, "Involvement of pro- and anti-inflammatory cytokines and chemokines in the pathophysiology of traumatic brain injury," *Neurother. J. Am. Soc. Exp. Neurother.*, vol. 7, no. 1, pp. 22–30, 2010.

[36]   V. E. Johnson, W. Stewart, and D. H. Smith, "Axonal Pathology in Traumatic Brain Injury Victoria," *Exp. Neurol.*, pp. 35–43, 2013.

[37]   A. F. Ramlackhansingh, D. J. Brooks, R. J. Greenwod, S. K. Bose, F. Turkheimer, K. M. Kinnunen, S. Gentleman, R. A. Heckemann, K. Gunanayagam, G. Gelosa, and D. J. Sharp, "Inflammation after Trauma : Microglial Activation and Traumatic Brain Injury Inflammation after Trauma," *Ann. Neurol.*, vol. 70, no. 3, pp. 374–383, 2011.

[38]   S. Williams, R. Raghupathi, M.-A. MacKinnon, T. K. McIntosh, K. E. Saatman, and D. I. Graham, "In situ DNA fragmentation occurs in white matter up to 12 months after head injury in man," *Acta Neuropathol.*, vol. 102, pp. 581–590, 2001.

[39]   K. L. Felmingham, I. J. Baguley, and A. M. Green, "Effects of diffuse axonal injury on speed of information processing following severe traumatic brain injury," *Neuropsychology*, vol. 18, no. 3, pp. 564–571, 2004.

[40]   G. Wang, J. Zhang, X. Hu, L. Zhang, L. Mao, X. Jiang, A. K.-F. Liou, R. K. Leak, Y. Gao, and J. Chen, "Microglia/macrophage polarization dynamics in white matter after traumatic brain injury.," *J. Cereb. Blood Flow Metab.*, vol. 33, no. 12, pp. 1864–74, 2013.

[41]   C. N. Winston, A. Noël, A. Neustadtl, M. Parsadanian, D. J. Barton, D. Chellappa, T. E. Wilkins, A. D. Alikhani, D. N. Zapple, S. Villapol, E. Planel, and M. P. Burns, "Dendritic Spine Loss and Chronic White Matter Inflammation in a Mouse Model of Highly Repetitive Head Trauma," *Am. J. Pathol.*, vol. 186, no. 3, 2016.

[42]   K. D. Kochanek, S. L. Murphy, J. Xu, E. Arias, and D. Ph, "Mortality in the United States," *Bost. Med. Surg. J.*, vol. 22, no. 3, pp. 46–47, 2013.

[43]   H. W. Morrison and J. A. Filosa, "A quantitative spatiotemporal analysis of microglia morphology during ischemic stroke and reperfusion," *J. Neuroinflammation*, vol. 10, no. 1, pp. 1–20, 2013.

[44]   K. Doyle, R. Simon, and M. Stenzel-poore, "Mechanisms of Ischemic Brain Damage – Review Article," *Neuropharmacology*, vol. 55, no. 3, pp. 310–318, 2008.

[45] R. A. Taylor and L. H. Sansing, "Microglial responses after ischemic stroke and intracerebral hemorrhage," *Clin. Dev. Immunol.*, vol. 2013, pp. 1–10, 2013.

[46] F. Helmchen and W. Denk, "Deep tissue two-photon microscopy.," *Nat. Methods*, vol. 2, no. 12, pp. 932–940, 2005.

[47] W. R. Zipfel, R. M. Williams, and W. W. Webb, "Nonlinear magic : multiphoton microscopy in the biosciences," *Nat. Biotechnol.*, vol. 21, no. 11, pp. 1369–1378, 2003.

[48] A. Ustione and D. W. Piston, "A simple introduction to multiphoton microscopy," *J. Microsc.*, vol. 243, no. 3, pp. 221–226, 2011.

[49] J. Bewersdorf, R. Pick, and S. W. Hell, "Multifocal multiphoton microscopy," *Opt. Lett.*, vol. 23, no. 9, pp. 655–657, 1998.

[50] R. Williams, W. Zipfel, and W. Webb, "Multiphoton microscopy in biological research," *Curr. Opin. Chem. Biol.*, vol. 5, pp. 603–608, 2001.

[51] K. Svoboda, W. Denk, D. Kleinfeld, and D. W. Tank, "In vivo dendritic calcium dynamics in neocortical pyramidal neurons," *Lett. to Nat.*, vol. 385, pp. 161–165, 1997.

[52] R. Mostany and C. Portera-Cailliau, "A craniotomy surgery procedure for chronic brain imaging.," *J. Vis. Exp.*, vol. 5, no. 12, pp. 2–3, 2008.

[53] A. Mizrahi, "High-Resolution In Vivo Imaging of Hippocampal Dendrites and Spines," *J. Neurosci.*, vol. 24, no. 13, pp. 3147–3151, 2004.

[54] J. Grutzendler, N. Kasthuri, and W. Gan, "Long-term dendritic spine stabilityin the adult cortex," *Lett. to Nat.*, vol. 420, pp. 1–5, 2002.

[55] J. T. Trachtenberg, B. E. Chen, G. W. Knott, G. Feng, J. R. Sanes, E. Welker, and K. Svoboda, "Long-term in-vivo imaging of experience-dependent synaptic plasticity in adult cortex," *Nature*, vol. 420, pp. 788–94, 2002.

[56] F. Engert and T. Bonhoeffer, "Dendritic spine changes associated with hippocampal long-term synaptic plasticity," *Nature*, vol. 399, no. 6731, pp. 66–70, 1999.

[57] P. Golshani and C. Portera-Cailliau, "In Vivo 2-Photon Calcium Imaging in Layer 2/3 of Mice," *J. Vis. Exp.*, vol. 1, no. 13, pp. 12–13, 2008.

[58] C. Stosiek, O. Garaschuk, K. Holthoff, and A. Konnertht, "In vivo two-photon calcium imaging of neuronal Networks," *Proc. Natl. Acad. Sci. U. S. A.*, vol. 100, no. 12, pp. 7319–7324, 2011.

[59] J. N. D. Kerr, D. Greenberg, and F. Helmchen, "Imaging input and output dynamics of neocortical networks in vivo," *Proc. Natl. Acad. Sci.*, vol. 102, no. 40, pp. 14125–14126, 2005.

[60] M. Mank, A. F. Santos, S. Direnberger, T. D. Mrsic-Flogel, S. B. Hofer, V. Stein, T. Hendel, D. F. Reiff, C. Levelt, A. Borst, T. Bonhoeffer, M. Hübener, and O. Griesbeck, "A genetically encoded calcium indicator for chronic in vivo two-photon imaging," *Nat. Methods*, vol. 5, no. 9, pp. 805–811, 2008.

[61] G. J. Goldey, D. K. Roumis, L. L. Glickfeld, A. M. Kerlin, R. Clay, V. Bonin, D. P. Schafer, and M. L. Andermann, "Long-term imaging in awake mice using removable cranial windows," *Nat. Protoc.*, vol. 9, no. 11, pp. 2515–2538, 2015.

[62] H. Dana, T. W. Chen, A. Hu, B. C. Shields, C. Guo, L. L. Looger, D. S. Kim, and K. Svoboda, "Thy1-GCaMP6 transgenic mice for neuronal population imaging in vivo," *PLoS One*, vol. 9, no. 9, pp. 1–20, 2014.

[63] C. E. Brown, J. D. Boyd, and T. H. Murphy, "Longitudinal in vivo imaging reveals balanced and branch-specific remodeling of mature cortical pyramidal dendritic arbors after stroke," *J. Cereb. Blood Flow Metab.*, vol. 30, no. 4, pp. 783–791, 2010.

[64] S. Fumagalli, C. Perego, F. Ortolano, and M.-G. De Simoni, "Cx3cr1 deficiency induces an early protective inflammatory environment in ischemic mice," *Glia*, vol. 61, no. 6, pp. 827–842, 2013.

[65] S. Bok, T. Wang, C.-J. Lee, S.-U. Jeon, Y.-E. Kim, J. Kim, B.-J. Hong, C. J. Yoon, S. Kim, S.-H. Lee, H. J. Kim, I. H. Kim, K. H. Kim, and G.-O. Ahn, "In vivo imaging of activated microglia in a mouse model of focal cerebral ischemia by two-photon microscopy," *Biomed. Opt. Express*, vol. 6, no. 9, p. 3303, 2015.

[66] V. Jolivel, F. Bicker, F. Binamé, R. Ploen, S. Keller, R. Gollan, B. Jurek, J. Birkenstock, L. Poisa-Beiro, J. Bruttger, V. Opitz, S. C. Thal, A. Waisman, T. Bäuerle, M. K. Schäfer, F. Zipp, and M. H. H. Schmidt, "Perivascular microglia promote blood vessel disintegration in the ischemic penumbra," *Acta Neuropathol.*, vol. 129, no. 2, pp. 279–295, 2015.

[67] E. J. Yoder and D. Kleinfeld, "Cortical imaging through the intact mouse skull using two-photon excitation laser scanning microscopy," *Microsc. Res. Tech.*, vol. 56, no. 4, pp. 304–305, 2002.

[68] H. T. Xu, F. Pan, G. Yang, and W. B. Gan, "Choice of cranial window type for in vivo imaging affects dendritic spine turnover in the cortex," *Nat. Neurosci.*, vol. 10, no. 5, pp. 549–551, 2007.

[69] Y. Zuo, A. Lin, P. Chang, and W. B. Gan, "Development of long-term dendritic spine stability in diverse regions of cerebral cortex," *Neuron*, vol. 46, no. 2, pp. 181–189, 2005.

[70] P. J. Drew, A. Y. Shih, J. D. Driscoll, P. M. Knutsen, P. Blinder, D. Davalos, K. Akassoglou, P. S. Tsai, and D. Kleinfeld, "Chronic optical access through a polished and reinforced thinned skull," *Nat. Methods*, vol. 7, no. 12, pp. 981–984, 2010.

[71] J.-H. Park, W. Sun, and M. Cui, "High-resolution in vivo imaging of mouse brain through the intact skull," *Proc. Natl. Acad. Sci.*, vol. 112, no. 30, pp. 9236–9241, 2015.

[72] G. Yang, F. Pan, C. N. Parkhurst, J. Grutzendler, and W. B. Gan, "Thinned-skull cranial window technique for long-term imaging of the cortex in live mice.," *Nat. Protoc.*, vol. 5, no. 2, pp. 201–208, 2010.

[73] W. Zhang, L. Zhang, B. Liang, D. Schroeder, Z. W. Zhang, G. A. Cox, Y. Li, and D. T. Lin, "Hyperactive somatostatin interneurons contribute to excitotoxicity in neurodegenerative disorders," *Nat. Neurosci.*, vol. 19, no. 4, pp. 557–559, 2016.

[74] R. H. Christie, B. J. Bacskai, W. R. Zipfel, R. M. Williams, S. T. Kajdasz, W. W. Webb, and B. T. Hyman, "Growth arrest of individual senile plaques in a model of Alzheimer's disease observed by in vivo multiphoton microscopy.," *J. Neurosci.*, vol. 21, no. 3, pp. 858–864, 2001.

[75] B. J. Bacskai, S. T. Kajdasz, R. H. Christie, C. Carter, D. Games, P. Seubert, D. Schenk, and B. T. Hyman, "Imaging of amyloid-?? deposits in brains of living mice permits direct observation of clearance of plaques with immunotherapy," *Nat. Med.*, vol. 7, no. 3, pp. 369–372, 2001.

[76] I. R. Winship and T. H. Murphy, "In Vivo Calcium Imaging Reveals Functional Rewiring of Single Somatosensory Neurons after Stroke," *J. Neurosci.*, vol. 28, no. 26, pp. 6592–6606, 2008.

[77] Y. Min, H. Li, K. Xu, Y. Huang, J. Xiao, W. Wang, L. Li, T. Yang, L. Huang, L. Yang, H. Jiang, Q. Wang, M. Zhao, H. R. Hua, R. Mei, and F. Li, "Minocycline-suppression of early peripheral inflammation reduces hypoxia-induced neonatal brain injury," *Front. Neurosci.*, vol. 11, no. SEP, pp. 1–14, 2017.

[78] T. A. Murray and M. J. Levene, "Singlet gradient index lens for deep in vivo multiphoton microscopy," *J. Biomed. Opt.*, vol. 17, no. 2, p. 21106, 2012.

[79] M. J. Levene, D. A. Dombeck, K. A. Kasischke, R. P. Molloy, and W. W. Webb, "In vivo multiphoton microscopy of deep brain tissue," *J Neurophysiol*, vol. 91, no. 4, pp. 1908–1912, 2004.

[80] J. C. Jung, A. D. Mehta, E. Aksay, R. Stepnoski, and M. J. Schnitzer, "In vivo mammalian brain imaging using one- and two-photon fluorescence microendoscopy.," *J. Neurophysiol.*, vol. 92, no. 5, pp. 3121–3133, 2004.

[81] R. P. J. Barretto, B. Messerschmidt, and M. J. Schnitzer, "In vivo fluorescence imaging with high-resolution microlenses," *Nat. Methods*, vol. 6, no. 7, pp. 511–512, 2009.

[82] M. E. Bocarsly, W. Jiang, C. Wang, J. T. Dudman, N. Ji, and Y. Aponte, "Minimally invasive microendoscopy system for in vivo functional imaging of deep nuclei in the mouse brain," *Biomed. Opt. Express*, vol. 6, no. 11, p. 4546, 2015.

[83] R. P. J. Barretto, T. H. Ko, J. C. Jung, T. J. Wang, G. Capps, A. C. Waters, Y. Ziv, A. Attardo, L. Recht, and M. J. Schnitzer, "Time-lapse imaging of disease progression in deep brain areas using fluorescence microendoscopy," *Nat. Med.*, vol. 17, no. 2, pp. 223–228, 2013.

[84] C. J. Engelbrecht, R. S. Johnston, E. J. Seibel, and F. Helmchen, "Ultra-compact fiber-optic two-photon microscope for functional fluorescence imaging in vivo.," *Opt. Express*, vol. 16, no. 8, pp. 5556–5564, 2008.

[85] M. Sato, Y. Motegi, S. Yagi, K. Gengyo-ando, M. Ohkura, and J. Nakai, "Fast varifocal two-photon microendoscope for imaging neuronal activity in the deep brain," *Biomed. Opt. Express*, vol. 8, no. 9, p. 4049, 2017.

[86] N. Garrido-Mesa, A. Zarzuelo, and J. Gálvez, "Minocycline: Far beyond an antibiotic," *Br. J. Pharmacol.*, vol. 169, no. 2, pp. 337–352, 2013.

[87] T. Kielian, N. Esen, S. Liu, N. K. Phulwani, M. M. Syed, N. Phillips, K. Nishina, A. L. Cheung, J. D. Schwartzman, and J. J. Ruhe, "Minocycline modulates neuroinflammation independently of its antimicrobial activity in Staphylococcus aureus-induced brain abscess," *Am. J. Pathol.*, vol. 171, no. 4, pp. 1199–1214, 2007.

[88] H. S. Kim and Y. H. Suh, "Minocycline and neurodegenerative diseases," *Behav. Brain Res.*, vol. 196, no. 2, pp. 168–179, 2009.

[89] R. Diaz-Arrastia, P. M. Kochanek, P. Bergold, K. Kenney, C. E. Marx, C. J. B. Grimes, L. T. C. Y. Loh, L. T. C. G. E. Adam, D. Oskvig, K. C. Curley, and W. Salzer, "Pharmacotherapy of traumatic brain injury: state of the science and the road forward: report of the Department of Defense Neurotrauma Pharmacology Workgroup.," *J. Neurotrauma*, vol. 31, no. 2, pp. 135–58, 2014.

[90] N. Bye, M. D. Habgood, J. K. Callaway, N. Malakooti, A. Potter, T. Kossmann, and M. C. Morganti-Kossmann, "Transient neuroprotection by minocycline following traumatic brain injury is associated with attenuated microglial activation but no changes in cell apoptosis or neutrophil infiltration," *Exp. Neurol.*, vol. 204, no. 1, pp. 220–233, 2007.

[91]   E. Siopi, A. H. Cho, S. Homsi, N. Croci, M. Plotkine, C. Marchand-Leroux, and M. Jafarian-Tehrani, "Minocycline Restores sAPPα Levels and Reduces the Late Histopathological Consequences of Traumatic Brain Injury in Mice," *J. Neurotrauma*, vol. 28, no. 10, pp. 2135–2143, 2011.

[92]   S. Homsi, T. Piaggio, N. Croci, F. Noble, M. Plotkine, C. Marchand-Leroux, and M. Jafarian-Tehrani, "Blockade of acute microglial activation by minocycline promotes neuroprotection and reduces locomotor hyperactivity after closed head injury in mice: a twelve-week follow-up study," *J Neurotrauma*, vol. 27, no. 5, pp. 911–921, 2010.

[93]   E. Siopi, G. Llufriu-Daben, F. Fanucchi, M. Plotkine, C. Marchand-Leroux, and M. Jafarian-Tehrani, "Evalualtion of late cognitive impairment and anxiety states folloing traumatic brain injury in mice: The effect of minocycline," *Neurosci. Lett.*, vol. 511, pp. 110–115, 2012.

[94]   M. D. Rene O. Sanchez Mejia, B.A., Victor O. Ona and M. D. Mingwei Li, M.D., Robert M. Friedlander, "Minocycline reduces traumatic brain injurymediated caspase-1 activation, tissue damage, and neurological dysfunction," *Neurosurg. ,* vol. 48, no. 6, pp. 1393–1400, 2008.

[95]   L. Spurr, S. Nadkarni, M. Pederzoli-Ribeil, N. J. Goulding, M. Perretti, and Filvio D'Acquisto, "Comparitive analysis ofo Annexin A1-formyl peptide receptor 2/ALX expression in human leukocyte subsets," *Int. Immunopharmacol.*, vol. 11, no. 1, pp. 55–66, 2011.

[96]   F. N. E. Gavins, J. Dalli, R. J. Flower, D. N. Granger, and M. Perretti, "Activation of the annexin 1 counter-regulatory circuit affords protection in the mouse brain microcirculation," *FASEB J.*, vol. 21, no. 8, pp. 1751–1758, 2007.

[97]   F. N. E. Gavins and M. J. Hickey, "Annexin A1 and the regulation of innate and adaptive immunity," *Front. Immunol.*, vol. 3, pp. 1–11, 2012.

[98]   H. K. Smith, C. D. Gil, S. M. Oliani, and F. N. E. Gavins, "Targeting formyl peptide receptor 2 reduces leukocyte-endothelial interactions in a murine model of stroke," *FASEB J.*, vol. 29, no. 5, pp. 1–11, 2015.

[99]   B. E. Chatterjee, S. Yona, G. Rosignoli, R. E. Young, S. Nourshargh, R. J. Flower, and M. Perretti, "Annexin 1-deficient neutrophils exhibit enhanced transmigration in vivo and increased responsiveness in vitro.," *J. Leukoc. Biol.*, vol. 78, no. 3, pp. 639–646, 2005.

[100] M. La, M. D'Amico, S. Bandiera, C. Filippo, S. M. Oliani, F. N. E. Gavins, J. Flower, Roderick, and M. Perretti, "Annexin 1 peptides protect against experimental myocardial ischemia-reperfusion: analysis of their mechanism of action," *FASED*, vol. 15, pp. 2247–2256, 2001.

[101] S. McArthur, E. Cristante, M. Paterno, H. Christian, F. Roncaroli, G. E. Gillies, and E. Solito, "Annexin A1: A Central Player in the Anti-Inflammatory and Neuroprotective Role of Microglia," *J. Immunol.*, vol. 185, no. 10, pp. 6317–6328, 2010.

[102] Y. Zhang, A. Satterlee, and L. Huang, "In vivo gene delivery by nonviral vectors: Overcoming hurdles," *Mol. Ther.*, vol. 20, no. 7, pp. 1298–1304, 2012.

[103] S. J. Gwak, J. Nice, J. Zhang, B. Green, C. Macks, S. Bae, K. Webb, and J. S. Lee, "Cationic, amphiphilic copolymer micelles as nucleic acid carriers for enhanced transfection in rat spinal cord," *Acta Biomater.*, vol. 35, pp. 98–108, 2016.

[104] S. J. Gwak, C. Macks, D. U. Jeong, M. Kindy, M. Lynn, K. Webb, and J. S. Lee, "RhoA knockdown by cationic amphiphilic copolymer/siRhoA polyplexes enhances axonal regeneration in rat spinal cord injury model," *Biomaterials*, vol. 121, pp. 155–166, 2017.

[105] S. P. Didion, C. . Lynch, G. L. Baumbach, and F. M. Faraci, "Impaired endothelium-dependent responses and enhanced influence of Rho-kinase in cerebral arterioles in type II diabetes," *Stroke*, vol. 36, pp. 43–57, 2005.

[106] E. Brown, L. L. Munn, D. Fukumura, and R. K. Jain, "In vivo imaging of tumors.," *Cold Spring Harb Protoc*, 2010.

[107] Y. Adam and A. Mizrahi, "Long-term imaging reveals dynamic changes in the neuronal composition of the glomerular layer," *J Neurosci*, vol. 31, pp. 7967–7973, 2011.

[108] T. H. Chia and M. J. Levene, "Microprisms for in vivo multilayer cortical imaging," *J Neurophysiol*, pp. 1310–1314, 2009.

[109] C. Stetter, M. Hirschberg, B. Nieswandt, R. I. Ernestus, M. Heckmann, and A. L. Siren, "An experimental protocol for in vivo imaging of neuronal structural plasticity with 2-photon microscopy in mice.," *Exp Transl Stroke Med*, vol. 385, pp. 161–165, 2013.

[110] A. Nimmerjahn, F. Kirchhoff, and F. Helmchen, "Neuroscience: Resting microglial cells are highly dynamic surveillants of brain parenchyma in vivo," *Science (80-.).*, vol. 308, no. 5726, pp. 1314–1318, 2005.

[111] C. Ricard and F. C. Debarbieux, "Six-color intravital two-photon imaging of brain tumors and their dynamic microenvironment.," *Front Cell Neurosci*, vol. 8, p. 57, 2014.

[112] T. M. Hoogland, B. Kuhn, W. Gobel, W. HUang, J. Nakai, F. Helmchen, J. Flint, and S. S. Wang, "Radially expanding transglial calcium waves in the intact cerebellumo Title," *Proc. Natl. Acad. Sci.*, vol. 106, pp. 3496–3501, 2009.

[113] O. Barnstedt, P. Keating, Y. Weissenberger, A. J. King, and J. C. Dahmen, "Functional Microarchitecture of the Mouse Dorsal Inferior Colliculus Revealed through In Vivo Two-Photon Calcium Imaging," *J. Neurosci.*, vol. 35, pp. 10927–10939, 2015.

[114] D. A. Dombeck, A. N. Khabbaz, F. Collman, T. L. Adelman, and D. W. Tank, "Imaging large-scale neural activity with cellular resolution in awake, mobile mice.," *Neuron*, vol. 56, p. 43, 2007.

[115] E. Pinard, N. Engrand, and J. Seylaz, "Dynamic cerebral microcirculatory changes in transient forebrain ischemia in rats: involvement of type I nitric oxide synthase," *J. Cereb. Blood Flow Metab.*, vol. 20, pp. 1648–1658, 2000.

[116] S. Pai, K. J. Danne, J. Qin, L. L. Cavangh, A. Smith, M. J. Hickey, and W. Weninger, "Visualizing leukocyte trafficking in the living brain with 2-photon intravital microscopy.," *Front. Cell. Neurosci.*, vol. 6, p. 67, 2012.

[117] S. A. Lee, K. S. Holly, V. Voziyanov, S. L. Villalba, R. Tong, H. E. Grigsby, E. Glasscock, F. G. Szele, I. Vlachos, and T. A. Murray, "Gradient index microlens implanted in prefrontal cortex of mouse does not affect behavioral test performance over time," *PLoS One*, vol. 11, no. 1, pp. 1–19, 2016.

[118] R. W. Gilsdorf and J. C. Palais, "Single-mode fiber coupling efficiency with graded-index rod lenses," *Appl. Opt.*, vol. 33, pp. 3440–3445, 1994.

[119] A. Y. Shih, C. Mateo, P. J. Drew, P. S. Tsai, and D. Kleinfeld, "A polished and reinforced thinned-skull window for long-term imaging of the mouse brain.," *J. Vis. Exp.*, 2012.

[120] A. C. Caro, F. C. Hankenson, and J. O. Marx, "Comparison of thermoregulatory devices used during anesthesia of C57BL/6 mice and correlations between body temperature and physiologic parameters," *J Am Assoc Lab Anim Sci*, vol. 52, pp. 577–583, 2013.

[121] J. Lifshitz, B. J. Kelley, and J. T. Povlishock, "Perisomatic thalamic axotomy after diffuse traumatic brain injury is associated with atrophy rather than cell death," *J Neuropathol Exp Neurol*, vol. 66, no. 218–229, 2007.

[122] S. E. Crowe and G. C. Eliis-Davies, "Longitudinal in vivo two-photon fluorescence imaging.," *J Comp Neurol*, vol. 522, pp. 1708–1727, 2014.

[123] I. T. Filho, L. N. Torres, J. L. Sondeen, I. A. Polykratis, and M. A. Dubick, "In vivo evaluation of venular glycocalyx during hemorrhagic shock in rats using intravital microscopy.," *Microvasc Res*, vol. 85, pp. 128–133, 2013.

[124] F. W. Damen, A. R. Adelsperger, K. E. Wilson, and C. J. Goergen, "Comparison of Traditional and Integrated Digital Anesthetic Vaporizers.," *J Am Assoc Lab Anim Sci*, vol. 54, pp. 756–762, 2015.

[125] G. C. Brown and J. J. Neher, "Microglial phagocytosis of live neurons," *Nat. Publ. Gr.*, vol. 15, no. 4, pp. 209–216, 2014.

[126] X. Hu, P. Li, Y. Guo, H. Wang, R. K. Leak, S. Chen, Y. Gao, and J. Chen, "Microglia/macrophage polarization dynamics reveal novel mechanism of injury expansion after focal cerebral ischemia," *Stroke*, vol. 43, no. 11, pp. 3063–3070, 2012.

[127] N. D. Stankovic, Teodorczyk, R. Ploen, F. Zipp, and M. H. H. Schmidt, "Microglia-blood vessel interactions: a double-edged sword in brain pathologies," *Acta Neuropathol.*, vol. 131, pp. 347–363, 2016.

[128] M. A. Yenari, L. Xu, N. T. Xian, Y. Qiao, and R. G. Giffard, "Microglia potentiate damage to blood-brain barrier constituents: Improvement by minocycline in vivo and in vitro," *Stroke*, vol. 37, no. 4, pp. 1087–1093, 2006.

[129] G. J. Del Zoppo, R. Milner, T. Mabuchi, S. Hung, X. Wang, G. I. Berg, and J. A. Koziol, "Microglial activation and matrix protease generation during focal cerebral ischemia," *Stroke*, vol. 38, no. 2, pp. 646–651, 2007.

[130] C. M. Webster, M. Hokari, A. McManus, X. N. Tang, H. Ma, R. Kacimi, and M. A. Yenari, "Microglial P2Y12 Deficiency/Inhibition Protects against Brain Ischemia," *PLoS One*, vol. 8, no. 8, 2013.

[131] J. C. d'Avila, T. I. Lam, D. Bingham, J. Shi, S. Won, T. M. Kauppinen, S. Massa, J. Liu, and R. a Swanson, "Microglial activation induced by brain trauma is suppressed by post-injury treatment with a PARP inhibitor," *J. Neuroinflammation*, vol. 9, no. 1, pp. 31–41, 2012.

[132] W. S. Rasband, "ImageJ." U.S. National Institutes of Health, Bethesda, 1997.

[133] I. Hovens, C. Nyakas, and R. Schoemaker, "A novel method for evaluating microglial activation using ionized calcium-binding adaptor protein-1 staining: cell body to cell size ratio," *Neuroimmunol. Neuroinflammation*, vol. 1, no. 2, p. 82, 2014.

[134] T. A. Ferreira, A. Blackman, J. Oyrer, A. Jayabal, A. Chung, J. Sjostrom, and D. van Meyell, "Neuronal morphometry directly brom bitmap images," *Nat. Methods*, vol. 10, pp. 982–984, 2011.

[135] D. G. Siedler, M. I. Chuah, M. T. K. Kirkcaldie, J. C. Vickers, and A. E. King, "Diffuse axonal injury in brain trauma: insights from alterations in neurofilaments," *Front. Cell. Neurosci.*, vol. 8, pp. 1–10, 2014.

[136] A. H. S. Holbourn, "The Mechanics of Brain Injuries," *Lancet*, vol. 242, no. 6267, pp. 438–441, 1943.

[137] S. J. Strich, "Diffuse Degeneration of the Cerebral White Matter in Severe Dementia Following Head Injury," *J. Neurol. Neurosurg. Psychiatry*, vol. 19, no. 3, pp. 163–185, 1956.

[138] D. R. Oppenheimer, "Microscopic lesions," *J. Neurol. Neurosurg. Psychiatry*, vol. 31, pp. 299–306, 1968.

[139] A. I. R. Maas, N. Stocchetti, and R. Bullock, "Moderate and severe traumatic brain injury in adults.," *Lancet. Neurol.*, vol. 7, no. 8, pp. 728–41, 2008.

[140] J. Ahmad and P. Pienkowski, "Regional Differences in Microtubule and in the Axon," *J. Neurosci.*, vol. 73, no. 2, pp. 856–866, 1993.

[141] D. H. Smith, J. a Wolf, T. a Lusardi, V. M. Lee, and D. F. Meaney, "High tolerance and delayed elastic response of cultured axons to dynamic stretch injury.," *J. Neurosci.*, vol. 19, no. 11, pp. 4263–4269, 1999.

[142] M. D. Tang-Schomer, A. R. Patel, P. W. Baas, and D. H. Smith, "Mechanical breaking of microtubules in axons during dynamic stretch injury underlies delayed elasticity, microtubule disassembly, and axon degeneration," *FASEB J.*, vol. 24, no. 5, pp. 1401–1410, 2010.

[143] H. Bramlett, S. Kraydieh, E. Green, and D. Dietrich, "Temporal and Regional Patterns of Axonal Damage following Traumatic Brain injury: A Beta-amyloid precursor protein Immunocytochemical Study in Rats," *J. Neuropathol. Experimenental Neurol.*, vol. 56, pp. 1132–1141, 1997.

[144] J. E. Pierce, J. Q. Trojanowski, D. I. Graham, D. H. Smith, and T. K. McIntosh, "Immunohistochemical characterization of alterations in the distribution of amyloid precursor proteins and beta-amyloid peptide after experimental brain injury in the rat," *J.Neurosci.*, vol. 16, no. 3, pp. 1083–1090, 1996.

[145] D. H. Smith, K. Uryu, K. E. Saatman, J. Q. Trojanowski, and T. K. McIntosh, "Protein accumulation in traumatic brain injury.," *Neuromolecular Med*, vol. 4, no. 1–2, pp. 59–72, 2003.

[146] A. M. DiLeonardi, J. W. Huh, and R. Raghupathi, "Impaired Axonal Transport And Neurofilament Compaction Occur In Seperate Populations of Injured Axons following Diffuse Brain Injury in the Immature Rate," *Brain Res.*, vol. 1263, pp. 174–182, 2009.

[147] C. Marmarou and J. T. Povlishock, "Administration of the immunophilin ligand FK506 differentially attentuates neurofilament compaction and impaired axonal transport in injured axons following diffuse traumatic brain injury," *Exp. Neurol.*, vol. 197, pp. 353–362, 2006.

[148] M. D. Tang-Schomer, V. E. Johnson, P. W. Baas, W. Stewart, and D. H. Smith, "Partial interruption of axonal transport due to microtubule breakage accounts for the formation of periodic varicosities after traumatic axonal injury," *Exp. Neurol.*, vol. 233, no. 1, pp. 364–372, 2012.

[149] R. O. Sanchez Mejia, V. O. Ona, M. Li, and R. M. Friedlander, "Minocycline reduces traumatic brain injury-mediated caspase-1 activation, tissue damage, and neurological dysfunction," *Neurosurgery*, vol. 48, no. 6, pp. 1393–1401, 2001.

[150] J. Alder, W. Fujioka, J. Lifshitz, D. P. Crockett, and S. Thakker-Varia, "Lateral fluid percussion: model of traumatic brain injury in mice.," *J. Vis. Exp.*, no. 54, pp. 1–6, 2011.

[151] S. T. Fujimoto, L. Longhi, K. E. Saatman, and T. K. McIntosh, "Motor and cognitive function evaluation following experimental traumatic brain injury," *Neurosci. Biobehav. Rev.*, vol. 28, no. 4, pp. 365–378, 2004.

[152] M. Antunes and G. Biala, "The novel object recognition memory: Neurobiology, test procedure, and its modifications," *Cogn. Process.*, vol. 13, no. 2, pp. 93–110, 2012.

[153] P. Thevenaz, U. E. Ruttimann, and M. Unser, "A pyramid approach to subpixel regidtration based on intensity," *IEEE Trans. Image Process.*, vol. 7, no. 1, pp. 27–41, 1998.

[154] V. E. Johnson, J. E. Stewart, F. D. Begbie, J. Q. Trojanowski, D. H. Smith, and W. Stewart, "Inflammation and white matter degeneration persist for years after a single traumatic brain injury," *Brain*, vol. 136, no. 1, pp. 28–42, 2013.

[155] S. Casha, D. Zygun, M. D. McGowan, I. Bains, V. W. Yong, and R. John Hurlbert, "Results of a phase II placebo-controlled randomized trial of minocycline in acute spinal cord injury," *Brain*, vol. 135, no. 4, pp. 1224–1236, 2012.

[156] T. Tikka, B. L. Fiebich, G. Goldsteins, R. Keinanen, and J. Koistinaho, "Minocycline, a tetracycline derivative, is neuroprotective against excitotoxicity by inhibiting activation and proliferation of microglia.," *J. Neurosci.*, vol. 21, no. 8, pp. 2580–2588, 2001.

[157] E. Kovesdi, A. Kamnaksh, D. Wingo, F. Ahmed, N. E. Grunberg, J. B. Long, C. E. Kasper, and D. V. Agoston, "Acute minocycline treatment mitigates the symptoms of mild blast-induced traumatic brain injury," *Front. Neurol.*, vol. 3, pp. 1–18, 2012.

[158] A. F. Ramlackhansingh, D. J. Brooks, R. J. Greenwood, S. K. Bose, F. E. Turkheimer, K. M. Kinnunen, S. Gentleman, R. A. Heckemann, K. Gunanayagam, G. Gelosa, and D. J. Sharp, "Inflammation after trauma: Microglial activation and traumatic brain injury," *Ann. Neurol.*, vol. 70, no. 3, pp. 374–383, 2011.

[159] K. Kobayashi, S. Imagama, T. Ohgomori, K. Hirano, K. Uchimura, K. Sakamoto, A. Hirakawa, H. Takeuchi, A. Suzumura, N. Ishiguro, and K. Kadomatsu, "Minocycline selectively inhibits M1 polarization of microglia.," *Cell Death Dis.*, vol. 4, no. 3, pp. 1–9, 2013.

[160] J. E. Greer, M. J. McGinn, and J. T. Povlishock, "Diffuse traumatic axonal injury in the mouse induces atrophy, c- Jun activation and axonal outgrowth in the axotomized neuronal population," *J Neurosci*, vol. 31, no. 13, pp. 5089–5105, 2011.

[161] S. G. Abdel Baki, B. Schwab, M. Haber, A. A. Fenton, and P. J. Bergold, "Minocycline synergizes with N-acetylcysteine and improves cognition and memory following traumatic brain injury in rats," *PLoS One*, vol. 5, no. 8, pp. 1–8, 2010.